JRC Scientific and Technical Reports

Non-linear Shear Model for R/C Piers

J. Guedes, A.V. Pinto, P. Pegon

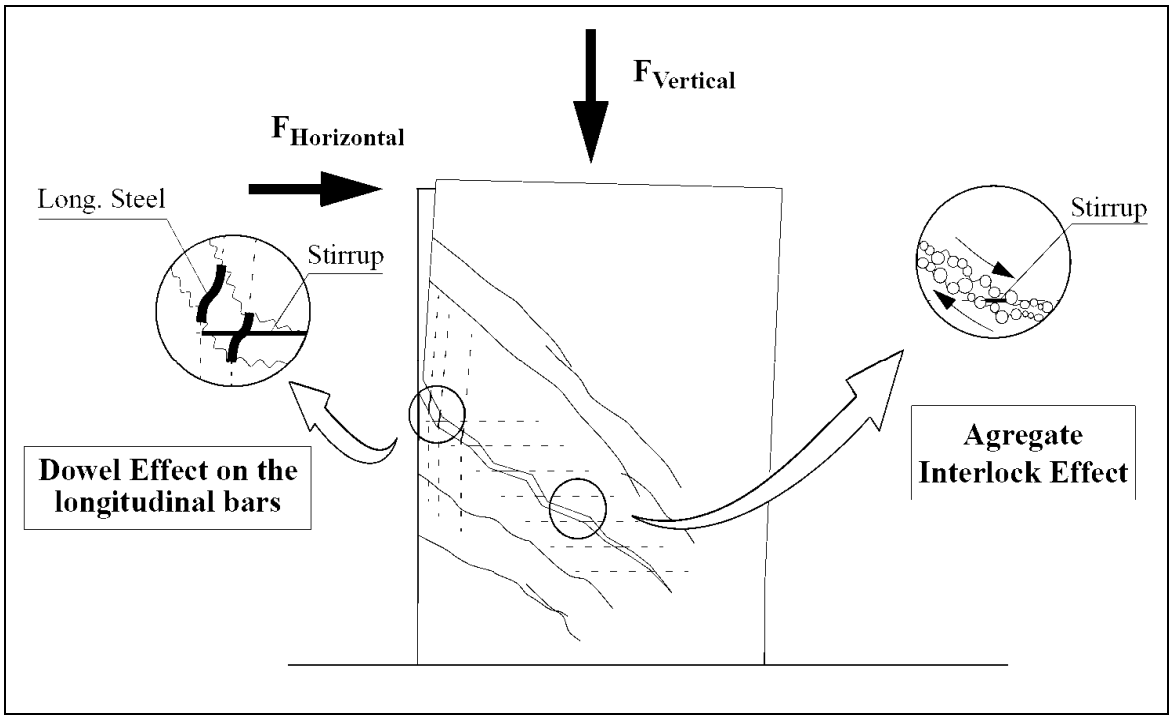

EUR 24153 EN - 2010

JRC EUROPEAN COMMISSION

ipsc Institute for the Protection and Security of the Citizen

The mission of the JRC-IPSC is to provide research results and to support EU policy-makers in their effort towards global security and towards protection of European citizens from accidents, deliberate attacks, fraud and illegal actions against EU policies.

European Commission
Joint Research Centre
Institute for the Protection and Security of the Citizen

Contact information
Address: Joint Research Centre, ELSA Unit, TP 480, 21027 Ispra (Va), Italy
E-mail: artur.pinto@jrc.ec.europa.eu
Tel.: +39 (0332) 789294
Fax: +39 (0332) 78 9049

http://ipsc.jrc.ec.europa.eu/
http://www.jrc.ec.europa.eu/

Legal Notice
Neither the European Commission nor any person acting on behalf of the Commission is responsible for the use which might be made of this publication.

Europe Direct is a service to help you find answers to your questions about the European Union

Freephone number (*):

00 800 6 7 8 9 10 11

(*) Certain mobile telephone operators do not allow access to 00 800 numbers or these calls may be billed.

A great deal of additional information on the European Union is available on the Internet.
It can be accessed through the Europa server http://europa.eu/

JRC 56446

EUR 24153 EN
ISBN 978-92-79-14874-3
ISSN 1018-5593
DOI 10.2788/56304

Luxembourg: Office for Official Publications of the European Communities

© European Union, 2010

Reproduction is authorised provided the source is acknowledged

Printed in Italy

TABLE OF CONTENTS

1 INTRODUCTION 13

2 NON-LINEAR SHEAR MODELS 17

2.1 Shear mechanisms in R/C structural elements 17
2.2 Numerical modelling 20
2.2.1 Chang model 20
2.2.2 Priestley model 22
2.2.3 A Strut-and-Tie model for 2D elements 23
2.2.4 Fibre based models 25

3 STRUT-AND-TIE MODEL IN FIBRE MODELLING 27

3.1 Fibre model 27
3.2 Non-linear shear modelling 29
3.2.1 Compatibility equations 31
3.2.2 Equilibrium equations 34
3.2.3 Damage of the struts 35
3.2.4 Constitutive laws. Tensile strut 36
Concrete constitutive model 37
Steel constitutive model 41
3.2.5 Shear ‘cracking’ angle 42
Cracking limit analysis 43
Cracking equilibrium model 45
3.2.6 Strut cross-section area 47
3.3 Summary 49

4 NUMERICAL IMPLEMENTATION 51

4.1 Parameters of the model in CASTEM 2000 51
4.2 Strain in the transverse steel 52
4.2.1 Equations of compatibility for incremental displacements 53
4.2.2 Equilibrium of internal forces - Iterative algorithm 53
4.3 Shear tangent stiffness 55
4.4 Modelling and implementation remarks 57
4.4.1 Yielding of transverse steel 57
4.4.2 Torsional moments 58
4.4.3 The snap-back phenomenon 60

5 MODEL VALIDATION 65

5.1 Experimental reference results 66
5.2 Numerical applications 68
5.2.1 Model parameters 69
5.2.2 Fibre discretization 71
5.2.3 Struts inclination angle 72

6 RESULTS 75
6.1 General results 75
6.1.1 Low strength pier - P1 76
6.1.2 Medium strength pier - P3 78
6.1.3 High strength pier - P5 78

7 CONCLUSIONS 81

8 REFERENCES 83

9 FIGURES 85

LIST OF FIGURES

2 NON-LINEAR SHEAR MODELS 17
Figure 2.1 -Diagonal cracking: dowel and interlock effect 18
Figure 2.2 -Chang model 22
Figure 2.3 -Contribution of axial load to shear strength (Priestly model [12]) 24
Figure 2.4 -Average stress-strain response of concrete. Modified model due to Vecchio and Collins . . 25

3 STRUT-AND-TIE MODEL IN FIBRE MODELLING 27
Figure 3.1 -Fibre model - deformation of the transverse section. 28
Figure 3.2 -Fibre model - deformation of the transverse section. 30
Figure 3.3 -Cracking pattern - internal acting forces 31
Figure 3.4 -Truss analogy 32
Figure 3.5 -Compatibility of displacements 33
Figure 3.6 -Internal forces in the section 35
Figure 3.7 -Axial stress-strain constitutive law for concrete 38
Figure 3.8 -Influence of the tensile behaviour law in the shear stress versus strain response curve. . . . 40
Figure 3.9 -Axial stress-strain constitutive law for steel 43
Figure 3.10 -Analogy with a membrane 45
Figure 3.11 -Cracking equilibrium model 46
Figure 3.12 -Cross-sectional area of the struts 48

4 NUMERICAL IMPLEMENTATION 51
Figure 4.1 -Shear fibre model 52
Figure 4.2 -Influence of yielding of the stirrups in the shear stress versus strain response curve 59
Figure 4.3 -Torsional moments 60
Figure 4.4 -Numerical simulation of torsional moments resisting mechanism 61
Figure 4.5 -The ‘snap-back’ phenomenon 62

5 MODEL VALIDATION 65
Figure 5.1 -Geometrical characteristics of bridges tested at the ELSA laboratory (scale 1:1). 65
Figure 5.2 -Reinforcement layout (all the measurements and diameters are in [mm]) 68
Figure 5.3 -Splitting of shear and bending displacements 69
Figure 5.4 -Confined and unconfined concrete characteristics. 70
Figure 5.5 -Longitudinal and transverse steel characteristics 70

Figure 5.6 -Distribution of the fibres in the cross-section (bending + shear) 72
Figure 5.7 -Cracking angle using the ‘cracking equilibrium model’. 73

9 FIGURES 85

Figure 9.1 -History of displacements imposed at the top of the piers 85
Figure 9.2 -Numerical versus experimental force-total displacement response curves for pier P1D at two different height levels and using the non-linear shear model with θ=68o 86
Figure 9.3 -Numerical versus experimental force-flexural and shear displacement response curves at 1.7m from the bottom, for pier P1D, using the non-linear shear model with θ=68o 87
Figure 9.4 -Numerical versus experimental force-total displacement response curves for pier P1D at two different height levels and using the linear elastic shear model 88
Figure 9.5 -Numerical versus experimental force-flexural and shear displacement response curves at 1.7m from the bottom, for pier P1D, using the linear shear model 89
Figure 9.6 -Numerical versus experimental force-total displacement response curves for pier P3D at two different height levels and using the non-linear elastic shear model with θ=56o. 90
Figure 9.7 -Numerical versus experimental force-flexural and shear displacement response curves at 1.7m from the bottom, for pier P3D, using the non-linear shear model with θ=56o 91
Figure 9.8 -Numerical versus experimental force-total displacement response curves for pier P3D at two different height levels and using the linear elastic shear model 92
Figure 9.9 -Numerical versus experimental force-flexural and shear displacement response curves at 1.7m from the bottom, for pier P3D, using the linear elastic shear model 93
Figure 9.10 -Numerical versus experimental force-total displacement response curves for pier P3S at two different height levels and using the non-linear shear model with θ=56o 94
Figure 9.11 -Numerical versus experimental force-flexural and shear displacement response curves at 1.7m from the bottom, for pier P3S, using the non-linear shear model with θ=56o 95
Figure 9.12 -Numerical versus experimental force-total displacement response curves for pier P3S at two different height levels and using the linear elastic shear model 96
Figure 9.13 -Numerical versus experimental force-flexural and shear displacement response curves at 1.7m from the bottom, for pier P3S, using the linear elastic shear model 97
Figure 9.14 -Numerical versus experimental force-total displacement response curves for pier P5D at two different height levels and using the non-linear shear model with θ=54o 98
Figure 9.15 -Numerical versus experimental force-flexural and shear displacement response curves at 1.7m from the bottom, for pier P5D, using the non-linear shear model with θ=54o 99
Figure 9.16 -Numerical versus experimental force-total displacement response curves for pier P5D at two different height levels and using the linear elastic shear model 100
Figure 9.17 -Numerical versus experimental force-flexural and shear displacement response curves at 1.7m from the bottom, for pier P5D, using the linear elastic shear model 101
Figure 9.18 -Numerical versus experimental peak displacement profiles for the four piers and the non-linear shear model. 102
Figure 9.19 -Numerical versus experimental force-total, flexural and shear displacement response curves for pier P5D with different transverse critical cracking angles 103
Figure 9.20 -Numerical versus experimental force-total, flexural and shear displacement response curves for pier P5D for different transverse steel ratios 104
Figure 9.21 -Numerical force versus total, flexural and shear displacement response curves for pier P5D for different mesh discretization 105

Figure 9.22 -Numerical versus experimental force-total displacement response curves for pier P1D at two different height levels and using the non-linear shear model with θ=45o 106

Figure 9.23 -Numerical versus experimental force-flexural and shear displacement response curves at 1.7m from the bottom, for pier P1D, using the non-linear shear model with θ=45o 107

Figure 9.24 -Numerical versus experimental force-total displacement response curves for pier P3D at two different height levels and using the non-linear elastic shear model with θ=45o. 108

Figure 9.25 -Numerical versus experimental force-flexural and shear displacement response curves at 1.7m from the bottom, for pier P1D, using the non-linear shear model with θ=45o 109

Figure 9.26 -Numerical versus experimental force-total displacement response curves for pier P3S at two different height levels and using the non-linear shear model with θ=45o 110

Figure 9.27 -Numerical versus experimental force-flexural and shear displacement response curves at 1.7m from the bottom, for pier P3S, using the non-linear shear model with θ=45o 111

Figure 9.28 -Numerical versus experimental force-total displacement response curves for pier P5D at two different height levels and using the non-linear shear model with θ=45o 112

Figure 9.29 -Numerical versus experimental force-flexural and shear displacement response curves at 1.7m from the bottom, for pier P5D, using the non-linear shear model with θ=45o 113

Figure 9.30 -Numerical versus experimental peak displacement profiles for the four piers and the non-linear shear model. 114

LIST OF TABLES

5 MODEL VALIDATION 65
Table 5.1: Steel mechanical properties (average values) 67
Table 5.2: Concrete cubic compressive strength (average values) 67
Table 5.3: Longitudinal and transverse reinforcement in the piers cross-section 67
Table 5.4: Transverse steel ratio 71
Table 5.5: Critical cracking angle θ 72
Table 5.6: Cracking angle 73

ABSTRACT

The work presented has been developed within the Prenormative Research in support of EuroCode 8 (PREC8) programme of the European Commission. The EuroCode 8 (EC8) are the provisional European standards for the design of civil engineering structures in seismic prone areas. This programme included experimental test on a series of bridge structures that have been tested under Pseudo-Dynamic conditions.

Experimental tests were carried out to study the behaviour of bridge piers under cyclic loading. The results from these tests underlined the need to improve an existing fiber-model to represent the non-linear behaviour of structures where the influence of the shear forces is not negligible. Thus, a strut-and-tie formulation coupled with the classic fibre model for flexural forces was developed. This formulation is based on the analogy of a R/C structure damaged with diagonal cracking with a truss made of concrete diagonals and steel ties.

The model is applied to a set of bridge piers tested at the ELSA laboratory and the results are compared with the experimental response.

1 INTRODUCTION

Earthquakes damage civil engineering structures every year and bridges are no exception. Historically, bridges have proven to be vulnerable to earthquakes, sustaining damage to substructures and foundations and in some cases being totally destroyed as superstructures collapse from their supporting elements [1]. In particular, shear failure due to inadequate detailing and/or poor confinement of concrete core was observed in several bridge piers emphasizing the importance of shear strength in the design phase.

As a matter of fact, these seismic events represent an important '*in situ*' source of information that should not be neglected and, furthermore, should be always present in the improvement of design codes and guidelines. In fact, significant advances in seismic design and strengthening of bridges have occurred after large earthquakes. The 1971 San Fernando earthquake caused substantial damage and exposed a number of deficiencies in the bridge design specifications of that time. During the Loma Prieta earthquake of October 1989, the dramatic collapse of the Cypress Street Viaduct in Okland and the damage of many elevated freeway bridge structures in the San Francisco bay area highlighted weaknesses in bent joints, lack of ductility in beams and columns and poor resistance to longitudinal and transversal loads. Inspections (observed damage) after the earthquake revealed shear cracking and spalling of concrete especially in outrigger knee joints on bends of several reinforced concrete (R/C) viaducts [2].

More recent events like the Northridge earthquake of January 1994 and the Kobe earthquake of January 1995, stressed once again those deficiencies. In particular, shear failure

was observed on several bridge piers again, emphasizing the importance of design and detailing of transverse steel to provide proper shear strength/capacity. Changes in the design code and guidelines were and are still undertaken to compensate for these shortcomings.

It should be pointed out that, although a general design code exists for civil engineering structures, bridges structures exhibit some characteristics that make them quite different from ordinary buildings, demanding special guidelines. Firstly, the mass of the bridge deck is an order of magnitude larger than the mass of a typical floor system. Secondly, bridge structural systems are not as redundant as typical building structures. This means that, although in a beam sides-way mechanism the plastic hinges would normally be located at the extremities of the beams, in bridge structures it is neither feasible nor desirable to locate them in the superstructure. Instead, it is preferable to place them in the columns, which end up being the primary sources of energy dissipation.

The aim of design is, therefore, to provide sufficient deformation capacity and shear strength to ensure that under seismic loads the columns present a ductile behaviour and that no shear failure occurs. It is now generally accepted that the ductile behaviour of a reinforced concrete column can be reached by supplying sufficient transverse reinforcement in the plastic hinge regions to provide adequate shear strength and, at the same time, to properly confine the concrete core in the section and prevent premature buckling of the longitudinal reinforcement.

The behaviour of bridge structures subject to important transverse type loading is now more than ever a matter of great experimental and numerical research interest. The aim of this report is to describe the non-linear shear model developed at the European Laboratory of Structural Assessment (ELSA) at Ispra, Italy, for piers with low shear span ratio.

After a general and brief description of non-linear shear models, the developed model, a strut-and-tie type formulation coupled with the fibre model already implemented in CASTEM 2000 [3], is presented. The details of the constitutive relations for both concrete and steel materials are described and several applications are carried out in order to

assess the performance of the tools developed; the numerical response of bridge piers is compared with experimental results, in particular with those from the experimental campaign performed at the ELSA laboratory [4]: four R/C structures with two different profiles representing a regular and an irregular bridge under horizontal transverse cyclic loading. The main conclusions are drawn in the last section.

2 NON-LINEAR SHEAR MODELS

Experimental tests on low shear span ratio R/C columns under important shear forces, especially when combined with high axial forces, have shown quite a different behaviour compared to columns under predominant flexural moments. A brittle behaviour with opening of inclined cracks and sudden crushing of diagonal concrete, caused by the combination of high axial and shear stresses, is often observed in laboratory tests. Seismic events like the Northridge and the Kobe earthquakes, confirmed these results and underlined the need to consider the influence of shear forces on the resistance and ductility capacity of reinforced concrete structures. This is particularly relevant in structures with different members set together where, due to their higher initial stiffness, short columns take most of the horizontal loading.

To develop a model capable of representing the response of such elements subjected to important transverse forces, it is essential to have a good understanding of the physical phenomena involved. Hence, before entering into the modelling aspects, the shear mechanism and damage process of R/C squat piers is reviewed.

2.1 Shear mechanisms in R/C structural elements

Experimental tests on reinforced concrete columns (e.g. Li [5]) show that, before cracking, the shear force is mainly carried by the concrete. The formation of cracks reduces the concrete active area, decreasing the shear resisting capacity of the concrete. However, diagonal cracking activates, through shear deformation, the aggregate interlock action along the cracks and the dowel force from longitudinal bars, giving a supplementary shear resistance to the cracked structure. The effectiveness of these two effects depends on the capacity of transverse steel to maintain both sides of the crack in contact. This capacity is directly related to the transverse steel ratio and to the spacing of the stirrups along the R/C element.

Thus, although before cracking the amount of transverse reinforcement has little effect on shear carrying capacity, after cracking, and especially in the post-yielding phase, it increases the shear strength of the column and improves its performance. Therefore, the role of transverse reinforcement in a column is to resist shear, to provide concrete core

confinement, increasing the concrete compression strength, and to prevent premature buckling of longitudinal bars. Experimental tests carried out in the ELSA laboratory showed that to prevent buckling it is important not only to provide the proper amount and spacing of transverse steel but also to adequately embrace the longitudinal bars; after the crushing of the concrete cover, some longitudinal bars not embraced by the stirrups buckled laterally, presenting an effective length two or three times the spacing of the transverse steel.

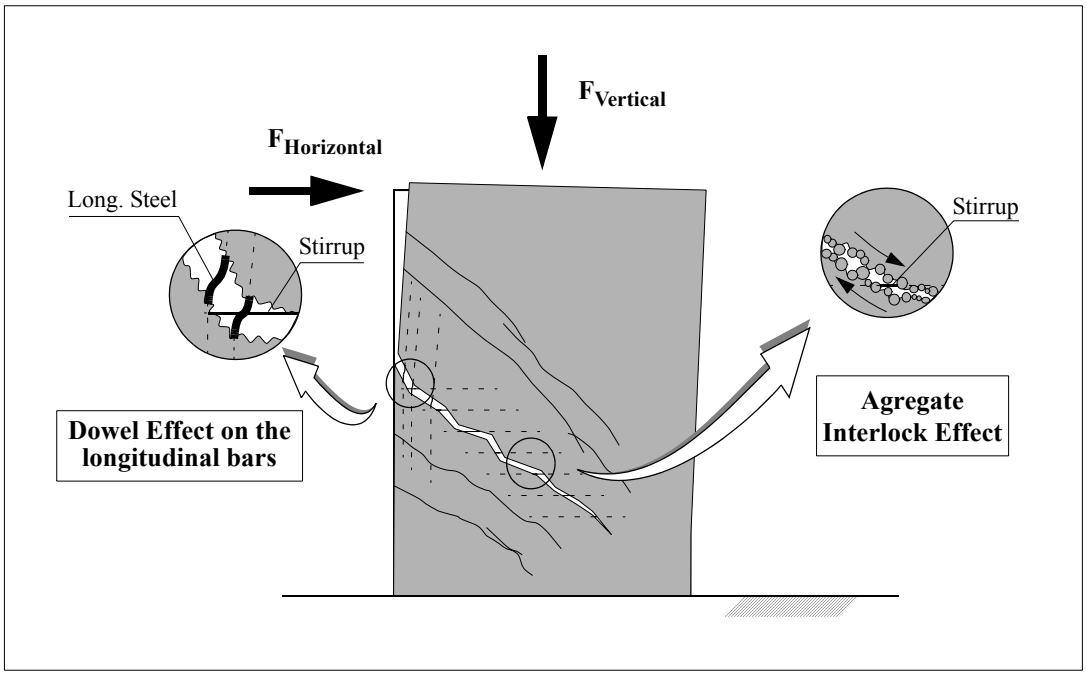

Figure 2.1 - Diagonal cracking: dowel and interlock effect

When the two surfaces of a crack of moderate width slide one against the other, a number of coarse aggregate particles projecting across the crack will enable shear forces to be transmitted [6]. As the shear load increases, the interface forces produce local crushing with a sliding of the crack surfaces and an important decrease in the shear stiffness. Upon unloading, the surfaces of the crack remain in contact until an opposite shear force pushes the surfaces in the other direction. Then, the two surfaces slide with little resistance until the aggregate particles come into contact again [7].

The longitudinal reinforcement also has an active role in the shear resisting mechanism. Firstly, it participates in the truss mechanism activated by diagonal cracking coupled with the transverse reinforcement and the diagonal concrete. Secondly, it contributes to

shear strength through its dowel force capacity. The dowel effect depends on many variables, namely: crack width, concrete cover, bar diameter, stress level in the bar, confinement around the bar and bar spacing. A detailed description of the involved phenomena can be found in [6] and [8].

Furthermore, axial load also has an important effect on shear strength capacity. While axial tensile forces favour the opening and delay the closure of diagonal cracks and, therefore, increase shear strength degradation, axial compression forces, up to a certain level, delay crack opening and increase the shear strength of the columns. Moreover, test results indicate that a more severe degradation of shear strength is observed in the case of varying axial load with cyclic bending.

The experimental results obtained by Li [5] confirm the interaction between shear strength and displacement ductility capacity; under cyclic loading the shear carried by the concrete decreases with increasing flexural displacement ductility. The reduction of shear strength is caused by the degradation of the concrete shear resisting mechanism during reversed cyclic loading. '*Concrete shear mechanism*' is the term commonly used to cover typical phenomena such as the aggregate interlock effect, the dowel action of flexural reinforcement and the shear transfer by the concrete through the truss mechanism [6].

Concerning shear failure, although it can be expressed in different ways, in general it is associated to crushing or splitting of the diagonal compressed concrete. It corresponds to the development of an unstable truss mechanism with cracks propagating through the compression zone. However, if transverse steel bars yield, they impose an unrestricted widening of diagonal cracks that cause the aggregate interlock action to become ineffective. In this case, the dowel effect and the truss mechanism having been pushed to their limits, failure occurs with little further deformation [6]. As for the inclination of the critical cracks to the column axis, the observation shows that the angle can be smaller than 45 degrees and, in general, the inclination becomes steeper as cracks propagate further into the compressed concrete zone. The experimental campaign carried out at the ELSA laboratory on squat bridge piers subjected to cyclic static loading confirms these results [4].

Although experimental results on R/C structures give a better understanding of the mechanisms involved, there is still much to investigate. The numerical simulation of the physical phenomena described is not an easy task and it is a present-day research topic. The next paragraphs give an overview of different numerical models dealing with the problem of the non-linear behaviour in shear.

2.2 Numerical modelling

Some authors suggest very simple models to represent the response of reinforced concrete structures under important transverse forces. The behaviour is simulated through global shear force-displacement curves representing each of the phenomena involved, namely: the aggregate interlock and the dowel effect, as described by Fardis [9] and Jimenez [10]. In general, these curves are based on experimental formulas.

Other authors propose the superimposition of different models for flexural and shear behaviour and it is common to find empirical laws for both or at least one of these two models, in particular to predict shear strength. Chang [11] presents a model of this kind.

2.2.1 Chang model

Two formulations are used to compute the response of the piers due to bending and shear behaviour. At each loading step, the equilibrium of axial forces and flexural moments is imposed in the column independently of the applied shear force. Then, according to the damage the column presents, different zones with different elastic equivalent shear stiffness are considered in the column, namely (see Figure 2.2): not cracked, cracked, inside the hinge or the plastic hinge region or outside. For a cantilever beam of length L, the elastic shear stiffness is given by:

- prior to cracking,

$$K_{ve} = \frac{G \cdot A_q}{f} \qquad 2.1$$

in which A_q is the area contributing to shear stiffness and f is a form section factor. The shear modulus is ($G = 0.4 \cdot E_c$) and it arises from the assumption of a Poisson ratio for concrete ($\nu = 0.25$);

- after cracking,

$$K_{\nu} = \frac{b_w \cdot d \cdot \cot\theta}{\frac{1}{E_s \cdot \rho_{\nu}} + \frac{1}{E_c \cdot (\sin\theta)^4}} \qquad 2.2$$

where θ is the inclination angle of the cracks with respect to the longitudinal axis, ($\rho_{\nu} = A_{\nu}/(s \cdot b_w)$) is the volumetric ratio of shear reinforcement, A_{ν} is the total area of stirrups, b_w and d are the width and the length of the concrete cross-section, s is the stirrups spacing and E_s and E_c are the steel and the concrete Young modulus, respectively.

These two expressions are applied to regions where no yielding of the longitudinal bars occurred. The shear displacement is computed through

$$\int_L (V/K)dx \qquad 2.3$$

where V is the transverse force, K represents the shear stiffness and L the total length of the column along the longitudinal $\overline{ox}$ axis of the structure. Taking as an example the column in Figure 2.2 and using equation (2.3), the total elastic shear displacement at the top is given by

$$\Delta_{se} = V \cdot L \cdot \left[\frac{1}{K_{\nu e}} \cdot \frac{M_{cr}}{M_{max}} + \frac{1}{K_{\nu h}} \cdot \frac{L_h}{L} + \frac{1}{K_{\nu c}} \cdot \left(1 - \frac{M_{cr}}{M_{max}} - \frac{L_h}{L}\right)\right] \qquad 2.4$$

where $K_{\nu h}$ is the shear stiffness within the hinge zone with length L_h and $K_{\nu c}$ is the shear stiffness outside the hinge zone. Both values are calculated through equation (2.2) but for different stirrups spacing values, inside or outside the hinge zone. M_{cr} and M_{max} are respectively the cracking and the maximum flexural moments in the structure. Thus, the flexural response determines the shear flexibility but without any feedback, i.e, the shear behaviour does not interfere in the flexural response of the structure.

When yielding of steel bars occurs, the behaviour is no longer elastic and an iterative process, using a strut-and-tie type model, is used to calculate the inelastic shear deformation. This method is based on a truss analogy where shear forces are resisted by a mech-

anism made of concrete struts and tensile ties that carry compression and tensile forces respectively. From the compatibility of displacements and the equilibrium of forces in the truss, a plastic shear deformation γ is computed. The total displacement due to shear is then given by

$$\Delta_{st} = \Delta_{se} + \gamma \cdot L_{pc} \qquad 2.5$$

being L_{pc} the yielded zone length.

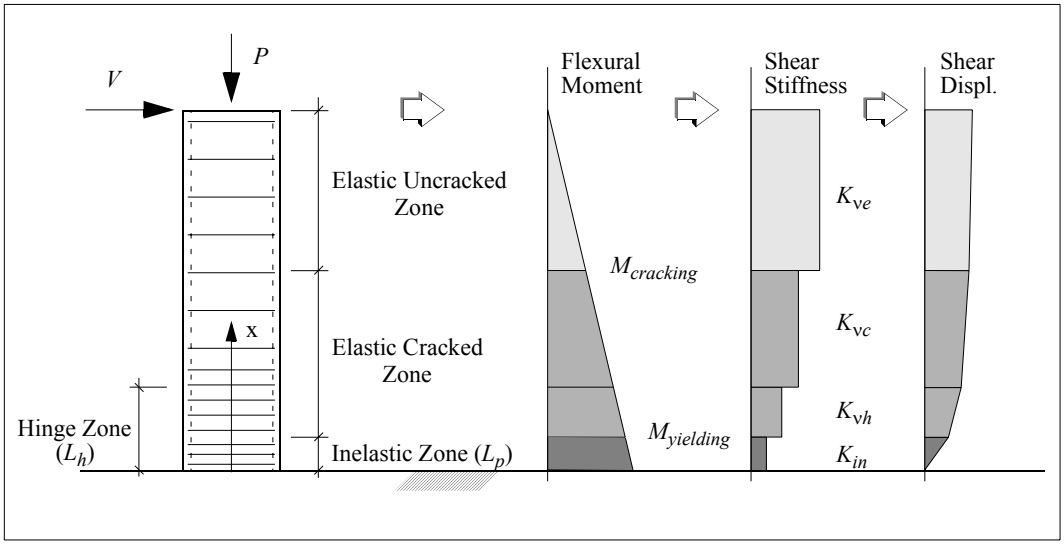

Figure 2.2 - Chang model

2.2.2 Priestley model

Some authors consider other semi-empirical models, most of them based in truss analogies. In general, they are used to calculate shear strength and not to establish hysteretic shear force-displacement response curves; given a structure with a pre-defined reinforced concrete cross section, these models predict a resisting mechanism and compute the contribution of the concrete and steel to the shear strength within that mechanism. Priestly [12], for instance, defines shear strength through the superimposition of three independent components which account for the contribution of the concrete, V_c, of the transverse steel via a truss mechanism, V_s, and of the axial load through an arch action, V_p,

$$V = V_c + V_s + V_p \qquad 2.6$$

There are several expressions available in the literature and in the design codes [13] to account for the contribution of the concrete and of the transverse steel to shear strength. However, in the case of the concrete, most of these expressions can be grouped in the general equation

$$V_c = K \cdot \sqrt{f'_c} \cdot b_w \cdot d \qquad 2.7$$

where d is the effective depth of the section, f'_c is the compression strength of the concrete and the parameter K includes the contribution of other factors to the concrete shear strength. Many codes consider the effect of the axial force through K, for instance.

For the contribution of transverse steel V_s, the equilibrium within the truss mechanism for a cracking angle θ gives

$$V_s = A_{sw} \cdot f_{sw} \cdot \frac{d}{s} \cdot \cot\theta \qquad 2.8$$

A_{sw} being the cross-sectional area of the stirrups, f_{sw} the stirrups yielding stress and s the stirrups spacing.

Priestly considers for the compression diagonals of the truss an inclination angle of ($\theta = 30^o$) to the column axis and calculates the contribution of the axial load V_p to shear strength through the horizontal component of a compression diagonal strut developing from the top of the column to the bottom, as illustrated in Figure 2.3. However, to capture the mechanics of the involved phenomena, more accurate models have to be used.

2.2.3 A Strut-and-Tie model for 2D elements

A strut-and-tie type model is often adopted for membrane elements. It assumes that the direction of principal stresses coincide with the direction of principal strains, which, in turn, are computed through the equations of compatibility of deformations in the membrane. The equilibrium equations are established making use of the uniaxial constitutive laws of the materials applied to each principal direction.

Two different modelling assumptions can be adopted: a rotating or a fixed crack angle

formulation. In the first case, the cracking angle follows the direction of the principal compression stresses in the concrete which, on the other hand, depend on the relative amount and distribution of steel in the plane of the membrane. On the contrary, in a fixed angle formulation the direction of the first crack defines the cracking angle for the rest of the loading history. In this case, the compatibility of displacements and the equilibrium of forces introduce an additional variable in the model: a shear strain together with a shear stress-strain law.

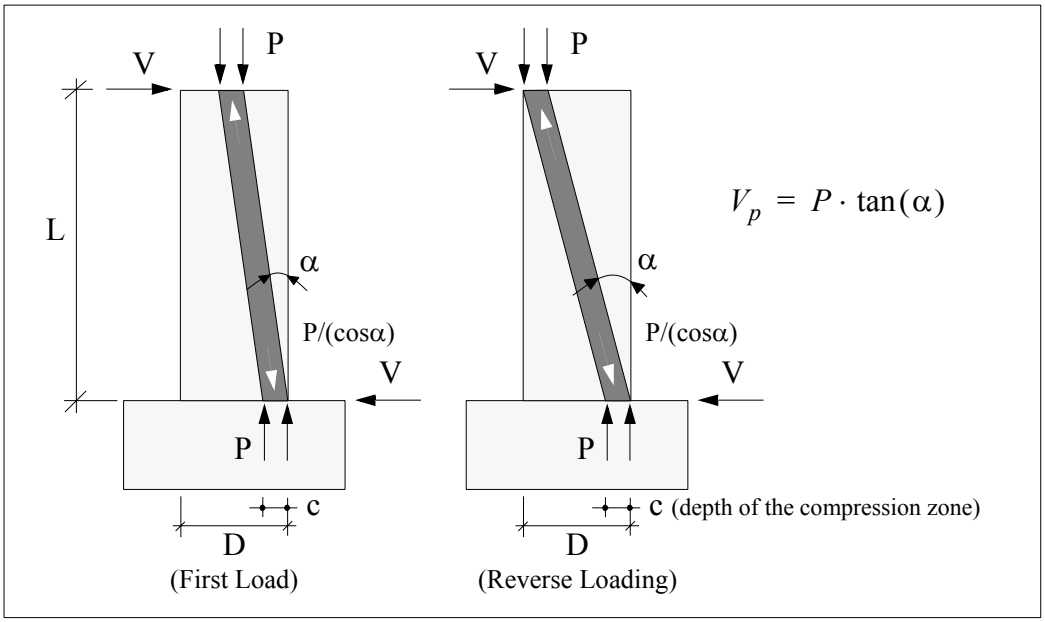

Figure 2.3 - Contribution of axial load to shear strength (Priestly model [12])

However, since the uniaxial stress-stain laws assume the material is homogeneous and damage is uniform, to represent appropriately the global behaviour of the concrete struts these laws should integrate the state of the concrete in a wide zone of the structure. In the Compression Field Theory (CFT), Vecchio and Collins proposes the first modified stress versus strain curve for the concrete in compression [14]. This uniaxial law tries to represent the average stress versus strain constitutive laws in the element.

The characteristics of the curve, strength and stiffness, depend on the principal tensile strain ε_1 (see Figure 2.4). The constitutive equations are expressed by

$$\sigma_c = \sigma'_c \cdot (0.8 - 0.34(\varepsilon_1 / \varepsilon'_c))^{-1} \cdot \left[2\left(\frac{\varepsilon_2}{\varepsilon'_c}\right) - \left(\frac{\varepsilon_2}{\varepsilon'_c}\right)^2 \right] \qquad 2.9$$

for compression forces and by

$$\sigma_c = \begin{cases} \dfrac{\sigma_{cr}}{1+\sqrt{200\varepsilon_1}} \wedge (\varepsilon_1 \geq \varepsilon_{cr}) \\ E_c \cdot \varepsilon_1 \wedge (\varepsilon_1 < \varepsilon_{cr}) \end{cases} \qquad 2.10$$

for tensile forces.

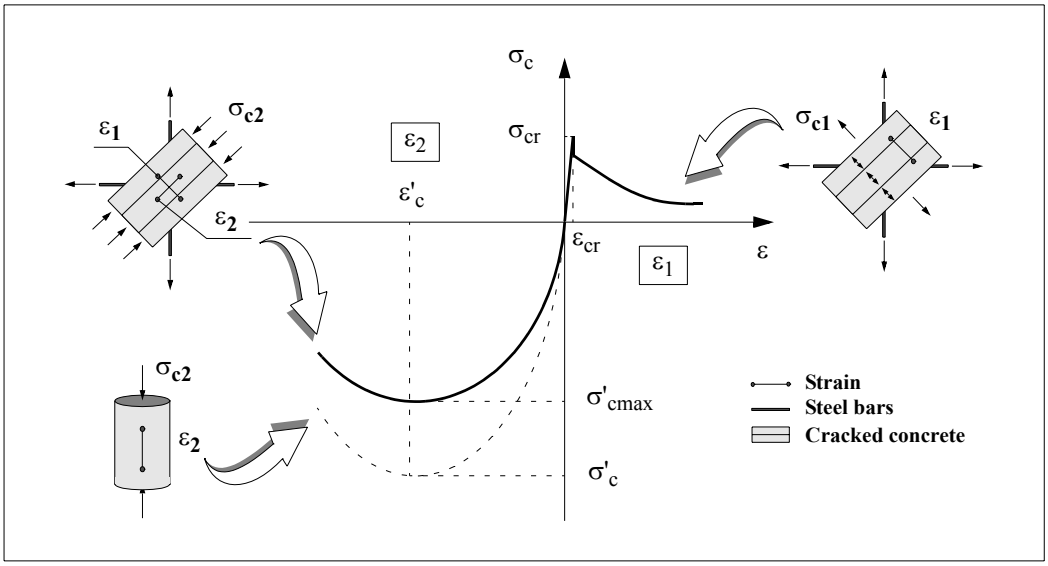

Figure 2.4 - Average stress-strain response of concrete. Modified model due to Vecchio and Collins

Since strut-and-tie type models make use of uniaxial stress-stain laws to represent the behaviour of concrete struts, the adoption of modified constitutive laws, taking into account the global state of the concrete, represented a considerable improvement to these models. Before that, the uniaxial compression strength of standard concrete cylinders was used, giving an overestimation of shear and torsional strength.

2.2.4 Fibre based models

The use of modified behaviour curves to represent the heterogeneous state of a material through a single homogenized law, is now common practice in several models. Garstka [15] superimposes a strut-and-tie model based on the CFT for shear deformations with a classic fibre model for flexural deformations. The model defines a truss made of concrete struts which follow a uniaxial stress-strain law modified to take into account the cracks in the perpendicular direction.

For structures with an one-dimensional (1D) geometry (e.g. beam, columns), Petrangeli and Pinto [16] propose the use of a fibre type model with three-dimensional (3D) constitutive laws for the concrete fibres to introduce diagonal cracking in the structure. In the algorithm, and apart from the global equilibrium of forces, the model establishes, at the level of each fibre, a supplementary internal equilibrium in the transverse direction which allows the computation of the transverse strain; an iterative process taking into account the amount of transverse steel in the cross-section has to be used for this purpose. The internal equilibrium having been established, the two or three-dimensional state of the concrete is defined.

The main difficulty in such a model is to find a three-dimensional model for the concrete which covers the entire range of possible cyclic loads. Furthermore, the computation phase can be far more time consuming and the number of variables defining the internal state of the cross-section can be much greater than in a standard model.

The model developed in ELSA for beam/column reinforced concrete elements under important shear loading is based on the procedure presented by Garstka: it superimposes the classic fibre model, which gives very good results for bending, with a strut-and-tie model to simulate cyclic shear behaviour.

3 STRUT-AND-TIE MODEL IN FIBRE MODELLING

A series of experimental tests on reinforced concrete bridge piers have been performed in the ELSA laboratory at Ispra. Simultaneously, a classic fibre model was used to predict the response of those structures under cyclic loading. The comparison of the experimental results with the numerical results pointed out the importance of developing a model to represent the non-linear shear behaviour of squat piers. In that context, a model based on a strut-and-tie type formulation was developed and implemented in CASTEM 2000.

The model is coupled with the classic fibre model which is briefly described below. Several aspects of the strut-and-tie formulation are presented and discussed and the implementation procedures are reviewed.

3.1 Fibre model

The fibre model in CASTEM 2000 is implemented in a three-dimensional Timoshenko beam element [17]: plane sections remain plane after being deformed but do not, necessarily, maintain the initial angle with the beam axial axis (see Figure 3.2). With this element, different interactions between axial and shear forces and bending moments can be considered. The complexity of the model depends on the complexity of the constitutive laws representing the behaviour of the materials. To take into account the non-linear behaviour in shear, a multi-dimension formulation for monotone increasing load using the Mazars concrete model was attempted with promising results [18]. However, typically a fibre model considers axial stress-strain constitutive laws uncoupled with linear elastic shear behaviour laws at each fibre.

A fibre model is a refined way of analysing the state of a section within a structure. The structure is divided in three-dimensional linear elements which are sub-divided in longitudinal fibres defining a mesh in the transverse section.

Given a loading history, a numerical step-by-step procedure is used to calculate the value of the shear and axial strain and the rotation along the three main axis of each Gauss point of each element, as in any three-dimensional beam model. Then, making use of the

assumptions of the Timoshenko beam element, the program goes deeper in the cross-section and computes the strain at each Gauss point *i* of each fibre through the equations of compatibility of displacements (see Figure 3.2)

$$\begin{aligned}(\varepsilon_x)_i &= \varepsilon_x - y_i c_z + z_i c_y \\ (\gamma_{xy})_i &= \gamma_{xy} - z_i c_x \\ (\gamma_{xz})_i &= \gamma_{xz} + y_i c_x\end{aligned} \qquad 3.1$$

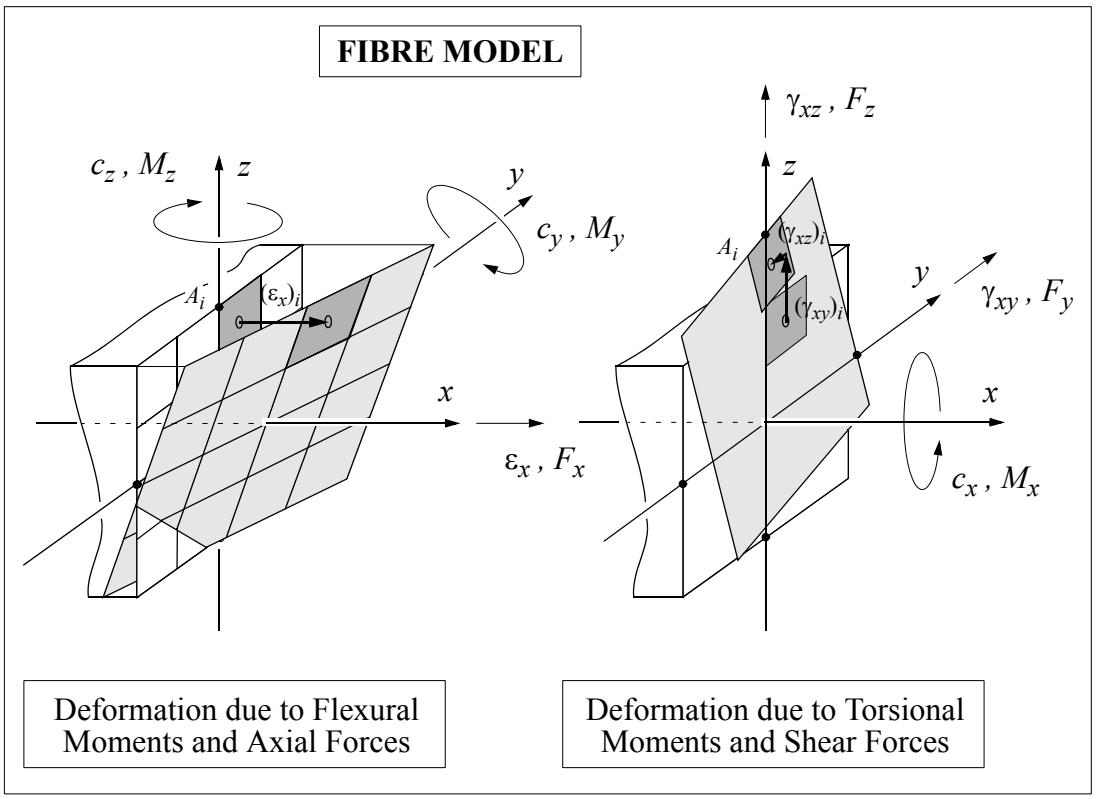

Figure 3.1 - Fibre model - deformation of the transverse section

No warping of the cross-section is considered. A constant unitary function is adopted for the distribution of shear strain in the transverse section and a linear elastic behaviour model is considered for shear forces. With the strain values and the constitutive laws for the materials, the axial stress σ_i and the shear stresses, $(\tau_{xy})_i$ and $(\tau_{xz})_i$, are computed and integrated in the section. The final solution is found when the equilibrium of forces is respected,

$$
\begin{aligned}
F_x &= \int_S \sigma_x dS \\
F_y &= \int_S \tau_{xy} dS \\
F_z &= \int_S \tau_{xz} dS \\
M_x &= \int_S (-z \cdot \tau_{xy} + y \cdot \tau_{xz}) dS \\
M_y &= \int_S (z \cdot \sigma_x) dS \\
M_z &= \int_S (-y \cdot \sigma_x) dS
\end{aligned}
\qquad 3.2
$$

Thus, in a fibre model the global response curve represents the integral of the local state of each section at the level of each Gauss point of each fibre. The global moment versus curvature curve is not defined a prior but it is the result of the integral of all the section forces. Any variation of the axial force and/or application of biaxial bending moments is automatically taken into account in the equilibrium equations.

The model implemented in CASTEM 2000 considers four Gauss points per fibre and one per beam element. Furthermore, the formulation for the beam element refers to an axial axis which can be eccentric to the '*axis of gravity*' of the element.

3.2 Non-linear shear modelling

The global behaviour of reinforced concrete columns with low shear span ratio is strongly influenced by shear forces and this effect must be considered in the response. Classic fibre models, like the one originally implemented in CASTEM 2000 and described above, consider a linear elastic behaviour law for shear; the fibres belonging to the same section '*see*' the same shear strain and contribute to the final force proportionally to their area and distortional modulus. The influence of the stirrups is neglected and it interferes only in the concrete core axial stress-strain law through the confinement effect; it modifies the peak value and the after peak softening behaviour, increasing the strength and rigidity of the concrete.In order to consider the influence of the non-linear behaviour in shear, a formulation based on a strut-and-tie model, coupled with the classic fibre model for flexural forces, is developed.

Figure 3.3 illustrates the main internal resisting forces in a short cantilever beam dam-

aged by a transverse and longitudinal force applied at the extremity. The resisting elements along the cracks are the steel reinforcing bars which tie both sides of the crack together, and the concrete through the aggregate interlock effect (see zoomed section 2 in Figure 3.3). Furthermore, the concrete also contributes to shear strength with its own shear resisting capacity and, above all, through a truss mechanism effect which is described hereafter.

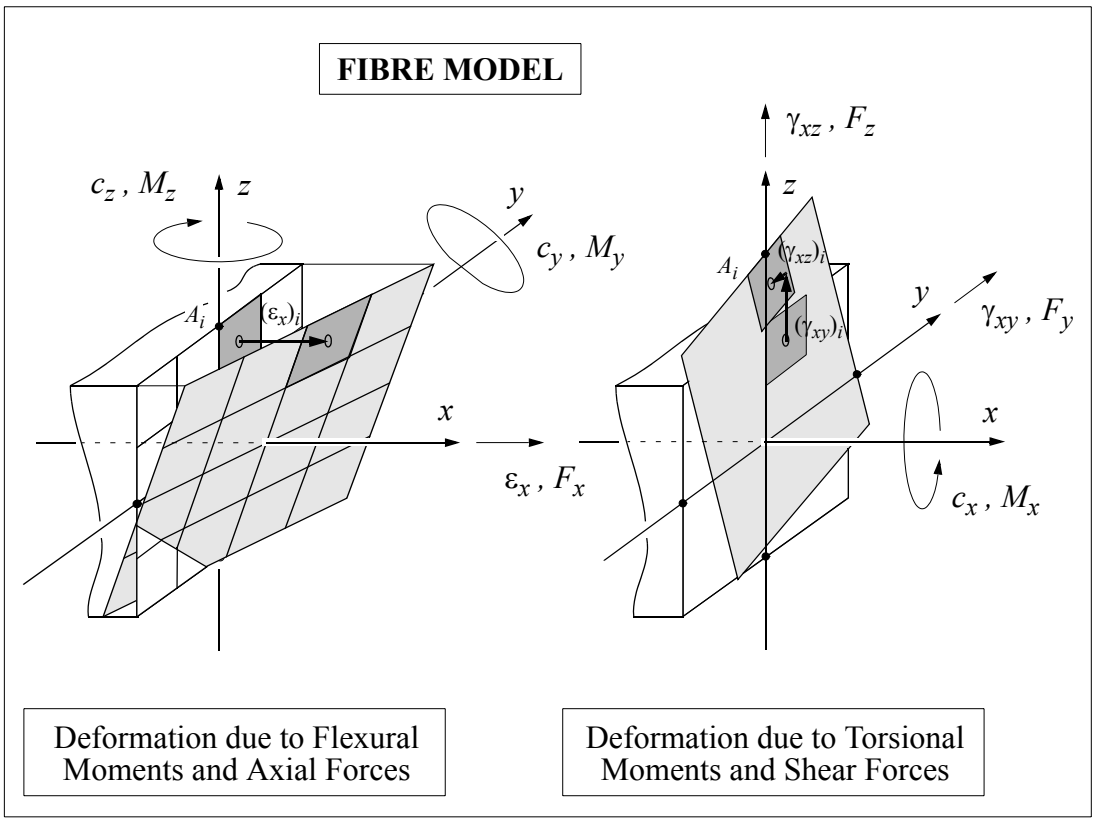

Figure 3.2 - Fibre model - deformation of the transverse section

In Figure 3.4, a short cantilever beam under shear forces, one can observe that a new structure appears from diagonal cracking analogous to a truss made of transverse and longitudinal steel ties and diagonal concrete struts. The non-linear shear model developed here is based on this analogy. Although the interlocking forces along the cracks and the dowel effect illustrated in Figure 3.3 are neglected in the present formulation, they are implicitly taken into account in the constitutive laws (see section 3.2.4).

Referring to Figure 3.4, the compatibility of displacements in the transverse direction is set out through the geometric analysis of the truss deformed by the axial force *P*, the

transverse force V and the bending moment M. Moreover, the two models interact through the '*average axial strain*' computed at the level of each transverse section. Actually, the coupling between the fibre and the strut-and-tie model is ensured by that deformation.

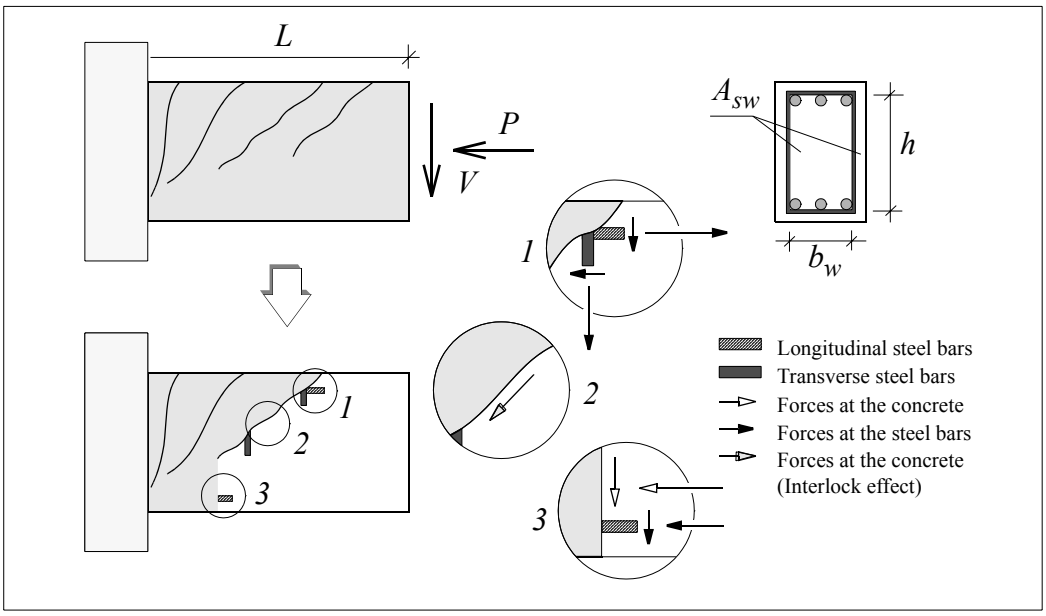

Figure 3.3 - Cracking pattern - internal acting forces

The algorithm for the case of shear force in one main transverse direction of the column is described in the next section. The equations of compatibility of displacements and equilibrium of forces are then described together with the constitutive laws at the strut and tie elements. The shear cracking angle and the cross-sectional area of the diagonal elements adopted in the model are discussed. The participation of the tensile strut in the global response and the possibility to consider a damage parameter at the diagonals are also referred to.

In the text, the words '*diagonal*' and '*strut*' are used indistinctly to refer to the concrete elements of the truss.

3.2.1 Compatibility equations

Two concrete diagonals are considered in the formulation. For each loading direction there is one strut under compression forces and another under tensile forces. In the case of shear forces in both main transverse directions of the element, the procedure described

for one direction is valid for the perpendicular direction and the two responses are superimposed.

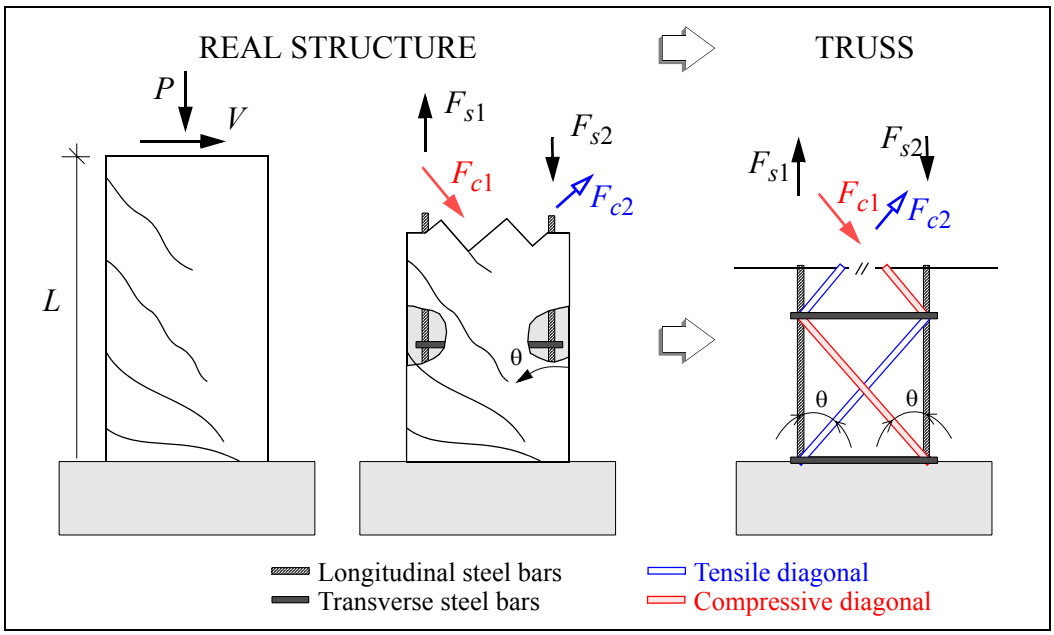

Figure 3.4 - Truss analogy

The struts are represented by their central axis. The same cracking angle is adopted for both diagonals, i.e., the two struts are symmetric in relation to the axis of the column. Note that the angle is a model parameter, in other words, it does not change during the loading history. The shear cracking angle is discussed later.

The diagonals represent the direction of the pseudo principal stresses. The word pseudo refers to the fact that the principal directions were estimated and not calculated through a Mohr's circle. This also means that the strut under tensile stresses is not always perpendicular to the compressed strut. The angle between the two pseudo principal directions is $(2 \cdot \theta)$, the two concrete diagonals being perpendicular one to the other only when $(\theta = 45^{o})$ (see Figure 3.5).

To establish the equations of compatibility of displacements, the deformation due to shear forces is set apart from the average axial deformation due to bending moments and axial forces. Assuming a cracking angle θ, as illustrated in Figure 3.5, the components j of the displacement of diagonal i, Δ_{ij}, are given by

$$\Delta_{11} = (h_v^* - h_v) \cdot (\sin\theta) \qquad \Delta_{12} = h_{oe} \cdot (\cos\theta)$$
$$\Delta_{21} = (h_v^* + h_v) \cdot (\sin\theta) \qquad \Delta_{22} = h_{oe} \cdot (\cos\theta) \qquad 3.3$$

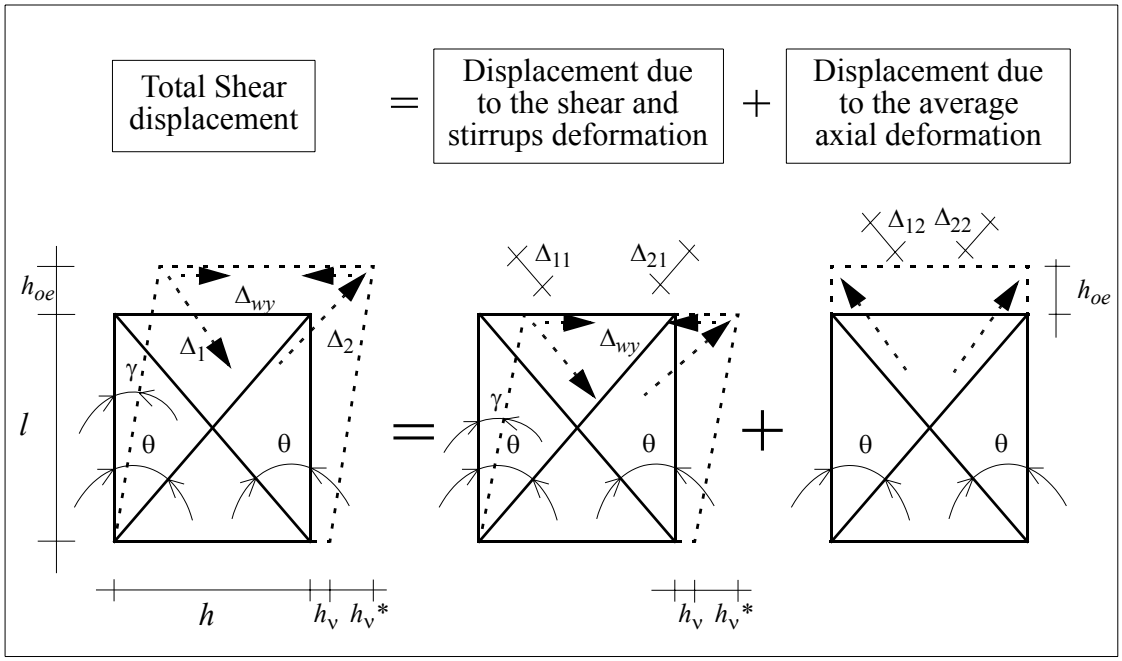

Figure 3.5 - Compatibility of displacements

where h_v, h_v^* and h_{oe}, are the displacements due to the stirrups strain ε_{wy}, to the shear deformation γ and to the average axial strain ε_{oe}, respectively,

$$h_v = \Delta_{wy} = \varepsilon_{wy} \cdot h$$
$$h_v^* = l \cdot \tan\gamma \qquad 3.4$$
$$h_{oe} = \varepsilon_{oe} \cdot l$$

The superimposition of the two partial displacements, ($\Delta_i = \Delta_{i1} + \Delta_{i2}$), gives the total displacement of each diagonal

$$\Delta_1 = (\varepsilon_{wy} \cdot h - l \cdot (\tan\gamma)) \cdot (\sin\theta) + \varepsilon_{oe} \cdot l \cdot (\cos\theta)$$
$$\Delta_2 = (\varepsilon_{wy} \cdot h + l \cdot (\tan\gamma)) \cdot (\sin\theta) + \varepsilon_{oe} \cdot l \cdot (\cos\theta) \qquad 3.5$$

These two expressions represent the compatibility of displacements to be respected in each transverse section. The uniform strain at the diagonals is obtained dividing both equations by the length of the diagonals, $l/(\cos\theta)$,

$$\varepsilon_1 = \frac{\Delta_1}{l/(\cos\theta)} = \varepsilon_{oe} \cdot (\cos\theta)^2 + \varepsilon_{wy} \cdot (\sin\theta)^2 - \frac{\tan\gamma}{2} \cdot (\sin(2\theta))$$
$$\varepsilon_2 = \frac{\Delta_2}{l/(\cos\theta)} = \varepsilon_{oe} \cdot (\cos\theta)^2 + \varepsilon_{wy} \cdot (\sin\theta)^2 + \frac{\tan\gamma}{2} \cdot (\sin(2\theta)) \qquad 3.6$$

The strains γ and ε_{oe} come directly from the 3D Timoshenko beam element algorithm. Instead, the stirrups strain, ε_{wy}, is computed internally at the level of the transverse section. This value must respect the equilibrium of forces inside the 3D element. The procedure used to calculate ε_{wy} is presented in section 4.2.

3.2.2 Equilibrium equations

With the deformation of each diagonal calculated through equation (3.6), the forces acting on the struts, F_{c1} and F_{c2}, and stirrups, F_{wy}, are computed through the constitutive laws of the materials (see Figure 3.6),

$$F_{c1} = \sigma_c(\varepsilon_1) \cdot A_{Sturt} = \sigma_c(\varepsilon_1) \cdot b_w \cdot h \cdot (\cos\theta)$$
$$F_{c2} = \sigma_c(\varepsilon_2) \cdot A_{Sturt} = \sigma_c(\varepsilon_2) \cdot b_w \cdot h \cdot (\cos\theta) \qquad 3.7$$
$$F_{wy} = f_{sw}(\varepsilon_{wy}) \cdot \frac{h/(\tan\theta)}{s} \cdot (2 \cdot A_{sw}) = f_{sw}(\varepsilon_{wy}) \cdot b_w \cdot h/(\tan\theta) \cdot \rho_{sw}$$

($\rho_{sw} = (2 \cdot A_{sw})/(b_w \cdot s)$) being a measure of the transverse steel ratio and σ_c and f_{sw}, respectively, the stresses at the concrete (struts) and stirrups (ties). The value A_{sw} is the cross-sectional area of the transverse steel, s the stirrups spacing and b_w and h the dimensions of the column transverse section (see Figure 3.3). The hysteretic curves adopted for both the concrete and the transverse steel are those already implemented in CASTEM 2000 for the fibre model and are presented in section 3.2.4.

The forces given by equation (3.7) must respect the internal and the external equilibrium in the structure:

- equilibrium of internal forces at point A (dashed lines in Figure 3.6):

$$F_{wy} + (F_{c1} + F_{c2}) \cdot (\sin\theta) = 0 \qquad 3.8$$

- equilibrium of total forces at the cross-section:

$$V + (F_{c1} - F_{c2}) \cdot (\sin\theta) = 0 \qquad 3.9$$

This system of equations is solved in two stages. Firstly, equation (3.8) is used to calculate the deformation of the stirrups, i.e., the strain at the transverse steel satisfying the compatibility of displacements and, at the same time, respecting the internal equilibrium in the element. Then, with ε_{wy}, the shear resisting force in the transverse section is computed and the equilibrium with the applied transverse force is checked (equation (3.9)).

Substituting equation (3.7) into equation (3.8) and equation (3.9), we obtain

$$f_{sw}(\varepsilon_{wy}) \cdot \rho_{sw} + (\sigma_c(\varepsilon_1) + \sigma_c(\varepsilon_2)) \cdot (\sin\theta)^2 = 0 \qquad 3.10$$

$$(\sigma_c(\varepsilon_2) - \sigma_c(\varepsilon_1)) \cdot b_w \cdot h \cdot (\sin\theta) \cdot (\cos\theta) = V \qquad 3.11$$

Note that the transverse steel ratio is taken into account in equation (3.10) and that it contributes to shear strength through the strains ε_1 and ε_2 at the struts in equation (3.11).

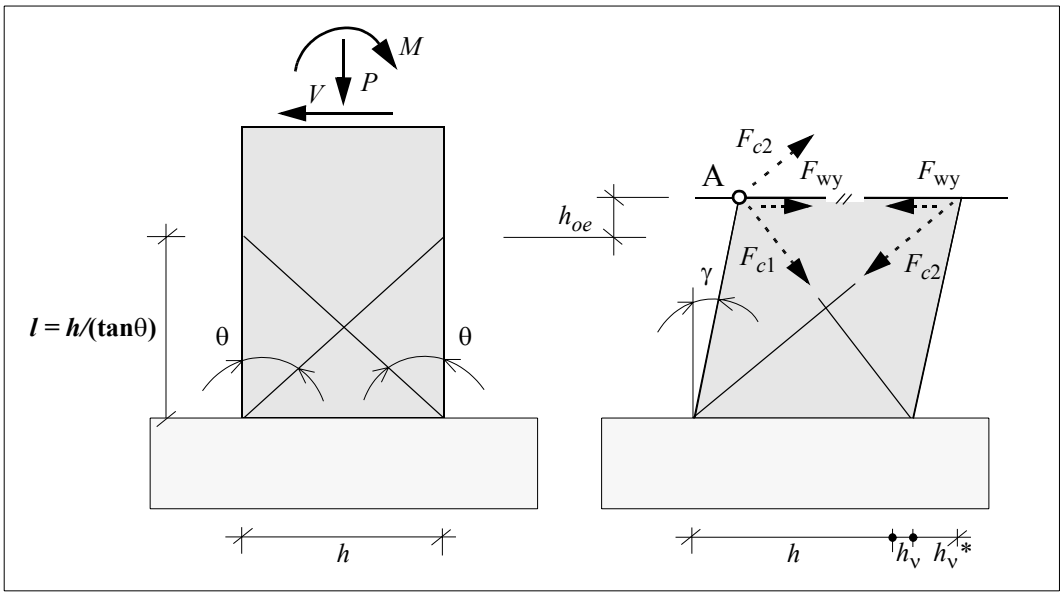

Figure 3.6 - Internal forces in the section

3.2.3 Damage of the struts

Damage of concrete due to flexural and axial forces can be included in the non-linear shear model not only through the average axial strain, as described in section 3.2.1, but also through a damage parameter that would represent the state of the transverse section due to those forces. Actually, with this procedure, the decrease in the concrete shear

strength of R/C columns under cyclic loading for increasing flexural displacement ductility can be described in a more suitable way. Different cumulative damage parameters can be used; from a simple parameter proportional to the maximum compression strain computed at the concrete core area of the cross-section, to more sophisticated parameters that include the amount of energy dissipated during the loading history. Actually, this damage parameter establishes a supplementary link between the longitudinal fibres and the strut-and-tie model.

In this case, two internal variables, D_1 and D_2, one per diagonal, have to be included in the model. These two parameters allow damage due to loading in one direction to be '*independent*' from loading in the opposite direction. Thus, equation (3.7) for the force at the concrete struts is modified to

$$F_{ci} = \sigma_c(\varepsilon_i) \cdot (1 - D_i) \cdot b_w \cdot h \cdot (\cos\theta) \qquad 3.12$$

which corresponds to substituting the stresses at the diagonals, $\sigma_c(\varepsilon_i)$, by

$$(\sigma_c^*)_i = \sigma_c(\varepsilon_i) \cdot (1 - D_i) \qquad 3.13$$

where $(i = 1, 2)$ refers to each strut. In the numerical tests illustrated in the present report this link has not been considered, $(D_i = 0)$.

3.2.4 Constitutive laws. Tensile strut

The axial stress versus strain laws used for the concrete and steel in the strut-and-tie model are the same as the ones used for the longitudinal fibres. However, the parameters that control the crack-closing and the tension-stiffening effect may present different values. Note that a non-linear shear model like the one considered in this report, attempts to reproduce the response of a structure through the behaviour of just three elements per cross-section: two made of concrete and one made of steel. This means that it is not possible for the model to '*disguise*' any singularity present in the axial stress-strain response curve of these three elements. For example, cracking of a diagonal or yielding of transverse steel occurs throughout the cross-sectional area of the strut or tie. Instead, in the bending fibres that only occurs at one Gauss point of one of the fibres in the cross-section.

Therefore, to properly represent the global shear stress versus strain response curve of the structure and to avoid numerical problems, smooth axial stress versus strain constitutive laws have to be used to '*hide*', as much as possible, the particularities in the behaviour of the steel and the concrete. Special care is given to the crack-closing and tension-stiffening phenomena.

Concrete constitutive model

The model used for the concrete follows a law of Hognestad type with two branches: a hardening branch before the compression peak followed by a softening branch until a residual compression plateau. The model represents the confinement effect of transverse steel through a parameter which increases the strength and post-peak stiffness of the concrete. Tensile stresses are included through a linear model with a post-peak softening behaviour. The equations used in the model and a brief description of the phenomena involved can be found in [17].

For cyclic loading, the model follows empiric based rules. To take into account phenomena like crack closing, stiffness degradation and tension stiffening, loading and unloading laws are considered and represented by an exponential equation. Different parameters are prescribed for unloading and reloading cycles.

An arbitrary axial stress-strain cyclic history is represented in Figure 3.7. The circles indicate either the extremities of the different branches of the hysteretic curve or the points where the load changes direction. Thus, before reaching the softening branch of the tensile stress-strain curve, the unloading curve from the compression envelope is described by a straight line with growing stiffness degradation given by

$$E_d = E_e\left(1 - \frac{(\varepsilon^*_{max})^2}{1 - \varepsilon^*_{max} + (\varepsilon^*_{max})^2}\right) \qquad 3.14$$

where E_e is the Young modulus of the virgin concrete and ($\varepsilon^*_{max} = \varepsilon^c_{max} / \varepsilon^c_o$) is the maximum compression strain ever reached during the loading history ε^c_{max} normalized by the strain at the peak compression stress ε^c_o. After that point, if loading changes direction, both the unloading and reloading curves follow an exponential type curve. Taking

as an example the loading curve from point 4 to point 5, the response is described by the equation

$$\sigma(\varepsilon) = (\sigma^* - \sigma'_4 \cdot \varepsilon^*) \cdot \left(\frac{\varepsilon - \varepsilon_4}{\varepsilon^*}\right)^{\left[(\sigma'_5 - \sigma'_4) \cdot \frac{\varepsilon^*}{\sigma^* - \sigma'_4 \cdot \varepsilon^*}\right]} + \sigma'_4 \cdot (\varepsilon - \varepsilon_4) + \sigma_4 \qquad 3.15$$

where $(\sigma^* = \sigma_5 - \sigma_4)$, $(\varepsilon^* = \varepsilon_5 - \varepsilon_4)$ and σ'_4 and σ'_5 are the tangents of the curve at points 4 and 5, respectively.

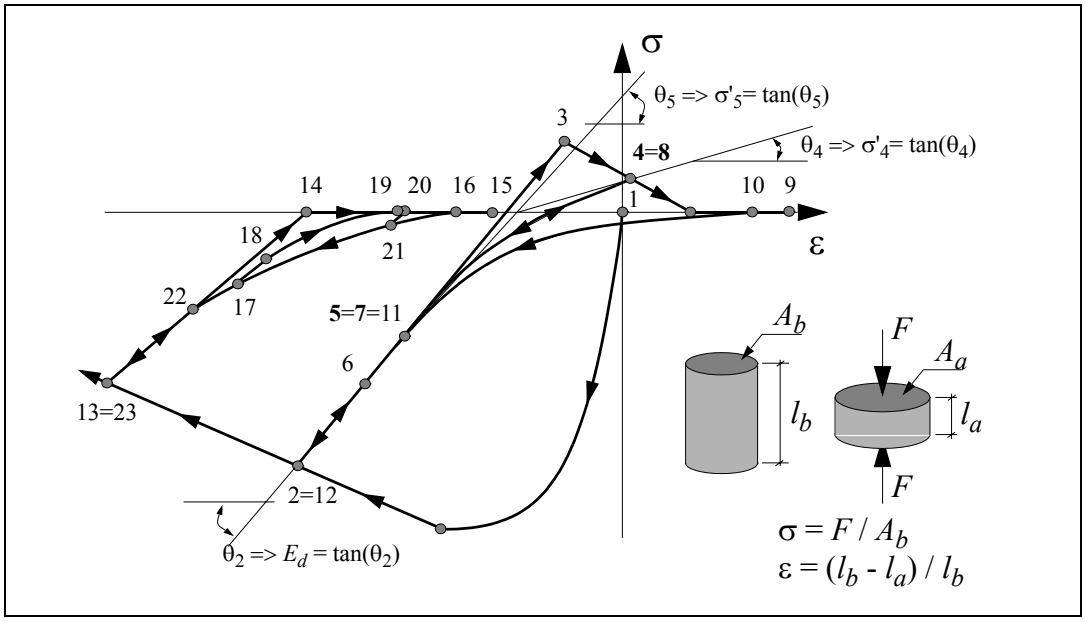

Figure 3.7 - Axial stress-strain constitutive law for concrete

To define the exponential curve, four parameters, F_1, F'_1, F_2 and F'_2, two per each extreme point, are used. Taking now the unloading curve from point 7 to point 8 and the reloading curve from point 10 to point 11, the following expressions are obtained:

- Unloading curve (7-8):

$$\begin{aligned}
&(\sigma_7 = \sigma^c_{max}/F_1) \Rightarrow (\varepsilon_7 = \varepsilon^c_{max} - (\sigma^c_{max} - \sigma_7)/E_d) \\
&(\sigma_8 = \sigma^t_{max} > 0) \Rightarrow (\varepsilon_8 = \varepsilon^t_{max} \wedge \varepsilon_8 \geq \varepsilon_{pla}) \\
&\sigma'_7 = \frac{\sigma_7}{(\varepsilon_7 - \varepsilon_8)/F'_1} \qquad 3.16 \\
&\sigma'_8 = \frac{\sigma_7}{(\varepsilon_7 - \varepsilon_8) \cdot F'_2}
\end{aligned}$$

ε_{pla} being the deformation at zero stress when unloading from the envelope curve, ε^{t}_{max} the maximum strain ever reached since last unloading from the monotonic curve and σ^{t}_{max} the maximum tensile stress still available. For this particular curve $(\varepsilon_{pla} = \varepsilon_2 - \sigma_2 / E_d)$ and $(\varepsilon_{max} = \varepsilon_4)$.

In addition, the following conditions must hold true,

$$\left(\sigma'_7 < \frac{\sigma_7}{(\varepsilon_7 - \varepsilon_{pla}) - 1/10 \cdot (\varepsilon_{pla} - \varepsilon_8)}\right) \wedge (\sigma'_7 < E_d)$$
$$\left(\sigma'_8 > \frac{\sigma_8}{9/10 \cdot (\varepsilon_8 - \varepsilon_{pla})}\right) \qquad 3.17$$

In the case $(\sigma^{t}_{max} = 0)$, as for curve (18-19), the strain at point 19 is given by

$$\varepsilon_{19} = \varepsilon_{pla} + (F_2/2) \cdot (\varepsilon^{t}_{max} - \varepsilon_{pla})$$

- Reloading curve (10-11):

$$(\sigma_{10} = \sigma^{t}_{max} = 0) \Rightarrow (\varepsilon_{10} = \varepsilon_{pla} + F_2 \cdot (\varepsilon^{t}_{max} - \varepsilon_{pla}))$$
$$(\sigma_{11} = \sigma^{c}_{max} / F_1) \Rightarrow (\varepsilon_{11} = \varepsilon^{c}_{max} - (\sigma^{c}_{max} - \sigma_{11})/E_d)$$
$$\sigma'_{10} = \frac{\sigma_{11}}{(\varepsilon_{11} - \varepsilon_{10}) \cdot F'_2} \qquad 3.18$$
$$\sigma'_{11} = \frac{\sigma_{11}}{(\varepsilon_{11} - \varepsilon_{10})/F'_1}$$

where $(\varepsilon_{max} = \varepsilon_9)$. In addition, the following conditions must hold true,

$$\sigma'_{10} > \frac{\sigma_{10}}{9/10 \cdot (\varepsilon_{10} - \varepsilon_{pla})}$$
$$\left(\sigma'_{11} < \frac{\sigma_{11}}{(\varepsilon_{11} - \varepsilon_{pla}) - 1/10 \cdot (\varepsilon_{pla} - \varepsilon_{10})}\right) \wedge (\sigma'_{11} < E_d) \qquad 3.19$$

The choice of the parameters of the exponential curve must be made taking into account that the axial stress-strain behaviour law of the concrete should represent what happens in the whole diagonal concrete element, in other words, it should integrate the bi-axial state of the concrete. Thus, the parameters may assume different values when representing the behaviour of the struts or of the concrete longitudinal fibres. The interlocking and

the dowel effect can be implicitly taken into account through these parameters.

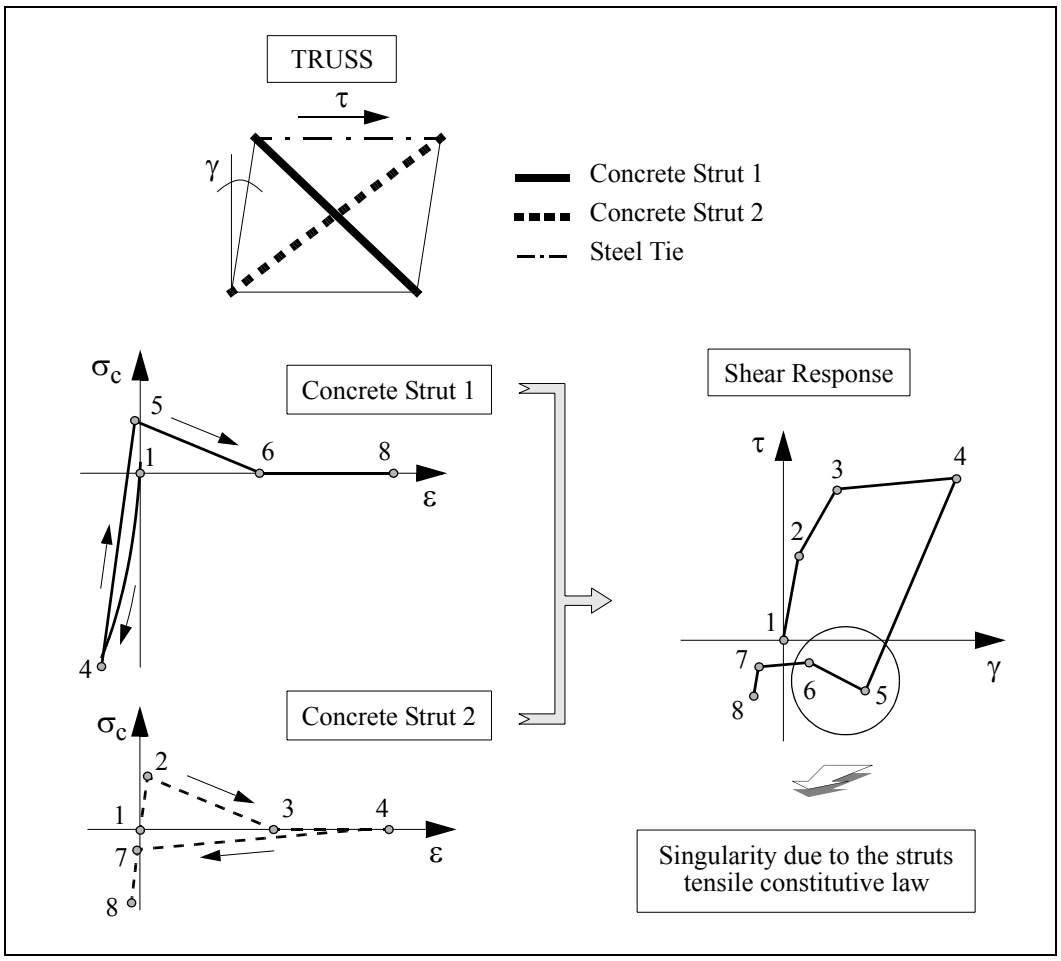

Figure 3.8 - Influence of the tensile behaviour law in the shear stress versus strain response curve

Concerning the contribution of the tensile stresses to the shear response, it should be also pointed out that:

a) to properly represent the shear force-displacement behaviour before yielding of the longitudinal steel bars, tensile stresses should be considered at the struts;

b) the tensile constitutive law at the diagonals should be carefully chosen so that an anomalous behaviour like the one described hereafter and illustrated in Figure 3.8 be avoided. When unloading after an important monotonic loading, the tensile strut discharges along the zero stress line (already fully cracked and still virgin in compression) and the shear stress is controlled by the compressed strut (see equation (3.9)) which, on the other hand, also depends on the transverse steel behaviour law. After

decreasing to zero, the stress in the compressed strut increases up to the tensile peak (still virgin in tension) and it decreases again following the softening branch of the tensile concrete curve (see Figure 3.8). Since the shear stresses follow the strut, they respond in the same way: a peak shear stress-strain point followed by a softening curve. This behaviour is, of course, anomalous and should be avoided;

c) as the non-linear shear model considers the diagonals to be symmetrical to the column axis, only for ($\theta = 45^o$) are the diagonals perpendicular to each other. Note that this angle defines the direction of the principal compression stresses. Thus, when the cracking angle is different to 45^o, the strain at the tensile strut does not correspond to the strain in the direction perpendicular to the compressed strut but to a value closer to the strain in the compressed strut. This means that the peak tensile stress is reached at the strut after being reached at the pseudo principal tensile direction, in other words, the diagonal under tensile strains is delayed in relation to the principal direction;

d) finally, although shear and flexural algorithms follow similar concrete constitutive laws, there is no link between them concerning tensile behaviour. The two elements may reach cracking at different steps of the loading history.

To take these aspects in consideration, the model of the concrete under tensile forces was changed; the tensile strength of the struts is no longer a parameter of the model but it depends on the deformation of the longitudinal fibres. The strut reaches the peak tensile strength when the average axial deformation of the cross-section, ε_{oe}, reaches the peak tensile stress of the concrete of the longitudinal fibres. This solution introduces an additional link between the flexural and the shear model. Furthermore, and to take into account that the concrete model should represent the global behaviour of the struts, the post-peak tensile softening branch adopted for the concrete at the shear model is usually much smoother than at the longitudinal fibres.

Steel constitutive model

The constitutive law used for the cyclic behaviour of the steel bars is the explicit formulation of Menegotto-Pinto [19]. The transverse steel follows the rules of this model for both monotonic or cyclic loading histories (see Figure 3.9). Note that in the case of the

steel of the longitudinal bars, steel follows first the monotonic curve (elastic branch, plateau and hardening branch) and only when, or if, an important unloading after yielding occurs is the hysteretic Menegotto-Pinto model activated. The model is described in [17] and it is given by

$$\sigma^* = b \cdot \varepsilon^* + \left(\frac{(1-b)}{(1+(\varepsilon^*)^R)^{1/R}} \right) \cdot \varepsilon^* \qquad 3.20$$

where

$$\sigma^* = \frac{\sigma_s - \sigma_r}{\sigma_o - \sigma_r} \qquad \varepsilon^* = \frac{\varepsilon_s - \varepsilon_r}{\varepsilon_o - \varepsilon_r} \qquad R = R_o - \frac{a_1 \xi}{a_2 + \xi} \qquad 3.21$$

This equation defines a family of transition curves between two asymptotes with slopes E_o and E_h having (ε_o,σ_o) as a common point (see Figure 3.9). The pair of values (ε_r,σ_r) are the coordinates of the reversal loading point. Furthermore, b factor represents the slope hardening ratio, that is, the ratio between the hardening slope E_h and the initial slope E_o and R defines the shape of the curve. This last parameter depends on ξ which measures the maximum strain ever reached in the loading direction, the value at point 2 in the case of curve (5-6) in Figure 3.9, in relation to (ε_o,σ_o), normalized by $(\varepsilon_o - \varepsilon_r)$. In the case of curve (5-6), the reversal loading point coincides with point 5 and point 2 represents the maximum strain ever reached in the loading direction, i.e.,

$$\xi = \frac{\varepsilon_2 - \varepsilon_o}{\varepsilon_o - \varepsilon_5} \qquad 3.22$$

The values R_o, a_1 and a_2, are parameters of the steel behaviour model.

The monotonic curve was not considered in the constitutive law of the transverse steel to avoid the plateau zone after yielding interfering negatively in the shear stress versus strain response curve.

3.2.5 Shear '*cracking*' angle

In the formulation described in this report, it is assumed that the cracking angle, better, the strut angle θ, is a model parameter. It is computed through the geometrical characteristics of the structure and of the longitudinal and transverse steel reinforcement ratio;

knowing the structure and the type of loading to be applied, with or without important axial forces, semi-empirical expressions can be used to find a suitable value for θ. In the next paragraphs a very simple approach described in [11] is presented.

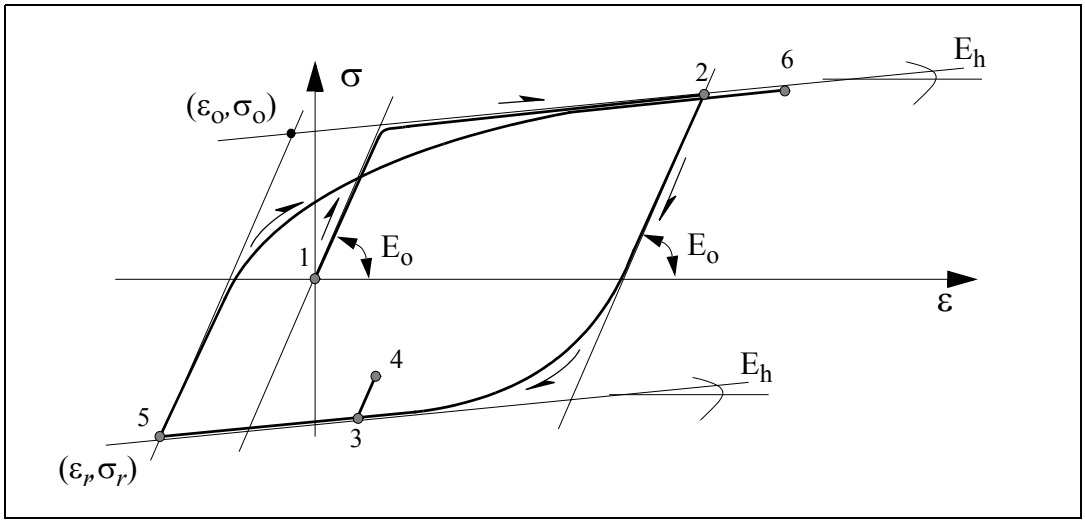

Figure 3.9 - Axial stress-strain constitutive law for steel

Cracking limit analysis

In this first approach, the crack inclination angle is calculated through the analysis of three possible shear failure modes in membrane type elements, namely: a) yielding of the steel in both directions with no crushing of the concrete, b) yielding of the steel in the weak direction with concrete crushing and the steel in the strong direction remaining elastic and, finally, c) crushing of the concrete without yielding of the steel. In the case of columns the in-plane steel grid corresponds to the longitudinal and transverse steel bars. The strong and weak directions are the longitudinal and transverse directions of the beam, respectively (see Figure 3.10).

For each of the failure modes a different expression is found for the inclination angle of the principal compression stress at failure θ [20]:

- yielding of both reinforcements without crushing of the concrete,

$$\tan\theta = \sqrt{\frac{\rho_{sw} \cdot f_{sw}}{\rho_s \cdot f_{sy}}} \qquad 3.23$$

where

$$\rho_s = \frac{A_{sl}}{h b_w} \qquad \rho_{sw} = \frac{A_{sw}}{s b_w} \tag{3.24}$$

are the longitudinal, ρ_s, and transverse steel ratios, ρ_{sw}, with A_{sl} and A_{sw} the steel reinforcing areas, f_{sw} and f_{sy} the correspondent yielding stresses, b_w and h the width and the length of the core of the cross-section and s the spacing of the stirrups. The shear stress corresponding to that failure mode is given by

$$\tau_u = \sqrt{\rho_{sw} \cdot \rho_s \cdot f_{sy} \cdot f_{sw}} \tag{3.25}$$

- yielding of the transverse reinforcement without yielding of the longitudinal steel bars and crushing of the concrete,

$$\sin\theta = \sqrt{\frac{\rho_{sw} \cdot f_{yw}}{f_{cd}}} \tag{3.26}$$

f_{cd} being the concrete strength and the shear failure stress given by

$$\tau_u = \sqrt{(f_{cd} - \rho_{sw} \cdot f_{sw}) \rho_{sw} \cdot f_{yw}} \tag{3.27}$$

- crushing of the concrete without yielding of both transverse and longitudinal reinforcements,

$$(\theta = 45^o) \wedge \left(\tau_u = \frac{1}{2} \cdot f_{cd}\right) \tag{3.28}$$

In this case the element is subjected to pure shear.

From the three possible failure modes, the governing mode is the one corresponding to the lowest τ_u value. Nevertheless, and according to this formulation, the crack inclination angle is not to be taken less than a minimum given by

$$\tan\theta_{min} = \frac{h}{2L} \tag{3.29}$$

Experimental results obtained at the ELSA laboratory on squat piers showed cracking angles that were not in agreement with the values calculated with this formulation (see section 5.2.3). Thus, another algorithm making use of the compression forces at the strut

and of the tensile forces at the steel longitudinal and transverse bars was developed for columns. The cracking angle is computed through the equilibrium of the horizontal and vertical forces in a cracked column. This formulation is named '*cracking equilibrium model*' and is presented hereafter.

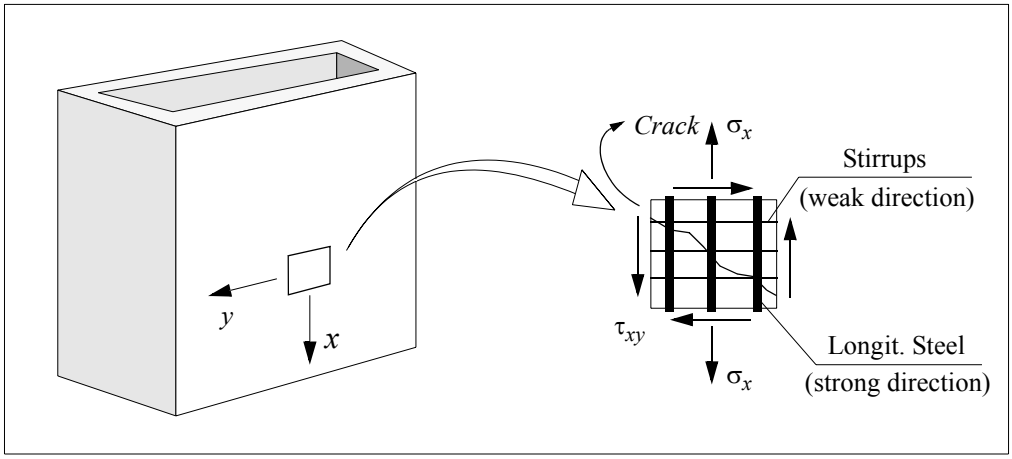

Figure 3.10 - Analogy with a membrane

Cracking equilibrium model

In this new approach, the critical cracking angle is established through the equilibrium of forces in two resisting mechanisms: one made of a concrete strut going from the top to the bottom of the column and transmitting the applied axial forces to the basement (see Priestly [12]) and a truss made of concrete struts and transverse and longitudinal steel ties. Since in the analysis the column is assumed to be cracked, no tensile strength is considered in the concrete.

The equilibrium is established on the transverse and longitudinal direction of the column. As illustrated in Figure 3.11 the equilibrium in the transverse direction is given by

$$V = F_{cs} \cdot \sin\theta - P \cdot \tan\alpha \qquad 3.30$$

F_{cs} being the compression force in the strut (positive) within the truss mechanism, and P the compression axial force (negative) on the top of the column.

In the longitudinal direction of the column, the axial force is transferred directly to the concrete compression zone at the basement, without passing through the truss. Thus, the equilibrium on the longitudinal direction gives the force at the concrete strut, F_{cs}, which

must be in equilibrium with the remaining compression force,

$$F_{cs} \cdot \cos\theta = -(F_c - P) \tag{3.31}$$

Substituting equation (3.30) into equation (3.31), the angle θ is given by

$$\tan\theta = \frac{V + P \cdot \tan\alpha}{P - F_c} \tag{3.32}$$

Knowing the distribution of flexural moments along the longitudinal axis of the structure $\overline{ox}$, $M(x)$, equation (3.32) becomes

$$\tan[\theta(x)] = \left(\frac{dM(x)}{dx} + P \cdot \tan\alpha\right) / (P - F_c) \tag{3.33}$$

To simplify the next steps, a cantilever element with a transverse force V at the top, as it is illustrated in Figure 3.11, is adopted, ($M(x) = V \cdot x$).

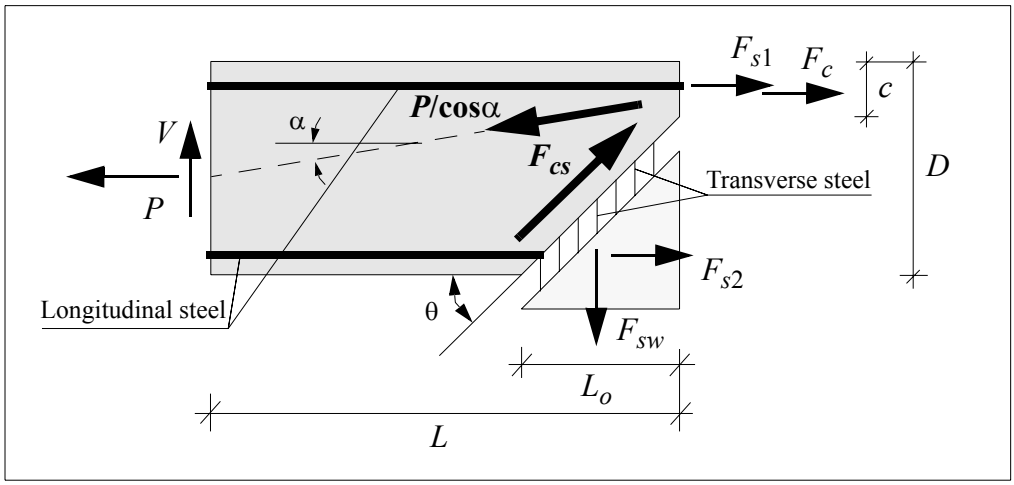

Figure 3.11 - Cracking equilibrium model

Therefore, given a structure and the applied axial force, the moment versus curvature history, $M(\phi)$, and the compression force at the concrete, $F_c(\phi)$, can be computed at any transverse section, in particular at the critical section (in this case at the bottom near the basement, ($x = L - L_o/2$)). Substituting these two values in equation (3.33), the cracking angle is given by

$$\tan[\theta(\phi)] = \left(\frac{M(\phi)}{(L - L_o/2)} + P \cdot \tan\alpha\right) / (F(\phi)) \tag{3.34}$$

where $(\tan\alpha = (D - c(\phi))/(2L))$ and $(F(\phi) = P - F_c(\phi))$. Furthermore, as illustrated in Figure 3.11, L_o also depends on the cracking angle,

$$L_o = \frac{D - c(\phi)}{\tan\theta} \qquad 3.35$$

$c(\phi)$ being the width of the compression zone. Substituting this value in equation (3.34), a polynomial of the second degree is obtained for $(\tan\theta)$,

$$F(\phi)\cdot(\tan\theta)^2 - \left(\tan\alpha\cdot(F(\phi)+P) + \frac{M(\phi)}{L}\right)\cdot\tan\theta + P\cdot(\tan\alpha)^2 = 0 \qquad 3.36$$

The history of flexural moments, the compression forces in the concrete and the width of the compression zone, are calculated through the fibre model. However, the resulting transverse force, $(F_c\cdot\sin\theta)$ must also be in equilibrium with the tensile force in the stirrups crossing the diagonal crack, F_{sw}. Using equation (3.30) and assuming an elastic perfectly plastic material for the transverse steel, the equilibrium is given by

$$\frac{M}{(L - L_o/2)} + P\cdot\tan\alpha \le f_{yw}\cdot\rho_{sw}\cdot b_w\cdot L_o \qquad 3.37$$

where f_{yw} is the yielding stress of the transverse steel, ρ_{sw} is the volumetric transverse steel ratio and b_w is the width of the transverse section.

Finally, substituting equation (3.35) into equation (3.37), we obtain

$$\left(P\cdot\tan\alpha + \frac{M(\phi)}{L}\right)\cdot(\tan\theta)^2 - (\tan\alpha\cdot(P\cdot\tan\alpha + B))\cdot\tan\theta + B\cdot(\tan\alpha)^2 < 0 \qquad 3.38$$

where $(\tan\theta > 0)$ and $(B = 2\cdot L\cdot f_{yw}\cdot\rho_{sw}\cdot b_w)$. The cracking angle in the model is the angle satisfying both equation (3.36) and equation (3.38), for a curvature corresponding to yielding of the longitudinal and/or of the transverse steel rebars (see the example in Figure 5.7).

3.2.6 Strut cross-section area

The angle θ defines the direction of cracking. Therefore, the orientation of the compressed strut, which contributes the most to shear strength, is correct. However, as both

diagonals are symmetric to the element axis, the tensile strut does not necessarily respect the perpendicularity to the direction of cracking. This means that, for angles not far from 45^o, the model is coherent but, whenever angles closer to 0^o or 90^o are forecasted, some adjustments must be made. In particular, the area of the transverse section A_{strut} must be carefully analysed.

As shown in Figure 3.12, the cross-sectional area of the diagonals is given by

$$A_{Strut} = b_w \cdot h \cdot (\cos\theta) \qquad 3.39$$

where b_w and h represent the dimensions of the effective shear resisting area, which usually corresponds to the concrete core area.

If the two extreme values ($\theta = 0^o$) and ($\theta = 90^o$) are considered in equation (3.39), the area of the cross-section of the struts is ($b_w \cdot h$) and zero, respectively. This means that for low cracking angles the total active area of the two diagonals can be almost twice the concrete core area and that it tends to zero when θ tends to 90^o. Therefore, equation (3.39) should be modified to take into account all possible range of angles from 0^o to 90^o.

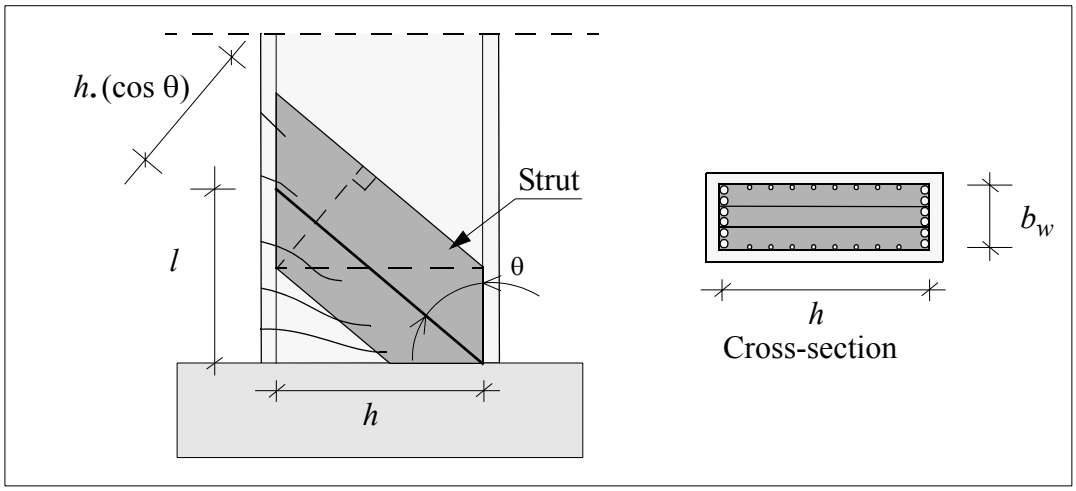

Figure 3.12 - Cross-sectional area of the struts

Since the two diagonals should represent the two principal strain directions, they should be, at each loading step, perpendicular to each other,

$$(A_{Sturt})_1 = b_w \cdot h \cdot (\cos\theta)$$
$$(A_{Strut})_2 = b_w \cdot h \cdot (\cos(90^o - \theta)) \qquad 3.40$$

Moreover, as a compressed strut becomes, with cyclic loading, a tensile strut and vice versa, the two diagonals should have the same cross-sectional area. Hence, the average value of the two areas in equation (3.40) has been adopted,

$$A_{Sturt}^* = \frac{(A_{Sturt})_1 + (A_{Strut})_2}{2} = b_w \cdot h \cdot \frac{\cos\theta + \sin\theta}{2} \qquad 3.41$$

and the transverse area given by equation (3.39) must be multiplied by

$$k_{As} = \frac{\cos\theta + \sin\theta}{2 \cdot \cos\theta} = \frac{1 + \tan\theta}{2} \qquad 3.42$$

3.3 Summary

A strut-and-tie type model coupled with the classic fibre model has been presented. To compile the information given in section 3.2, the main steps within the new formulation are schematically described in the next paragraphs. Thus,

1 • calculate the average axial strain ε_{oe} in the cross-section, using equation (3.1) from the bending model,

$$\varepsilon_{oe} = \left(\sum_i \varepsilon_i \cdot A_i\right) \Big/ \left(\sum_i A_i\right) \qquad 3.43$$

2 • admit an initial value for the transverse steel strain ε_{wy},

3 • establish the compatibility of displacements in equation (3.6). The shear strain is computed within the hypothesis of the Timoshenko beam element,

4 • with the strain in the struts and in ties and the constitutive laws for the materials, the forces in the elements of the truss are computed through equation (3.7),

5 • establish the equilibrium of internal forces within the transverse section. If the equilibrium is respected, go to the next step. Otherwise, estimate another value for

ε_{wy} and go to step 2,

6 • compute the shear reaction force in the transverse section using equation (3.11).

The new non-linear transverse forces substitute the values F_y and F_z in equation (3.2) and the algorithm used before in the fibre model is used again in the equilibrium of the external forces.

4 NUMERICAL IMPLEMENTATION

To implement the strut-and-tie model, a new fibre with special characteristics is added to the transverse section. It is made of concrete and steel and reacts to shear forces according to equation (3.9). As in the longitudinal fibres, four Gauss points are used. To distinguish this new element from the classic longitudinal fibres, in the report it is referred to as shear fibre. In the case that shear force exists in both principal directions of the transverse section, one shear fibre needs to be considered in each direction. If torsional moments also exist, the position and geometric characteristics of these new fibres must be carefully chosen. This topic is discussed later on.

In a classic fibre model the algorithm is straightforward; the program calculates, at each Gauss point of each three-dimensional element, the axial deformation, the rotation in the three directions and the shear strain in both transverse directions of the cross-section. Then, at each Gauss point of each fibre the program computes the axial strain through the equations of compatibility of displacements, and the internal stresses via the constitutive laws of the materials which are explicit in terms of strain. When dealing with shear fibres, an intermediate step has to be considered. The strain in the struts depends on the strain in the stirrups which is computed through the equilibrium of internal forces in the cross-section. This intermediate procedure requires an iterative algorithm.

This issue and other aspects linked to the implementation procedures, such as: the parameters of the model in CASTEM 2000, and the shear tangent stiffness used in the algorithm, are presented in the next sections. Finally, the possibility to represent torsional moments is discussed.

4.1 Parameters of the model in CASTEM 2000

The parameters for the shear fibre behaviour model in CASTEM 2000 are divided into three groups namely: one group with the parameters of the concrete constitutive law for the struts, another group with the parameters of the steel law for the ties and, finally, a third group with the specific parameters of the non-linear shear model. The first and the second group of parameters are described in [17]. The third group includes three parameters: the transverse steel ratio ρ, “ROST”, the shear cracking angle θ, “THET”, and a

parameter defining the ultimate state of the concrete (deformation, energy), “EULT”, which is used to define the struts damage *D*.

4.2 Strain in the transverse steel

Knowing the shear deformation arising from the 3D Timoshenko element, the equilibrium of internal forces in the cross-section is established and the strain in the stirrups is obtained through an iterative algorithm as described in section 3.3 and illustrated in Figure 4.1. This procedure is internal to the cycle of equilibrium of external forces.

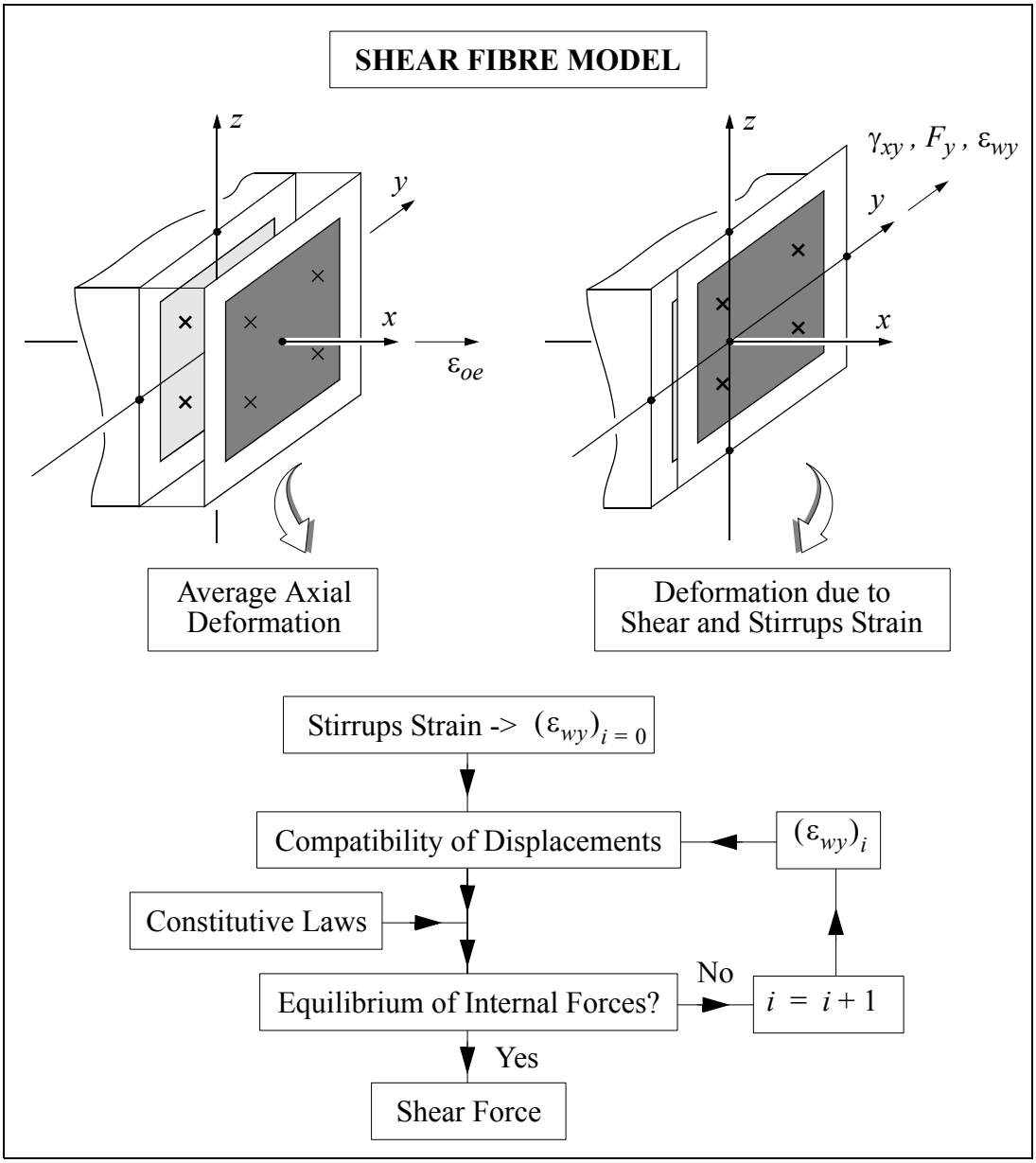

Figure 4.1 - Shear fibre model

The algorithm used to solve this internal step requires the equations of compatibility of

displacements to be formulated not in terms of total displacements but in terms of incremental displacements. Therefore, before describing the algorithm, the modifications performed to equation (3.6) are presented.

4.2.1 Equations of compatibility for incremental displacements

Referring to the equations of compatibility of displacements in section 3.2.1, if in equation (3.6) the deformation at loading step (i) is described as a function of the deformation at loading step $(i-1)$ plus an incremental value Δ, it becomes

$$\varepsilon_{k(i)} = \varepsilon_{k(i-1)} + \Delta\varepsilon_{k(i)} \qquad k = 1, 2 \tag{4.1}$$

where

$$\Delta\varepsilon_{k(i)} = \left[\Delta\varepsilon_{oe} \cdot (\cos\theta)^2 + \Delta\varepsilon_{wy} \cdot (\sin\theta)^2 + (-1)^k \cdot \frac{\tan\Delta\gamma}{2} \cdot (\sin(2\theta))\right]_{(i)} \tag{4.2}$$

However, since the cracking angle does not depend on the loading step,

$$\begin{aligned} \varepsilon_{oe(i)} &= \varepsilon_{oe(i-1)} + \Delta\varepsilon_{oe(i)} \\ \varepsilon_{wy(i)} &= \varepsilon_{wy(i-1)} + \Delta\varepsilon_{wy(i)} \\ \tan\gamma_{(i)} &= \tan(\gamma_{(i-1)} + \Delta\gamma_{(i)}) = \frac{\tan\gamma_{(i-1)} + \tan\Delta\gamma_{(i)}}{1 + \tan\gamma_{(i-1)} \cdot \tan\Delta\gamma_{(i)}} \end{aligned} \tag{4.3}$$

and $(1 + \tan\gamma_{(i-1)} \cdot \tan\Delta\gamma_{(i)} \cong 1)$, the two formulations, considering incremental displacements (equation (4.1)) or total displacements (equation (3.6)), are similar.

The iterative algorithm that solves the internal equilibrium in the cross-section follows the displacement incremental formulation in equation (4.1).

4.2.2 Equilibrium of internal forces - Iterative algorithm

As stated above, the behaviour of shear fibres depends on the average axial and shear strain in the transverse section and on the strain at the stirrups. The first two values come directly from the flexural fibre model. To calculate the third one, the equilibrium of internal forces is established in the cross-section through equation (3.10). However, since this equation is implicit on the transverse steel strain and functions σ_c and f_{sw} are non-linear,

an iterative process must be used.

The system to be solved is an equation with one unknown; so, a very simple iterative algorithm is adopted. It starts from the equilibrium at loading step $(l-1)$ and applies the equilibrium at the next step looking for the new strain at the stirrups. For a certain step (l) and iteration (j), the compatibility of displacements for the two diagonals becomes

$$[\varepsilon_{i(l)}]_{(j)} = [\varepsilon_{i(l)}]_{(j-1)} + [\Delta\varepsilon_{wy(l)}]_{(j)} \cdot (\sin\theta)^2 \qquad i = 1, 2 \tag{4.4}$$

where the strain in the stirrups is given by

$$[\varepsilon_{wy(l)}]_{(j)} = [\varepsilon_{wy(l)}]_{(j-1)} + [\Delta\varepsilon_{wy(l)}]_{(j)} \tag{4.5}$$

In the case $(j = 1)$,

$$[\varepsilon_{i(l)}]_{(0)} = \varepsilon_{i(l-1)} + \left[\Delta\varepsilon_{oe} \cdot (\cos\theta)^2 + (-1)^i \cdot \frac{\tan\Delta\gamma}{2} \cdot (\sin(2\theta))\right]_{(l)} \tag{4.6}$$
$$[\varepsilon_{wy(l)}]_{(0)} = \varepsilon_{wy(l-1)}$$

Considering now equation (3.10), the internal equilibrium must be respected allowing a maximum absolute error that should not be greater than an established tolerance (*Tol*),

$$R([\varepsilon_{wy(l)}]_{(j)}) = [\sigma([\varepsilon_{1(l)}]_{(j)}) + \sigma([\varepsilon_{2(l)}]_{(j)})] \cdot (\sin\theta)^2 + f_{sw}([\varepsilon_{wy(l)}]_{(j)}) \cdot \rho_{sw} \le Tol \tag{4.7}$$

where $R(\varepsilon_{wy})$ is the residual function. Ignoring pointer (l) and knowing that for small incremental values $\Delta\varepsilon$ one can write

$$F(\varepsilon + \Delta\varepsilon) \cong F(\varepsilon) + \frac{\mathrm{d}}{\mathrm{d}\varepsilon}F(\varepsilon) \cdot \Delta\varepsilon \tag{4.8}$$

equation (3.10) becomes linear in $\Delta\varepsilon_{wy(j)}$,

$$[\sigma(\varepsilon_{1(j-1)}) + \sigma(\varepsilon_{2(j-1)})] + [E_{ct}(\varepsilon_{1(j-1)}) + E_{ct}(\varepsilon_{2(j-1)})] \cdot \Delta\varepsilon_{wy(j)} \cdot (\sin\theta)^2 = \frac{-f_{sw}(\varepsilon_{wy(j-1)}) - E_{st}(\varepsilon_{wy(j-1)}) \cdot \Delta\varepsilon_{wy(j)}}{(\sin\theta)^2} \cdot \rho_{sw} \tag{4.9}$$

i.e,

$$\Delta\varepsilon_{wy(j)} \cong \frac{-f_{sw}(\varepsilon_{wy(j-1)}) \cdot \rho_{sw} - [\sigma(\varepsilon_{1_{(j-1)}}) + \sigma(\varepsilon_{2_{(j-1)}})] \cdot (\sin\theta)^2}{E_{st}(\varepsilon_{wy(j-1)}) \cdot \rho_{sw} + [E_{ct}(\varepsilon_{1_{(j-1)}}) + E_{ct}(\varepsilon_{2_{(j-1)}})] \cdot (\sin\theta)^4} \qquad 4.10$$

or,

$$\Delta\varepsilon_{wy(j)} = \frac{-R(\varepsilon_{wy(j-1)})}{E_{R_{(j-1)}}} \qquad 4.11$$

where ($E_{R_{(j-1)}} = \partial R(\varepsilon_{wy(j-1)}) / \partial(\varepsilon_{wy(j-1)})$) and $E_{ct}(\varepsilon)$ and $E_{st}(\varepsilon)$ are the axial tangent stiffness of struts and ties respectively.

Note that, occasionally, the convergence of the algorithm can be quite slow. During the numerical analysis performed with this algorithm, cases were found in which the residual function had a very smooth tangent which increased abruptly in a very narrow band around the zero of the function. In these cases, another algorithm was used to find the solution of equation (3.10): the bisection method applied to the residual function in equation (4.7). The convergence criterion was given by

$$\left|\varepsilon_{wy(j)} - \varepsilon_{wy(j-1)}\right| < 10^{-4} \cdot \varepsilon_{w,\,yield} \qquad 4.12$$

where $\varepsilon_{w,yield}$ is the yielding strain of the stirrups.

4.3 Shear tangent stiffness

The resolution of non-linear structural problems requires, very often, the tangent stiffness within each Gauss point of the element. For the shear fibres the tangent modulus is given by

$$\frac{\mathrm{d}}{\mathrm{d}\gamma}\tau(\gamma) = \frac{\mathrm{d}}{\mathrm{d}\gamma}(V/(b_w \cdot h)) \qquad 4.13$$

Substituting equation (3.11) in equation (4.13), one can write

$$\frac{\mathrm{d}}{\mathrm{d}\gamma}\tau(\gamma) \equiv \left(\frac{\partial}{\partial\varepsilon_2}\sigma_c(\varepsilon_2) \cdot \frac{\partial\varepsilon_2}{\partial\gamma} - \frac{\partial}{\partial\varepsilon_1}\sigma_c(\varepsilon_1) \cdot \frac{\partial\varepsilon_1}{\partial\gamma}\right) \cdot (\sin\theta) \cdot (\cos\theta) \qquad 4.14$$

Taking into account the dependency of ε_{oe} and ε_{wy} of γ,

$$\frac{\partial \varepsilon_i}{\partial \gamma} = \frac{\partial \varepsilon_i}{\partial \varepsilon_{oe}} \cdot \frac{\partial \varepsilon_{oe}}{\partial \gamma} + \frac{\partial \varepsilon_i}{\partial \varepsilon_{wy}} \cdot \frac{\partial \varepsilon_{wy}}{\partial \gamma} + \frac{\partial \varepsilon_i}{\partial \gamma} \qquad i = 1, 2 \tag{4.15}$$

and using the equation (3.6) of compatibility of displacements, the partial derivative becomes

$$\frac{\partial \varepsilon_i}{\partial \gamma} = (\cos\theta)^2 \cdot \frac{\partial \varepsilon_{oe}}{\partial \gamma} + (\sin\theta)^2 \cdot \frac{\partial \varepsilon_{wy}}{\partial \gamma} + \frac{(-1)^i}{2 \cdot (\cos\gamma)^2} \cdot (\sin(2\theta)) \tag{4.16}$$

Substituting now equation (4.16) into equation (4.14), the shear tangent stiffness is finally given by

$$\begin{aligned} \frac{\mathrm{d}}{\mathrm{d}\gamma}\tau(\gamma) &= \frac{\sin(2\theta)}{2 \cdot (\cos\gamma)^2} \cdot (E_{ct}(\varepsilon_1) + E_{ct}(\varepsilon_2)) \\ -\left((\cos\theta)^2 \cdot \frac{\partial \varepsilon_{oe}}{\partial \gamma} + (\sin\theta)^2 \cdot \frac{\partial \varepsilon_{wy}}{\partial \gamma}\right) &\cdot (E_{ct}(\varepsilon_1) - E_{ct}(\varepsilon_2)) \end{aligned} \tag{4.17}$$

The partial derivatives of the axial strain ε_{oe} and of the transverse steel strain ε_{wy} with respect to the shear strain γ are calculated through a sensitive analysis on the equation of equilibrium of internal forces. To calculate $(\partial \varepsilon_{wy} / \partial \gamma)$, the algorithm checks what happens to ε_{wy} when in equation (3.10) the shear strain is incremented by $\Delta\gamma$,

$$f_{sw}(\varepsilon_{wy} + \Delta\varepsilon_{wy}) \cdot \rho_{sw} + (\sigma_c(\varepsilon_1 + \Delta\varepsilon_1) + \sigma_c(\varepsilon_2 + \Delta\varepsilon_2)) \cdot (\sin\theta)^2 = 0 \tag{4.18}$$

with

$$\Delta\varepsilon_i = \Delta\varepsilon_{wy} \cdot (\sin\theta)^2 + (-1)^i \cdot \frac{\tan\Delta\gamma}{2} \cdot (\sin(2\theta)) \qquad i = 1, 2 \tag{4.19}$$

Using equation (3.10) and the hypothesis expressed in equation (4.8), the equation becomes linear in $\Delta\varepsilon_{wy}$,

$$\begin{aligned} &\Delta\varepsilon_{wy} \cdot [E_{st}(\varepsilon_{wy}) \cdot \rho_{sw} + (E_{ct}(\varepsilon_1) + E_{ct}(\varepsilon_2)) \cdot (\sin\theta)^4] \\ &= (E_{ct}(\varepsilon_1) - E_{ct}(\varepsilon_2)) \cdot (\sin\theta)^2 \cdot \frac{\sin(2\theta)}{2} \cdot \tan\Delta\gamma \end{aligned} \tag{4.20}$$

Since for small incremental values $(\Delta\varepsilon_{wy} / \Delta\gamma \cong \partial\varepsilon_{wy} / \partial\gamma)$ and $(\tan\Delta\gamma \cong \Delta\gamma)$, the derivative of the transverse steel stain with respect to shear strain becomes

$$\frac{\partial \varepsilon_{wy}}{\partial \gamma} \cong \frac{(E_{ct}(\varepsilon_1) - E_{ct}(\varepsilon_2)) \cdot (\sin\theta)^3 \cdot \cos\theta}{E_{st} \cdot \rho_{sw} + (E_{ct}(\varepsilon_1) + E_{ct}(\varepsilon_2)) \cdot (\sin\theta)^4} \qquad 4.21$$

Using the same procedure for the axial strain (i.e., check what happens to ε_{oe} when in equation (3.10) the shear strain is incremented by $\Delta\gamma$) the partial derivative of ε_{oe} with respect to the shear distortion is given by

$$\frac{\partial \varepsilon_{oe}}{\partial \gamma} \cong \frac{(E_{ct}(\varepsilon_1) - E_{ct}(\varepsilon_2))}{(E_{ct}(\varepsilon_1) + E_{ct}(\varepsilon_2))} \cdot \tan\theta \qquad 4.22$$

For the linear elastic case the elastic modulus of both struts are equal to each other and to the concrete elastic modulus E_c ($E_{ct}(\varepsilon_1) = E_{ct}(\varepsilon_2) = E_c$) leading to

$$\frac{\partial \varepsilon_{wy}}{\partial \gamma} = \frac{\partial \varepsilon_{oe}}{\partial \gamma} = 0 \qquad 4.23$$

Moreover, since ($\cos\gamma \cong 1$) equation (4.14) becomes

$$\frac{\mathrm{d}}{\mathrm{d}\gamma}\tau(\gamma) = \frac{E_c}{2} \cdot (\sin(2\theta))^2 \qquad 4.24$$

Comparing with the '*classic*' elastic shear modulus expression ($G = E_c/(2(1+\nu))$) an equivalent Poisson ratio can be derived

$$\nu = \frac{1}{(\sin(2\theta))^2} - 1 \qquad 4.25$$

4.4 Modelling and implementation remarks

Some comments on the behaviour of the strut-and-tie model result from the analysis of the equations of equilibrium forces and compatibility of displacements. They concern the yielding of transverse steel, the possibility of representing torsional moments and, finally, the snap-back phenomenon that may occur in the shear stress-strain response curve for low shear strains after unloading, as illustrated in Figure 4.5.

4.4.1 Yielding of transverse steel

If the stirrups do not plastify, a reduction on the ratio of transverse steel, ρ_{sw}, does not modify substantially the shear force versus displacement response curve. It increases the

stirrups strain proportionally to the decrease of ρ_{sw}, so that the transverse steel maintains more or less the same level of reaction force, and it only introduces minor changes in the diagonals strain.

In the case that the transverse steel do plastify, the response depends on the state of the diagonal under tensile strain. Substituting the force F_{c1} in the compressed strut given by equation (3.8) into equation (3.9), one can write

$$V = F_{wy} + 2 \cdot F_{c2} \cdot \sin\theta \qquad 4.26$$

in other words, if the tensile strut is completely cracked, ($F_{c2} = 0$), the structure slides and the incremental top displacement of the pier is mainly due to shear strain. Furthermore, equation (3.8) shows that, in that case, the force in the compressed strut can not increase substantially either. Therefore, the shear resisting force at the cross-section follows the steel constitutive law of the stirrups.

On the other hand, if the diagonal under tensile strain still resists to tensile forces and goes through the softening branch after peaking, the increase of the strain at the tensile diagonal implies, through equation (3.8) and equation (4.26), the decrease of the compression force in the compressed strut. Consequently, the global shear resisting force also decreases and this occurs until no residual tensile strength exists in the strut. From that point, the structure is fully cracked and responds accordingly (see Figure 4.2). This underlines the need to chose behaviour laws for the struts and ties that are smooth and integrate the whole state of the elements they represent.

4.4.2 Torsional moments

As illustrated in Figure 4.3, the torsional moment in the transverse section *S* of an element with longitudinal axis $\overline{ox}$, is given by the integral of the moment of shear forces, ($\tau_{xy} \cdot dS$) and ($\tau_{xz} \cdot dS$), in relation to $\overline{ox}$. Since the shear fibre model simulates the response of structures submitted to shear forces, it should also be able to simulate the response due to torsional moments. In this case, the description of the truss in the 3D element must take into account the existence of torsional moments, i.e., of a non-uniform distribution of shear deformations in the cross-section. Two solutions are proposed: to increase the number of shear fibres to properly simulate the distribution of shear forces

in the cross-section or to expand or shrink the transverse section of the shear fibres to make the Gauss points coincide with representative points of the structure.

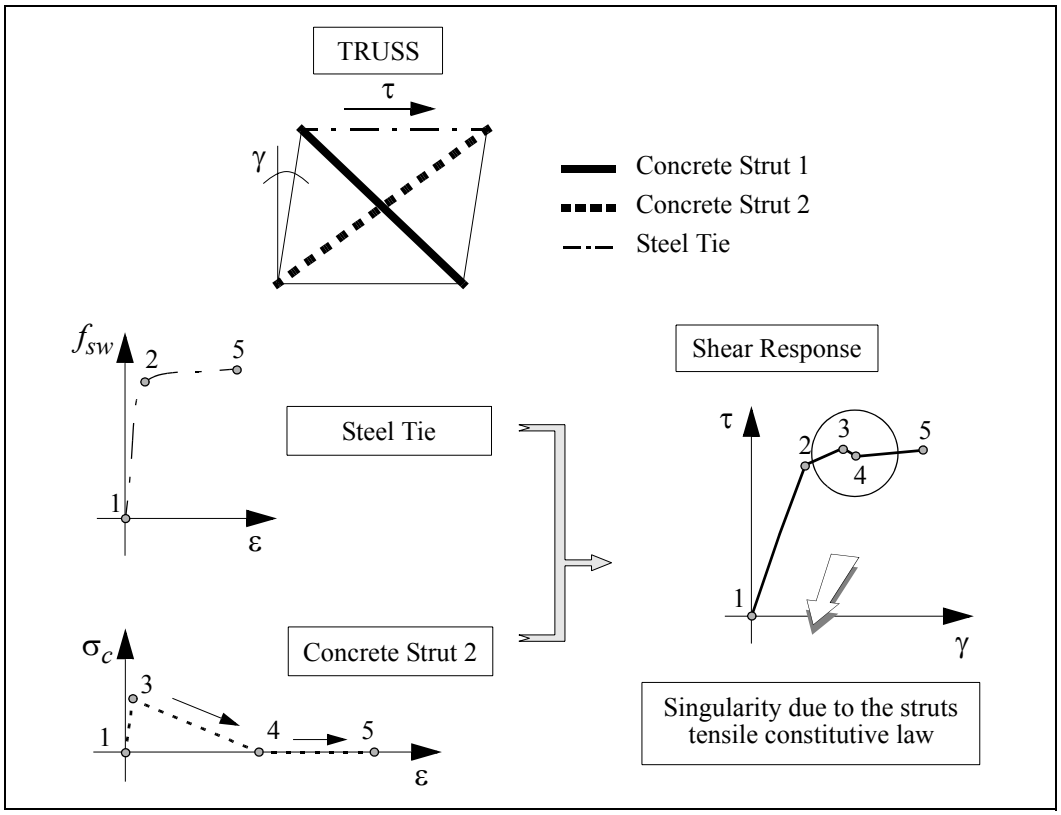

Figure 4.2 - Influence of yielding of the stirrups in the shear stress versus strain response curve

In order to explain further the meaning of these two solutions, a 3D beam element with a rectangular hollowed core section is considered. The first solution consists in describing each of the four side walls of the beam by a different shear fibre element with a transverse section proportional to the zone of the cross-section it represents. Each Gauss point of each shear fibre '*sees*' different shear strains, depending on the torsional rotation and the position it occupies in the cross-section and, therefore, it contributes differently to resist torsional moments (see Figure 4.4-a)).

The second solution is to change the cross-sectional area of the shear fibres by expanding it so that the position of each of the 2 per 2 Gauss points represents the average shear stress of each quarter of the total cross-section (see Figure 4.4-b)). A corrective factor must be used to convert the expanded area to the real transverse area. In the case of the model in CASTEM 2000, the warping parameter α, described in [17], is used. It repre-

sents the quotient between the real area and the expanded area.

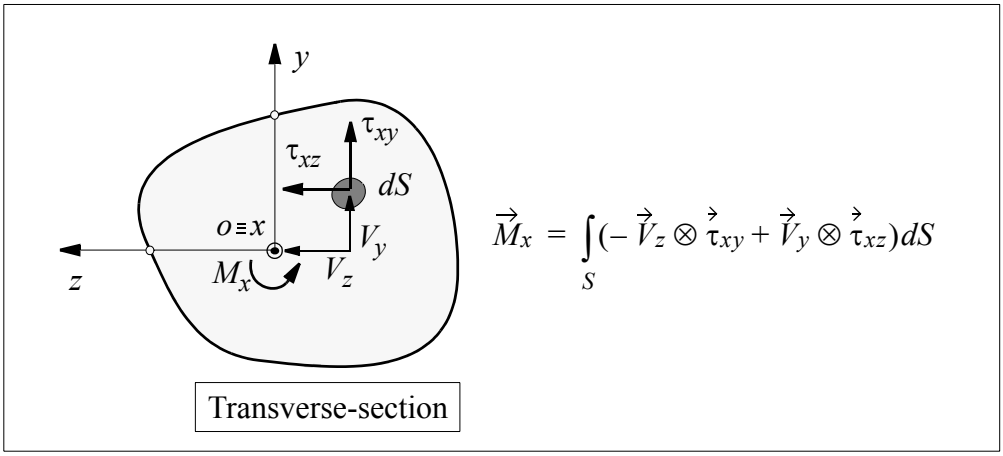

Figure 4.3 - Torsional moments

This procedure must be applied to both transverse directions; at least two shear fibres, one per each transverse direction, must be considered in the 3D element. In Figure 4.4-a) the stresses at the shear fibres are represented by one vector per fibre and not one per each Gauss point so as not to overcharge the picture.

4.4.3 The snap-back phenomenon

A snap-back phenomenon has been observed at the shear stress-strain response curve after cracking. The reason for this phenomenon is found in the equations of compatibility of displacements and equilibrium of forces of the model. The strain in the struts is the combination of three different deformations: the average axial strain ε_{oe}, the stirrups strain ε_{wy}, and the shear strain γ. During cyclic loading and after cracking of the concrete, the average axial strain grows with loading. When the structure unloads, ε_{oe} decreases to a minimum that corresponds to the pinching zone of the flexural force versus displacement curve. This is particularly evident after yielding of the longitudinal steel bars. However, while some cracks close, others open and ε_{oe} increases again till the peak displacement in the other direction is reached. Still, as growing shear forces correspond to, or should correspond to, growing shear deformations, the shear strain should increase

and decrease following the loading history.

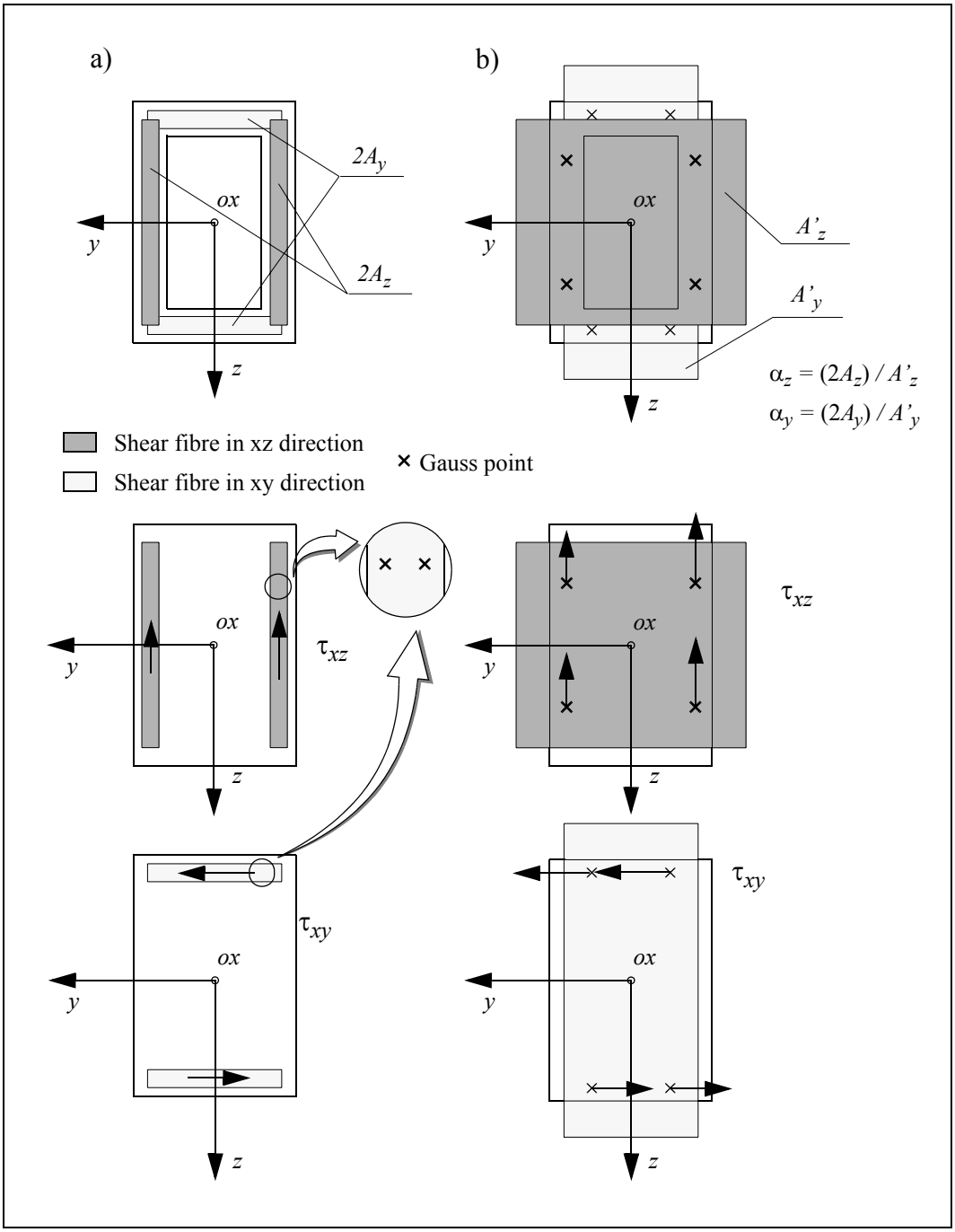

Figure 4.4 - Numerical simulation of torsional moments resisting mechanism

Thus, when the structure unloads after cracking, the absolute value of the two strains may progress in opposite directions. In fact, the shear strain changes sign before the minimum average axial strain is reached (see the example in Figure 4.5 - circle 1). After this point, while the absolute value of the shear strain increases, the average axial strain goes

on decreasing and demanding even higher shear strain in order to respect the compatibility of displacements and equilibrium of forces in the structure. This is true until the minimum average axial strain occurs. Then it increases giving, together with the shear strain, a '*positive*' contribution to the deformation of the compressed strut.

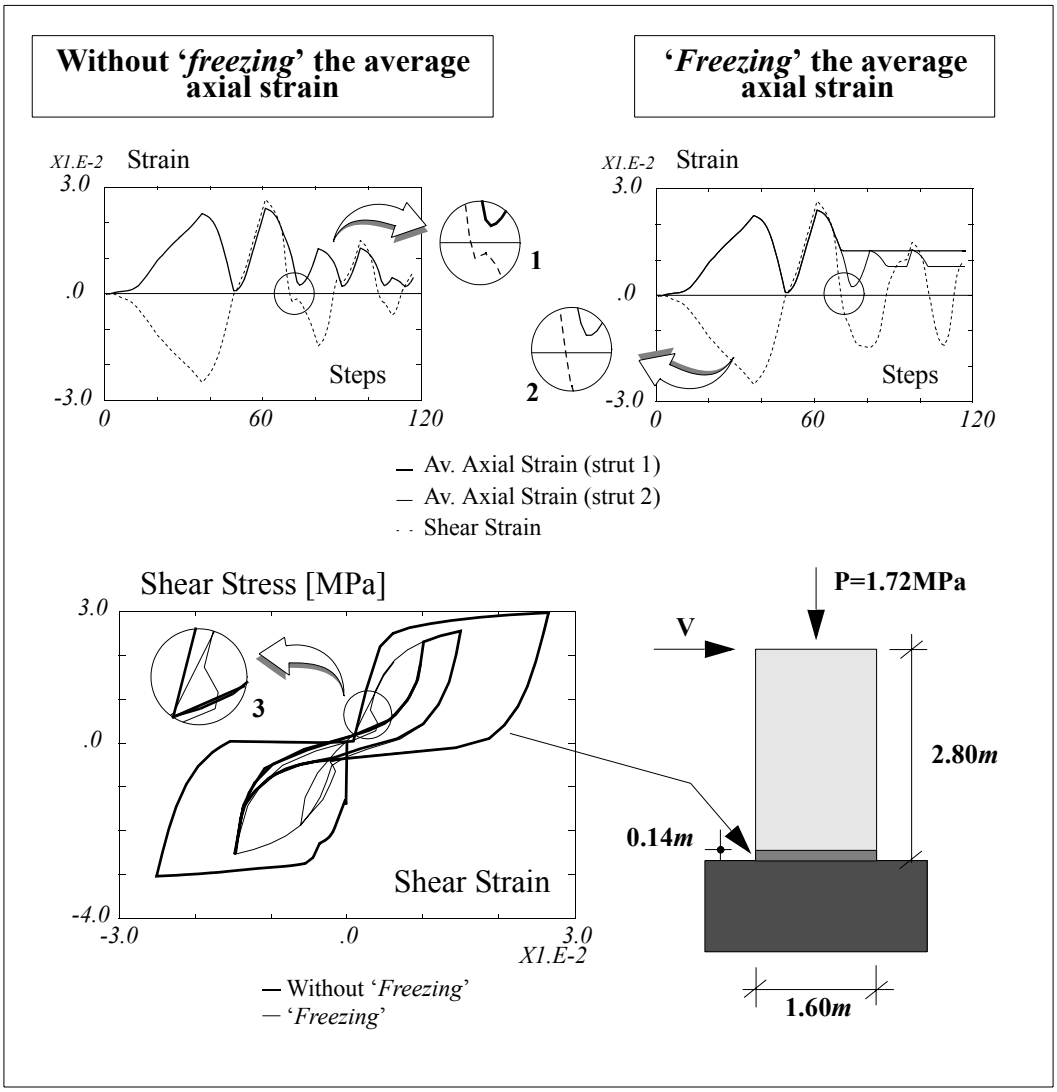

Figure 4.5 - The '*snap-back*' phenomenon

To respect the equilibrium of forces and the compatibility of deformations in the structure, the change in the growing direction of the average axial strain may force the shear strain to decrease in order to compensate for the increase of the mean axial strain that, sometimes, is quite abrupt. This gives rise to the '*snap-back*' phenomenon in the shear stress versus strain response curve, i.e., the decrease of the shear strain for an increase of the shear force, illustrated in Figure 4.5 (circles 1 and 3). The numerical simulation cor-

responds to the response of a bridge pier submitted to a cyclic static horizontal displacement at the top. The cross-section and other characteristics of the structure correspond to the bridge pier with section type 3 referred to in section 5.

To confirm this analysis a checking procedure was implemented: the value of the average axial strain due to the axial force and flexural moment was '*frozen*' each time the shear strain changed sign, i.e., each time the shear stress-strain response curve crossed the shear stress axis. This value represented the minimum axial strain allowed in the compressed strut for the following steps and it was corrected each time a higher axial strain occurred in the same circumstances (Figure 4.5 - circle 2).

For most of the examples solved with this procedure the '*snap-back*' phenomenon did not occur. In the case of piers with low axial forces, although the phenomenon was still reproduced, it was much less evident. This procedure seems to confirm the previous analysis and, at the same time, it stresses the importance of the average axial strain in the global shear response. However, other numerical analyses performed with the same structure as in Figure 4.5 show that the shear cracking angle also plays a fundamental role in this process: a higher cracking angle reduces the weight of the average axial strain in the struts strain disguising the '*snap-back*' phenomenon.

5 MODEL VALIDATION

To check the proposed non-linear shear model, a set of squat bridge piers tested at the ELSA laboratory in Ispra, Italy, have simulated numerically. These squat piers are part of a series of bridges designed under the research programme of the European Community: Pre-normative Research in Support of Eurocode 8 (PREC8) [4]. The structures, one regular bridge and three irregular bridges with the same profile, were tested following the pseudo-dynamic testing procedures and using the reaction-wall facility of the laboratory. Furthermore, a cyclic static test on an isolated squat pier with increasing top displacements was also carried out at the ELSA laboratory.

These experimental results are used in this work to validate the numerical model. Since the aim of this section is not to simulate the bridges response but to check the behaviour of the non-linear shear model, instead of applying the seismic action to the global structure, the history of displacements found during the tests is applied directly to the top of the piers. Furthermore, only the short pier of the irregular bridges is analysed (see Figure 5.1).

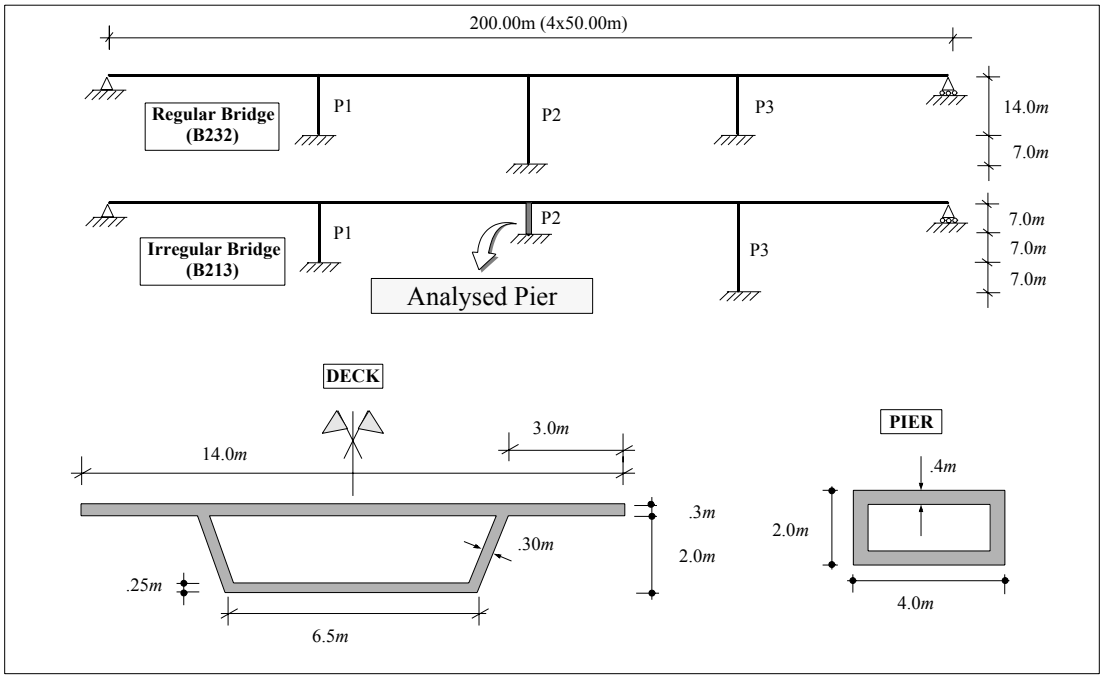

Figure 5.1 - Geometrical characteristics of bridges tested at the ELSA laboratory (scale 1:1)

Thus, after a brief description of the experimental campaign, in particular of the charac-

teristics of the structures being analysed, the numerical and experimental results of, first the isolated squat pier and then the three piers belonging to the three bridges of PREC8 programme, are presented. The response of the two models, considering non-linear and linear elastic shear behaviour, are also compared.

5.1 Experimental reference results

The research programme at the ELSA laboratory included the pseudo-dynamic testing of six bridges using substructuring techniques: a regular and 3 irregular (1:2.5) scale bridges (see Figure 5.1). One of the irregular structures was also tested with isolation/ dissipation devices and asynchronous motion. This was the first large scale testing campaign successfully performed with such a technique [4]: the piers were tested in the laboratory and the deck was simulated with a linear elastic model in the computer. A design earthquake corresponding to the Eurocode 8 [21] response spectrum for soil type B and 5% damping was applied to the bridges.

No flexural moments were transferred through the pier-deck connection points. The superstructure and the substructure moved together in the horizontal transverse direction but were disconnected in the vertical and longitudinal direction of the bridge. A vertical force of 1.72MPa is applied to the top of the piers to simulate the dead load of the deck.

Four experimental results at the squat pier are presented, corresponding to the static cyclic test on the squat pier and to the Pseudo Dynamic test on the three irregular bridges. They are referred to as P3S, P1D, P3D and P5D, where the number refers to the section type according to the nomenclature presented in [23], [4] and [22] and illustrated in Figure 5.2, and the last letter refers to the static test (S) or the PSD test (D).

The mechanical characteristics of the materials: steel (B500 Tempcore) and concrete C25/30 have been evaluated on the basis of the tests performed on the material samples and are presented in Table 5.1 and Table 5.3, respectively.

The piers in the laboratory are build in plinths rigidly attached to the strong floor. The local deformation of the plinths introduces a supplementary rotation at the bottom of the pier. This effect is taken into account in the numerical tests through a flexible foundation

represented by a linear elastic rotational spring calibrated for the experimental tests [22].

Table 5.1: Steel mechanical properties (average values)

Bar Diam. [mm]	Average Bar Diam. [mm]	Number of Tests	σ_y [MPa]	σ_u [MPa]	ε_u [%]	σ_u/σ_y
ϕ5	4.7	7	700	731	1.6	1.05
ϕ6	6.4	6	364	430	15.1	1.18
ϕ8	8.2	4	503	563	12.3	1.12
ϕ10	10.0	4	489	572	14.5	1.17
ϕ12	11.9	4	558	647	12.8	1.16
ϕ14	13.8	4	477	578	13.0	1.21

Table 5.2: Concrete cubic compressive strength (average values)

	Pier Type			
	P3S	**P1D**	**P3D**	**P5D**
Strength [MPa]	35.4	41.2	37.0	40.2

Only the irregular bridge, and in particular the shortest pier illustrated in Figure 5.1, is referred to in the report. Three different doubly symmetric cross-sections with different volumetric ratios of longitudinal and transverse steel bars are considered (see Figure 5.2 and Table 5.3), where the number of the type of section follows the nomenclature pre-

Table 5.3: Longitudinal and transverse reinforcement in the piers cross-section

	Section Type		
	S1	**S3**	**S5**
Volumetric ratio of longitudinal rebars, $(\rho_l)^a$ [%]	0.50	0.92	1.69
Mechanical volume ratio of confining hoops, $(\omega_{wd})^b$ [%]	24.7	20.5	35.5

a. $\rho_l = \dfrac{Volume\ of\ longitudinal\ bars}{Volume\ of\ concrete}$

b. $\omega_\omega = \dfrac{Volume\ of\ confining\ hoops}{Volume\ of\ concrete\ core} \cdot \dfrac{f_{\omega y}}{f_c}$ and $(f_{\omega y} = 500MPa)$, $(\sigma_c = 30MPa)$

sented in [4], [22] and [23]. During the experiments the piers were fitted with displacement transducers distributed along the sides of the columns. The squat pier has been especially well fitted to enable the splitting of bending and shear displacements [4]. The

displacements due to bending forces were computed through a quadratic integration of the rotations measured along the length of the column (see Figure 5.3). The difference between the total displacements observed during the experiment and the bending displacements gives the deformation due to shear forces. Note that with this approach, displacements like those due to the deformation of the basement appear in the shear curves.

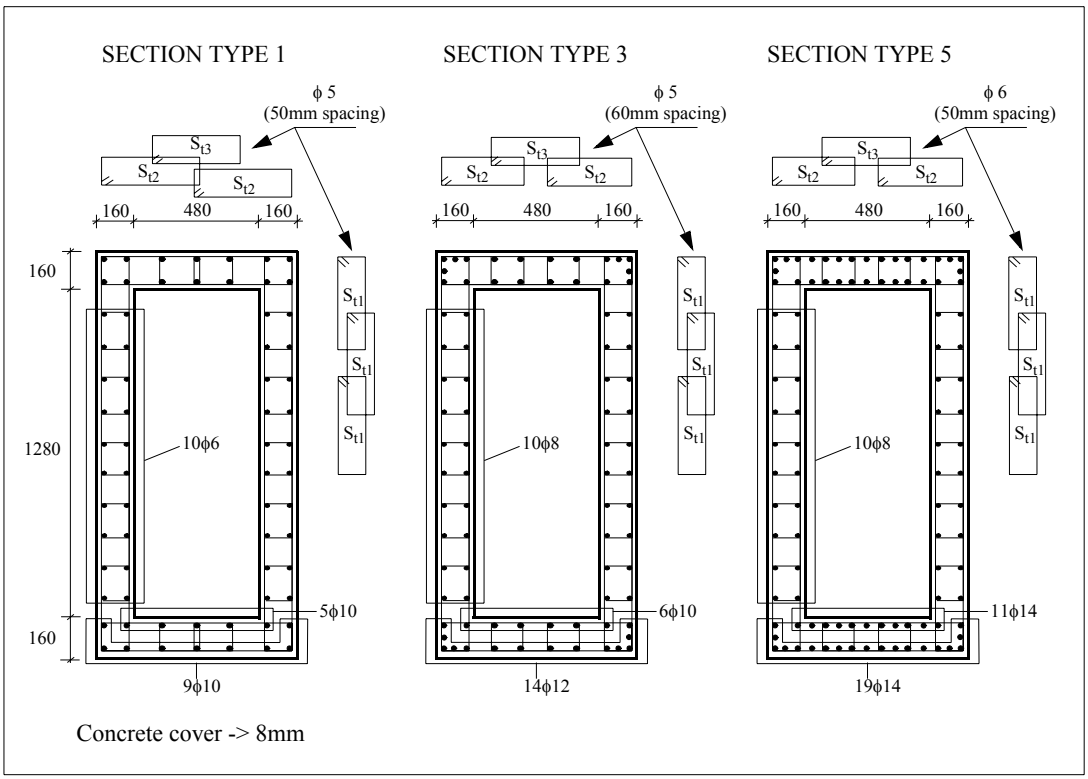

Figure 5.2 - Reinforcement layout (all the measurements and diameters are in [mm])

Four experimental results at the squat pier are presented, corresponding to the static cyclic test on the squat pier and to the Pseudo Dynamic test on the three irregular bridges. They are referred to as P3S, P1D, P3D and P5D, where the number refers to the section type according to the nomenclature presented in [23], [4] and [22] and illustrated in Figure 5.2, and the last letter refers to the static test (S) or the PSD test (D).

5.2 Numerical applications

The three different cross-sections are made of bending and shear fibres. Since the applied load introduces transverse forces only in one direction of the pier and, furthermore, no torsional moments exist, a '`I`' type cross-section was adopted. The distribution of con-

fined and unconfined concrete and steel fibres in the cross-section is illustrated in Figure 5.6. The parameters of the model defining both the steel and the concrete characteristics are presented in Figure 5.4 and Figure 5.5. The piers were divided in 5 plus 2 Timoshenko elements with lengths of 0.34*m* and 0.55*m*, respectively.

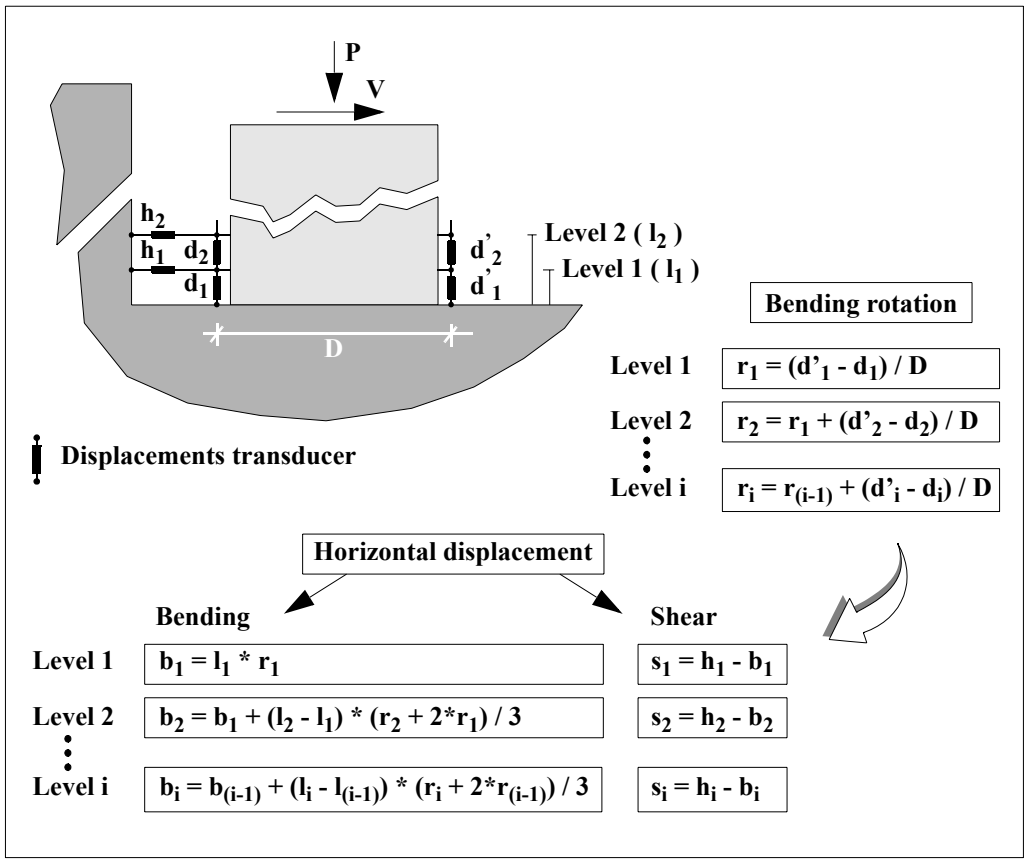

Figure 5.3 - Splitting of shear and bending displacements

5.2.1 Model parameters

The expression used to describe the confinement of the concrete core is the one specified in Eurocode 8 [21]. According to this reference code, the increase in the compression strength and corresponding strain due to confinement effect depends on the cross-section characteristics, in particular on the transverse steel ratio and spacing. Furthermore, the four parameters presented in equation (3.16) and equation (3.18) which define the loading and unloading laws of the hysteretic concrete constitutive law, are ($F_1 = 2.0$), ($F_2 = 0.75$) and ($F_1' = 20.0$) and ($F_2' = 20.0$) for the longitudinal fibres and ($F_1' = 20.0$) and ($F_2' = 3.0$) for the shear fibres.

The parameters adopted in the Menegotto-Pinto model are ($R_o = 10.0$), ($a_1 = 9.0$) and ($a_2 = 0.15$). The properties of the steel are illustrated in Figure 5.5.

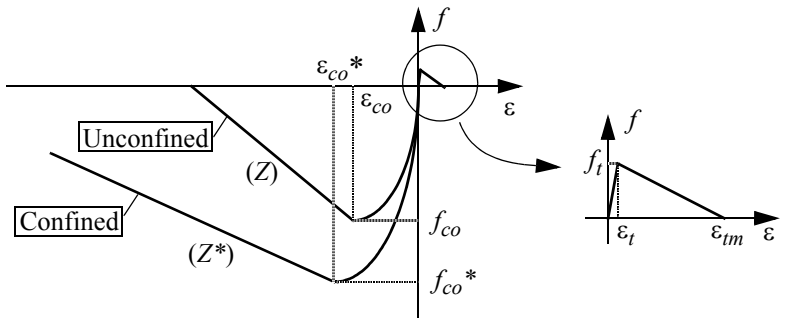

Piers	f_{co} [MPa]	f_{co}*[MPa]	ε_{co} [%]	ε_{co}*[%]	Z	Z*	f_t [MPa]	[a] $\varepsilon_{tm}/\varepsilon_t$	[b] $\varepsilon_{tm}/\varepsilon_t$
S1	36.2	45.6	0.25	0.40	100	27.7	1.6	10	100
S3	32.0	40.2	0.25	0.39	100	28.3	1.2	7	100
S5	35.2	43.3	0.25	0.38	100	30.3	0.1	5	100

a. Longitudinal fibres

b. Shear fibres

Figure 5.4 - Confined and unconfined concrete characteristics

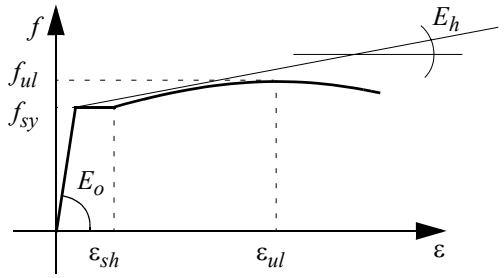

Piers		f_{sy} [MPa]	f_{ul} [MPa]	ε_{sh}*[%]	ε_{ul} [%]	E_o [GPa]	E_h/E_o[%]
S1	**Long. Fibres**	490.0	570.0	2.00	14.5	206.0	0.55
	Shear Fibres	700.0	730.0	0.34	1.6		
S3	**Long. Fibres**	540.0	630.0	2.00	13.2	206.0	0.55
	Shear Fibres	700.0	730.0	0.34	1.6		
S5	**Long. Fibres**	480.0	580.0	2.0	13.0	206.0	0.55
	Shear Fibres	365.0	430.0	2.0	15.0		

Figure 5.5 - Longitudinal and transverse steel characteristics

Note that if shear stresses exist in the cross-section and are important, cracking of concrete occurs along a surface oblique to the longitudinal fibres. This means that the physical structure opens cracks before the longitudinal fibres reach the tensile strength of the

concrete, in other words, the tensile strength in the model should not be the value from the axial test, or any equivalent test like the Brazilian test, but a lower value. Thus, and in order to adequately represent the pre-yielding branches of the global force-displacement curve, the tensile strength adopted in the concrete presented in Figure 5.4 is the value that fits the envelope of the top force-displacement experimental curve.

As for the transverse steel ratio, it is given by

$$\rho_{sw} = \frac{4 \cdot A_{sw} \cdot r}{b_w \cdot s} \qquad 5.1$$

where ($b_w = 0.32m$) and r measures the superposition of the stirrups, i.e., the ratio between the total length of the stirrups and the length of the cross-section, ($r = (6 \cdot 0.492m)/(1.60m)$), s is the stirrups spacing and A_{sw} is the area of the stirrups cross-section. The values in equation (5.1) for the three different sections are presented in Table 5.4.

Table 5.4: Transverse steel ratio

Pier	A_{sw} [m^2]	s [m]	ρ_{sw} [%]
S1 (5)[a]	1.963x10^{-5}	0.050	0.905
S3 (5)	1.963x10^{-5}	0.060	0.754
S5 (6)	2.827x10^{-5}	0.050	1.304

a. Stirrups diameter in [mm]

5.2.2 Fibre discretization

To describe the flexibility of the plinth at the basement of the pier, a linear elastic rotational spring is placed at the bottom of the pier. It is simulated through a fictitious $0.01m$ length element (1:2.5 scale) with the same cross-section of the pier and a Young modulus of $0.2GPa$. The distribution of the longitudinal and shear fibres in the pier cross-section is illustrated in Figure 5.6.

The transverse section of the shear fibre considers that only the side-walls of the pier contribute to shear strength, and it includes the unconfined concrete. Thus, the shear

fibres measure 0.32*m* per 1.44*m*.

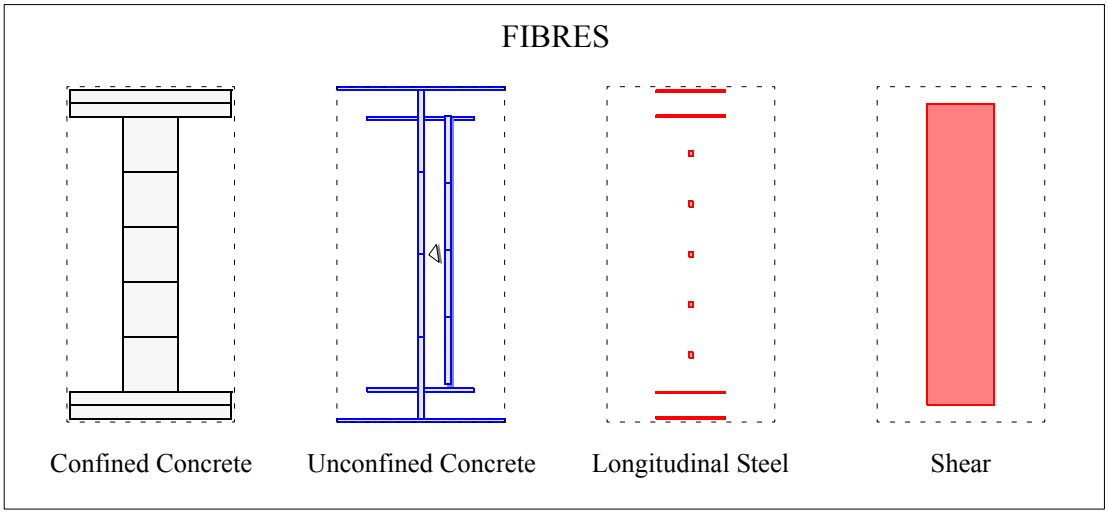

Figure 5.6 - Distribution of the fibres in the cross-section (bending + shear)

5.2.3 Struts inclination angle

The critical cracking angle is calculated using the model described n section 3.2.5 and referred to as '*cracking limit analysis*'. Again, only the side walls of the pier were considered to contribute to shear strength. The values required to compute the angle θ for the three different cross-sections are presented in Table 5.4 and Table 5.5.

Table 5.5: Critical cracking angle θ

Pier	f_{sw} [MPa]	$^{a}\rho_s$ [%]	$^{b}f_{sy}$ [MPa]	f_c [MPa]	$^{c}\tau_u$ [MPa]	$^{d}\tau_u$ [MPa]	$^{e}\tau_u$ [MPa]	f_θ [degrees]
S1	700	0.276	364	41.2	2.52	14.86	20.6	68.3
S3	700	0.491	503	37.0	3.61	12.94	18.5	55.6
S5	364	0.491	503	42.2	3.42	13.33	21.1	54.2

a. $\rho_s = (10 \cdot \pi \cdot D^2)/(1.28m \cdot 0.32m)$, being $D = 6mm$ in S1 and $D = 8mm$ in S3 and S8.
b. It refers only to the steel in the side walls of the structure
c. $\tau_u = \sqrt{\rho_{sw} \cdot \rho_s \cdot f_{sy} \cdot f_{sw}}$
d. $\tau_u = \sqrt{(f_{cd} - \rho_{sw} \cdot f_{sw})\rho_{sw} \cdot f_{yw}}$
e. $\tau_u = f_{cd}/2$
f. $\theta = \text{atan}[\sqrt{(\rho_{sw} \cdot f_{sw})/(\rho_s \cdot f_{sy})}]$

For the '*cracking equilibrium model*', the results for the three different cross-sections are presented in Figure 5.7. The curves illustrated by broken lines represent the limits for the cracking angle given by equation (3.38). The angle to be used in the non-linear shear model is the lowest value that corresponds to yielding of the longitudinal steel or to

yielding of the transverse steel. The yielding point is indicated in the graphics by a vertical broken line and the corresponding cracking angles are presented in Table 5.6.

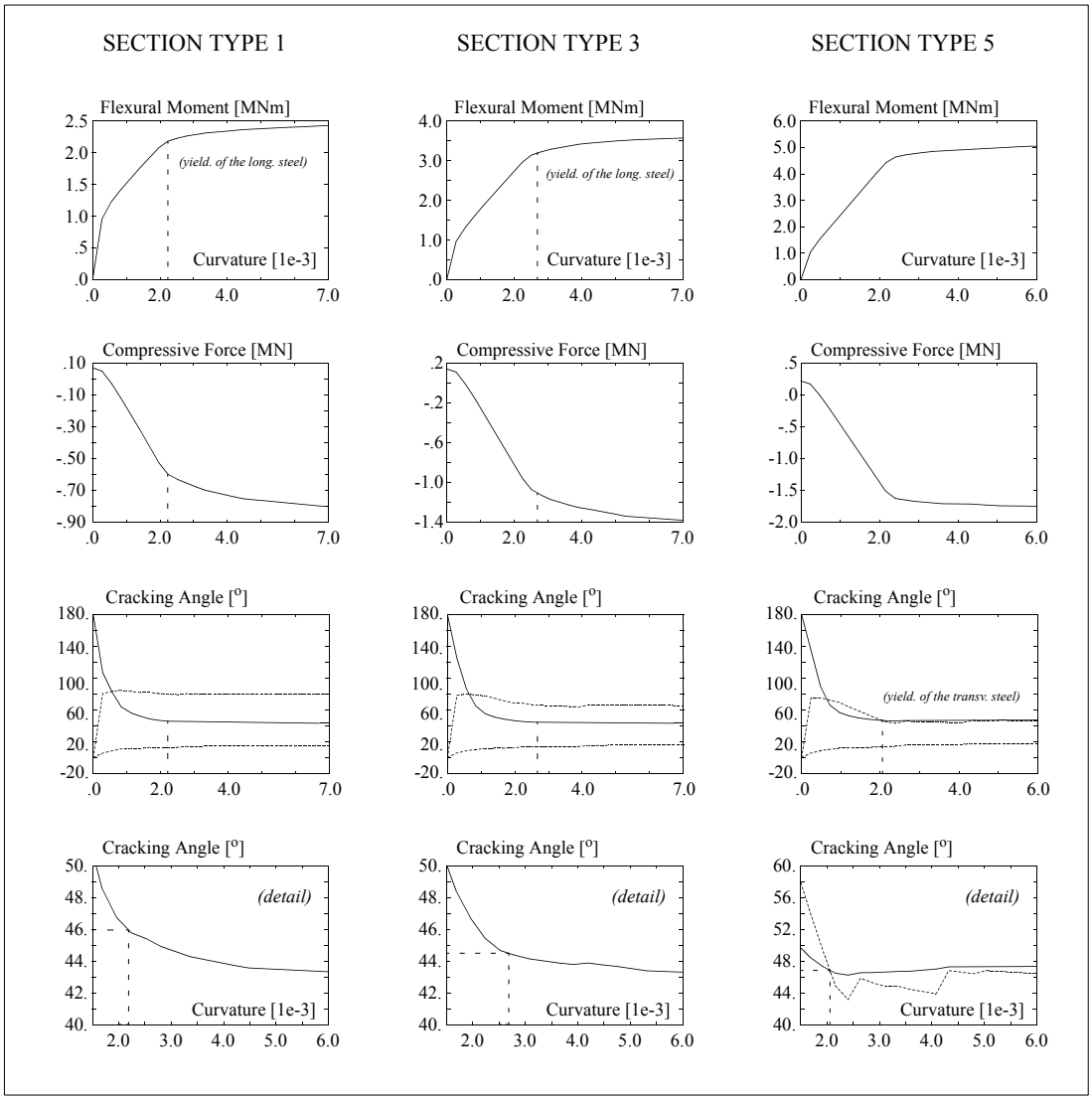

Figure 5.7 - Cracking angle using the '*cracking equilibrium model*'

The angles considered in these two methods are quite different one from the other; the results from the '*cracking equilibrium model*' agree quite well with the experimental values whereas the shear angles using the '*cracking limit analysis*' are far from the experimental angles observed in the piers at the laboratory (around 45^o for the three piers: P1, P3 and P5).

Table 5.6: Cracking angle

Section type 1	Section type 3	Section type 5
46.0º	44.5º	46.8º

Since the angles computed through the '*cracking equilibrium model*' are close to 45^{o}, this value was adopted for the three piers. However, the angles referred to in Table 5.5 are also considered in the numerical calculations presented in the report.

6 RESULTS

The numerical response of the piers is calculated using the fibre model and the two different approaches for the shear forces: the linear elastic law and the non-linear shear model described in the report. The histories of displacement registered at the top of the four piers during the cyclic static and the Pseudo-Dynamic tests are applied to the top of the numerical structures (see Figure 9.1).

For each test the following response curves are presented: transverse force versus total transverse displacement at the top of the pier and at a height of 1.70*m*, transverse force versus shear and flexural transverse displacements at a height of 1.70*m* and, finally, the peak displacement profiles for both loading directions. For pier P5S, apart from the two analytical cracking angles two other angles are adopted: ($\theta = 48°$) and ($\theta = 51°$). Still for pier P5D and for cracking angle ($\theta = 45°$), two additional transverse steel ratios are considered: ($\rho_{sw} = 0.0115$) and ($\rho_{sw} = 0.0100$).

After an overview of the main outcomes of the model, the analytical results are compared with the experimental response obtained at the ELSA laboratory. A more detailed analysis pier by pier is made before the final conclusions are drawn.

6.1 General results

Although the piers have the same concrete cross-section and the same shear span ratio, ($r_{sp} = 2.8/1.6$), the influence of shear forces in the response is quite different from one pier to the other. As the strength to flexural moments increases with the longitudinal steel ratio and higher flexural strength means higher allowable transverse force at the top of the pier, a stronger participation of shear mechanisms in the response is expected when the longitudinal steel ratio increases. This is confirmed by the diagrams in Figure 9.18: the proportion of shear displacement increases from section type 1 to section type 5.

Furthermore, the presence of transverse forces changes the orientation of the principal directions that become diagonal to the longitudinal axis of the structure and, in this case, the transverse steel has a very important role in resisting shear forces; the longitudinal and transverse steel form a steel grid that, together with the concrete, define a truss

mechanism that controls the deformation of the structure. Therefore, the resistance to shear forces depends strongly on the amount of transverse steel in the pier. An example using pier P5D for different transverse steel ratios is illustrated in Figure 9.20.

Note that the non-linear shear model uses the average axial deformation that comes from the flexural model which, in turn, depends on the dimension of the elements defining the structure. Thus, in order to verify the dependency of the response to the mesh discretization, four tests were done on pier P5 considering elements with different lengths near the basement: 2 elements of 0.85m in the first test, 3 elements of 0.56m in the second test, 5 elements of 0.34m in the third test and 4 elements of 0.17m plus 3 elements of 0.34m in the last test. A cyclic displacement history was applied to the top of the pier: a 2cm amplitude cycle followed by a 4cm cycle. The results presented in Figure 9.21 show that the four responses agree quite well with each other. Even the case where only two 0.85m length elements are considered near the basement gives a response close to the more refined solution.

6.1.1 Low strength pier - P1

Pier P1 is the least reinforced of the three piers. The first comment is that in spite of the general good agreement between the numerical and the experimental results, the ultimate state of the pier was not caught by the numerical model. The decrease of strength registered in the experimental force versus displacement curve is due to the rupture of the longitudinal steel bars which did not occur in the numerical test. After this loading step the comparison between the experimental and the analytical results makes no sense.

The simulation of the ultimate state of a structure caused by an abrupt event like the rupture of a steel bar is a very a difficult subject. Small variations in the geometry and/or on the materials can explain the differences to the experimental results. In the case of a symmetrical cross-section with uniaxial bending, such as the one under analysis, one bar can not break alone leaving all the others at the same level still resisting, unless different fibres with different materials characteristics, which would have to be known extremely accurately, were considered for each one of the rebars. Furthermore, the degradation of the characteristics of the materials with cyclic loading would have also to be properly taken into account.

From the comparison of the results using the linear and the non-linear shear behaviour model in Figure 9.2 to Figure 9.5 and in Figure 9.22 and Figure 9.23, it seems that no evident benefit comes from the non-linear shear model. The shear displacements ratio is very low and the stiffness of the structure is not strongly affected by the degradation of shear stiffness. Nevertheless, and in spite of the large over-estimation of the shear displacements, the force-displacement curves at a height of 1.70*m* for the non-linear shear model are closer to the experimental results. The over-estimation of the numerical shear displacements is partly due to a more flexible response at the post-cracking branch before yielding of the longitudinal bars. Although this is true for both cracking angles, ($\theta = 68°$) and ($\theta = 45°$), the first angle gives a behaviour in shear closer to the experimental response. Nevertheless, the global force-displacement curves for both angles, experimental and analytical, are similar and very close to the experimental response.

Before going further into the analysis of the results, two comments must be made. Firstly, the split of total displacements in flexural and shear displacements is fully legitimate only when dealing with numerical results; in a real structure there is a perfect coupling between the two displacements. Secondly, since in the numerical model the flexural behaviour assumes that cracking is perpendicular to the longitudinal axis of the structure, the diagonal cracking on the physical structure changes the conditions that make the splitting fully comparable with the numerical results. Therefore, the first comparison between the analytical and the experimental results should be done at the level of the global force versus displacement curves and only after the flexural and the shear behaviour should be analysed separately. Regardless, the splitting of the total experimental displacements gives a good idea of how much the behaviour of the structure is influenced by shear forces and, furthermore, how far the numerical model is to predict non-linear shear behaviour.

The profiles of maximum displacements are closer to the experimental results when the angle from the '*cracking limit analysis*' is used (see Figure 9.18 and Figure 9.30). In this case, and in spite of the more flexible behaviour of the model near the basement in relation to the experiment, the two results are quite close.

6.1.2 Medium strength pier - P3

Pier P3 was tested for two different top displacement-time histories. The first one corresponds to the displacement measured during the Pseudo-Dynamic test of bridge B213A according to [4]. The second is a displacement-time history for growing peak displacements as it is described in [23] and illustrated in Figure 9.1.

The global force versus displacement curves for both assumed cracking angles follow quite well the experimental results; although the analytical angle ($\theta = 56°$) gives a less dissipative shear curve, the test with the angle ($\theta = 45°$) shows a shear force versus displacement curve which is closer to the results found in the laboratory (see Figure 9.6 to Figure 9.13 and Figure 9.24 to Figure 9.27). For this particular pier, the '*snap-back*' phenomenon is also clear. This is especially evident for ($\theta = 45°$), since in this case the participation of the average axial deformation in the non-linear shear model is more important (see equation (3.6)). This happens for both displacement-time histories. Regarding the flexural behaviour, the fibre model describes the response due to flexural moments with great accuracy.

Since a higher longitudinal steel ratio enables greater shear forces on the structure, pier P3 shows a behaviour which is clearly more influenced by shear forces than pier P1. This is evident in the shape of the global response curve. For the same displacement imposed at the top of the pier, the results using the linear shear model are more dissipative showing a typical flexural behaviour. This model does not reproduce properly the narrowing and lengthening of the hysteretic force-displacement curve typical of structures submitted to important transverse forces.

The profiles of maximum displacements show that the pier in the test considering the '*cracking limit analysis*' angle is less flexible near the basement giving better results (see Figure 9.18 and Figure 9.30). Nevertheless, the non-linear shear model considering both angles represents well the results from the experiments.

6.1.3 High strength pier - P5

From the three piers analysed in the report, P5 is the pier with the higher longitudinal and transverse reinforcement ratio. The analytical results using both cracking angles are dis-

cussed before; any comparison with the experimental response is done. Looking at Figure 9.14 and Figure 9.15, the first comment is that the analytical angle, ($\theta = 54°$), gives a very flexible response mainly controlled by the shear (truss) mechanism. When the maximum shear strength of the truss is reached, i.e., the transverse steel bars yield, the structure cannot respond to the new demand of shear force and it slides near the basement. Thus, the maximum flexural moment is controlled by the truss mechanism and the contribution of the flexural mechanism to the global behaviour of the structure is reduced significantly.

The second comment comes from Figure 9.19. In the case of pier P5, the analytical results are quite sensitive to the cracking angle adopted in the strut-and-tie model. A decrease of 3^{o} in the value of the cracking angle corresponds to a decrease of more than 30% in the shear displacement.

Two circumstances contribute to the high sensitivity of the analytical results to small variations of the cracking angle at pier P5: the low yielding stress of the transverse rebars, 365.0*MPa*, and the proximity between the maximum shear force from the truss and the flexural mechanism. In this case, a small decrease of the cracking angle corresponds to an increase of the amount of transverse steel involved in the internal equilibrium of the structure (see equation (3.7)), in other words, to an increase of the strength of the truss, enough to allow the flexural mechanism to go much further in the inelastic range. This is well illustrated in the comparison of Figure 9.14 and Figure 9.15 with Figure 9.28 and Figure 9.29.

The comparison with the experimental results shows clearly that the '*cracking limit analysis*' angle does not properly represent what happens in the physical pier. Furthermore, the analytical response for the '*cracking equilibrium model*' angle is quite close to the experimental results. These results are confirmed by the profiles of maximum displacements illustrated in Figure 9.18 and Figure 9.30. This shows that the expressions given by the '*cracking limit analysis*' are not only unsuitable to represent the cracking pattern observed in the experiments but should also not be used to compute the cracking angle of the non-linear shear model.

Finally, the model was able to represent the non symmetrical behaviour in shear due to yielding of transverse steel bars; although two struts are considered to represent the state of the concrete for both loading directions, the stirrups are the same regardless of the loading direction. Thus, if after loading the structure in one direction the stirrups yield, the plastic deformation at the steel bars is transmitted when the load goes in the opposite direction. This phenomenon is not so evident in the flexural behaviour since the longitudinal rebars under tensile forces change when the structure is loaded in different directions.

When compared with the response using the linear elastic model in shear (see Figure 9.16 and Figure 9.17), a much more dissipative global force versus displacement curve is found in opposition to the experimental results.

7 CONCLUSIONS

The results expressed in Figure 9.22 to Figure 9.29, show, in general, a very good agreement between the numerical and the experimental results. The comparison is made at two levels: at the top and at 1.70*m* from the bottom of the pier. The numerical transverse force versus displacement curves at both levels fit the experimental results. The behaviour of structures where the effect of shear forces in the response is not negligible is well reproduced by the non-linear shear model; the narrowing and lengthening of the force versus displacement curves observed in the experimental results due to the shear forces is well represented.

In a strut-and-tie based model like the one described in this report, the determination of the angle of the cracking pattern is very important. Special care must be taken when dealing with structures where the applied transverse force is near to its maximum shear capacity. In this case, small variations of the shear cracking angle can greatly change the response.

Furthermore, the numerical tests presented in the report show that the analytical model referred to as '*cracking limit analysis*' to estimate the critical cracking angle is not suitable to represent what happens in the structure. Angles much higher than the experimental values were computed with this formulation and gave results that for the critical pier P5 were quite far from the experimental results. Instead, the '*cracking equilibrium model*' developed in section 3.2.5 gave, for the three piers, cracking angles in very good agreement with the values observed during the experiments.

The tests done on pier P5 also show that the results can be considered mesh independent. Four different meshes, more or less refined near the basement, gave similar top transverse force versus displacement response curves.

8 REFERENCES

[1] Buckle, I. G. 1991. "Seismic Design and Retrofitting of Reinforced Concrete Bridges". Proceedings of the International Workshop held in Bormio on April 2-5. Edited by G. M. Calvi and M. J. Priestley. Bormio, Italy

[2] Stojadinovic, B. & C. Thewalt 1995. "Upgrading Bridge Outrigger Knee Joint Systems". Report No. UCB/EERC - 95/03, Earthquake Engineering Research Center, University of California at Berkeley, Berkeley, USA

[3] CEA 1990. *CASTEM 2000, Guide d'utilisation*. CEA, Saclay, France

[4] Pinto, A.V., G. Verzeletti, P. Pegon, G. Magonette, P. Negro & J. Guedes 1996. "Pseudo-Dynamic Testing of Large-Scale R/C Bridges". *Report EUR 16378 EN*, Safety Technology Institute, European Commission, Joint Research Centre, Ispra Establishment, Ispra (VA), Italy

[5] Li, Xinrong 1995. "Reinforced Concrete Columns Under Seismic Lateral Force and Varying Axial Load". PhD Thesis at the University of Canterbury, Christchurch, New Zealand

[6] Park, P. & T. Paulay 1975. "Reinforce concrete structures". A Wiley Interscience Publication, John Wiley & Sons, Inc.

[7] Comité Euro-International du Béton (C.E.B.) 1983. "Response of R.C. Critical Regions Under Large Amplitude Reversed Actions". Bulletin d'Information N^{o} 161 (Contribution à la 23eme Session Plénière du C.E.B.), Prague, Czechoslovakia

[8] Paulay, T. & M. Priestley 1992. "Seismic Design of Reinforced Concrete and Masonry Buildings". A Wiley Interscience Publication, John Wiley & Sons, Inc.

[9] Fardis, M. & O. Buyukozturk 1979. "Shear Transfer Model for Reinforced Concrete". ASCE Journal of Engineering Mechanics Division, Vol. 105, No EM2, pp. 255-275, April

[10] Jimenez, R., R. White & P. Gergely 1982. "Cyclic Shear and Dowel Action Models Reinforced Concrete". ASCE Journal of Structural Engineering Division, Vol. 108, No ST5, pp. 1106-1123, May

[11] Chang, G.A. & J.B. Mander 1994. "Seismic Energy Based Damage Analysis of Bridge Columns - Part I - Evaluation of Seismic Capacity". *Technical Report NCEER-94-0006 (March 14, 1994)*. State University of New York at Buffalo, Department of Civil Engineering, Buffalo, New York, USA

[12] Priestley, M., F. Seible, R. Verma & Y. Xiao 1993. "Seismic Shear Strength of Reinforced Concrete Columns". Report SSRP-93/06, Departement of Applied Mechanics and Engineering Science, University of California, San Diego, USA

[13] CEC 1984. Eurocode No 2 - Regles Unifiees Communes pour les Constructions en Beton. EUR8848 DE, EN, FR

[14] Vecchio, F. & M. Collins 1986. "The Modified Compression-Field Theory for Reinforced Concrete Elements Subjected to Shear". ACI Structural Journal, pp 219-231, March-April

[15] Garstka, B., W.B. Kratzig & F. Stangenberg 1993. “Damage Assessment in Cyclically Reinforced Concrete Members”. Proceedings of the second European Conference on Structural Dynamics: EURODYN’93, 21-23 June, Trondheim, Norway

[16] Petrangeli, M. & P. E. Pinto 1995. “A Fibre Model for Elements Under Cyclic Bending and Shear”. Proceedings of the first Japan-Italy workshop on seismic design of bridges. ISSN 0386-5878 Technical Memorandum of PWRI N. 3369, Tsukuba, Japan

[17] Guedes, J., P. Pegon & A.V. Pinto 1994. “A Fibre/Timoshenko Beam Element in CASTEM 2000”. *Special Publication* Nr. I.94.31, Applied Mechanics Unit, Safety Technology Institute, European Commission, Joint Research Centre, Ispra Establishment, Ispra (VA), Italy

[18] Combescure, D., P. Pegon 1994. “A Fibre Model Accounting for Transverse Shear in CASTEM 2000”. *Special Publication* Nr. I.94.59, Applied Mechanics Unit, Safety Technology Institute, European Commission, Joint Research Centre, Ispra Establishment, Ispra (VA), Italy

[19] Menegotto, M. & P. Pinto 1973. “Method of Analysis for Cyclically Loaded Reinforced Concrete Plane Frames Including Changes in Geometry and Non-elastic Behaviour of Elements under Combined Normal Force and Bending”. *IABSE Symposium on Resistance and Ultimate Deformability of Structures Acted On by Well-Defined Repeated Loads*, Final Report, Lisbon, Portugal

[20] Marti, P. & Joost Meyboom 1992. “Response of Prestressed Concrete Elements to In-plane Shear Forces”. ACI Structural Journal, Vol. 89, No. 5, pp. 503-514, September-October

[21] CEC 1993. Eurocode No 8 - Structures in Seismic Regions - Design, Part 2 - Bridges (Draft-April 1993). CEN, DOC, TC250/SC8/N76

[22] Guedes, J. & A. Pinto 1996. “Numerical Simulation of the ELSA PSD Tests of R/C Bridges”. *Report EUR 16358 EN*, Safety Technology Institute, European Commission, Joint Research Centre, Ispra Establishment, Ispra (VA), Italy

[23] Pinto, A.V., G. Verzeletti, P. Negro & J. Guedes 1995. “Cyclic testing of a Squat Bridge-Pier”. *Report EUR 16247 EN*, Safety Technology Institute, European Commission, Joint Research Centre, Ispra Establishment, Ispra (VA), Italy

9 FIGURES

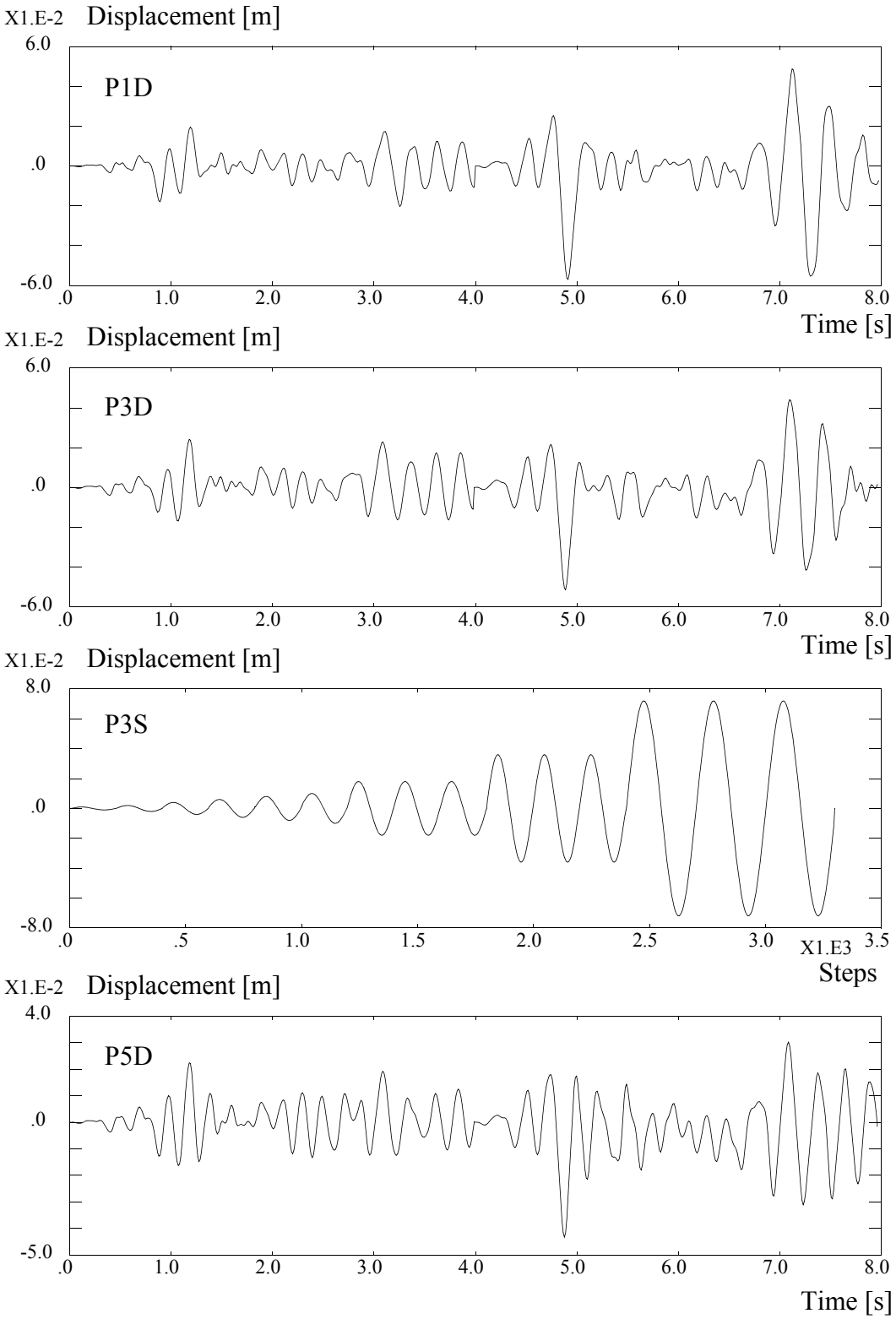

Figure 9.1 - History of displacements imposed at the top of the piers

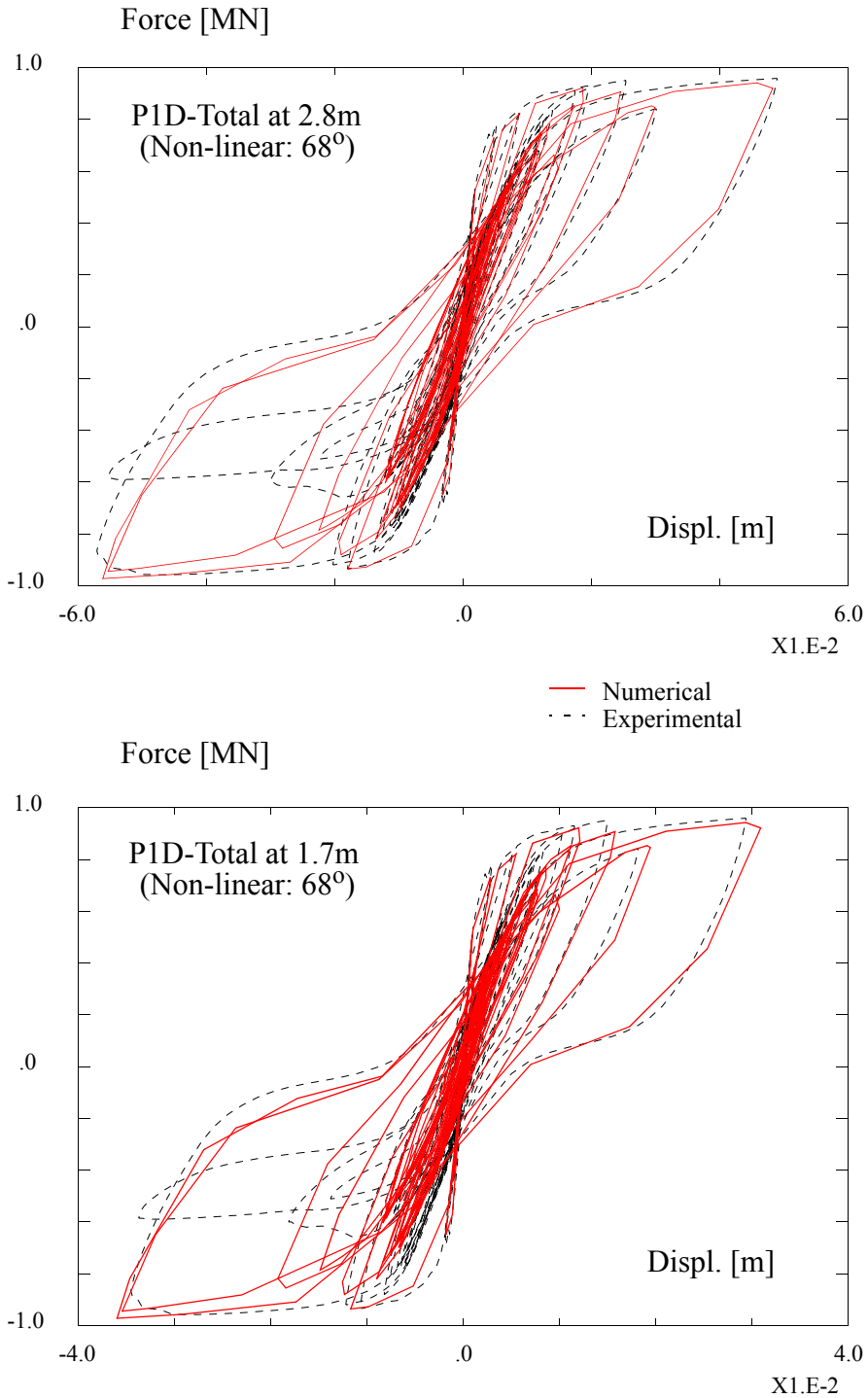

Figure 9.2 - Numerical versus experimental force-total displacement response curves for pier P1D at two different height levels and using the non-linear shear model with θ=68°

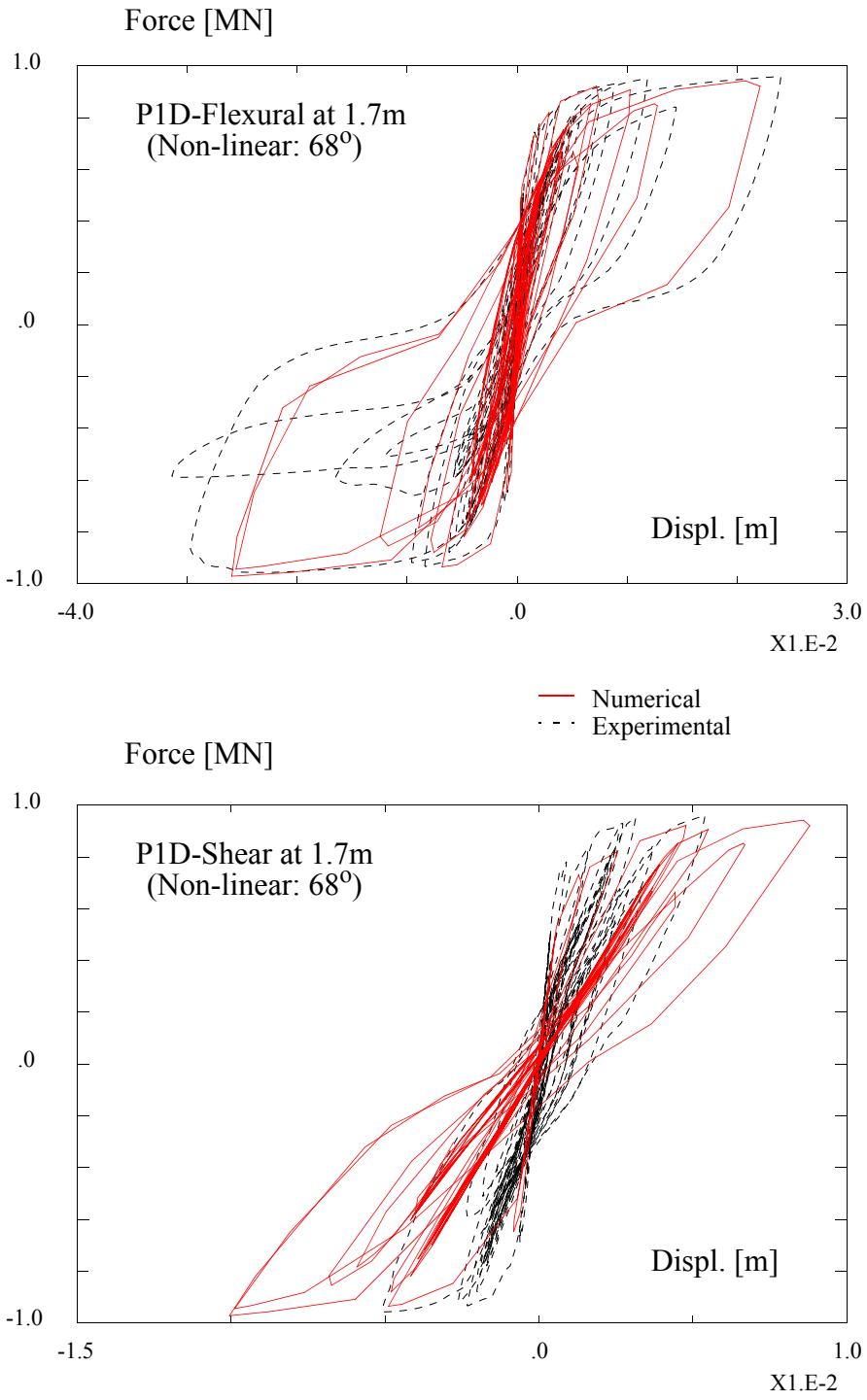

Figure 9.3 - Numerical versus experimental force-flexural and shear displacement response curves at 1.7m from the bottom, for pier P1D, using the non-linear shear model with θ=68°

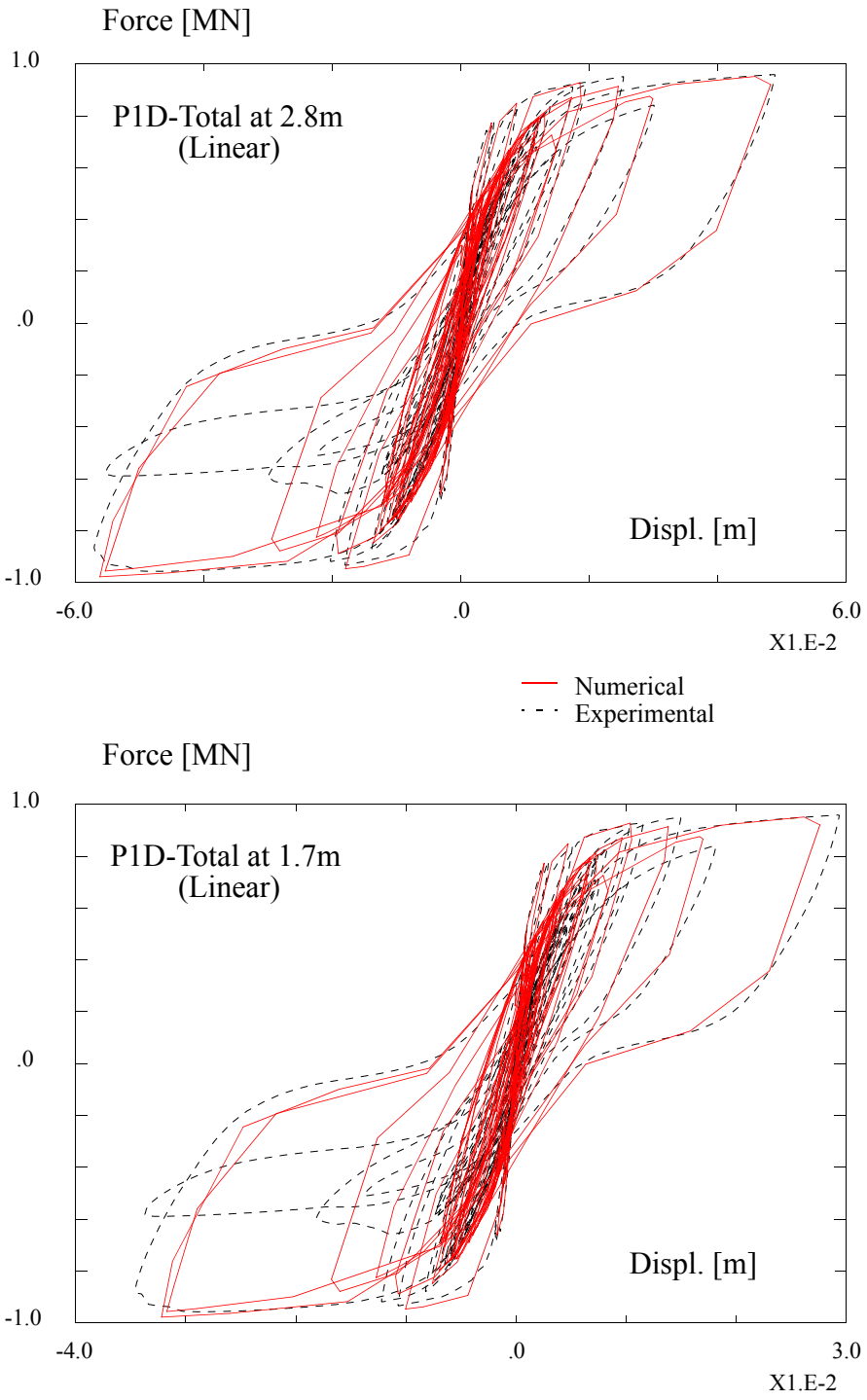

Figure 9.4 - Numerical versus experimental force-total displacement response curves for pier P1D at two different height levels and using the linear elastic shear model

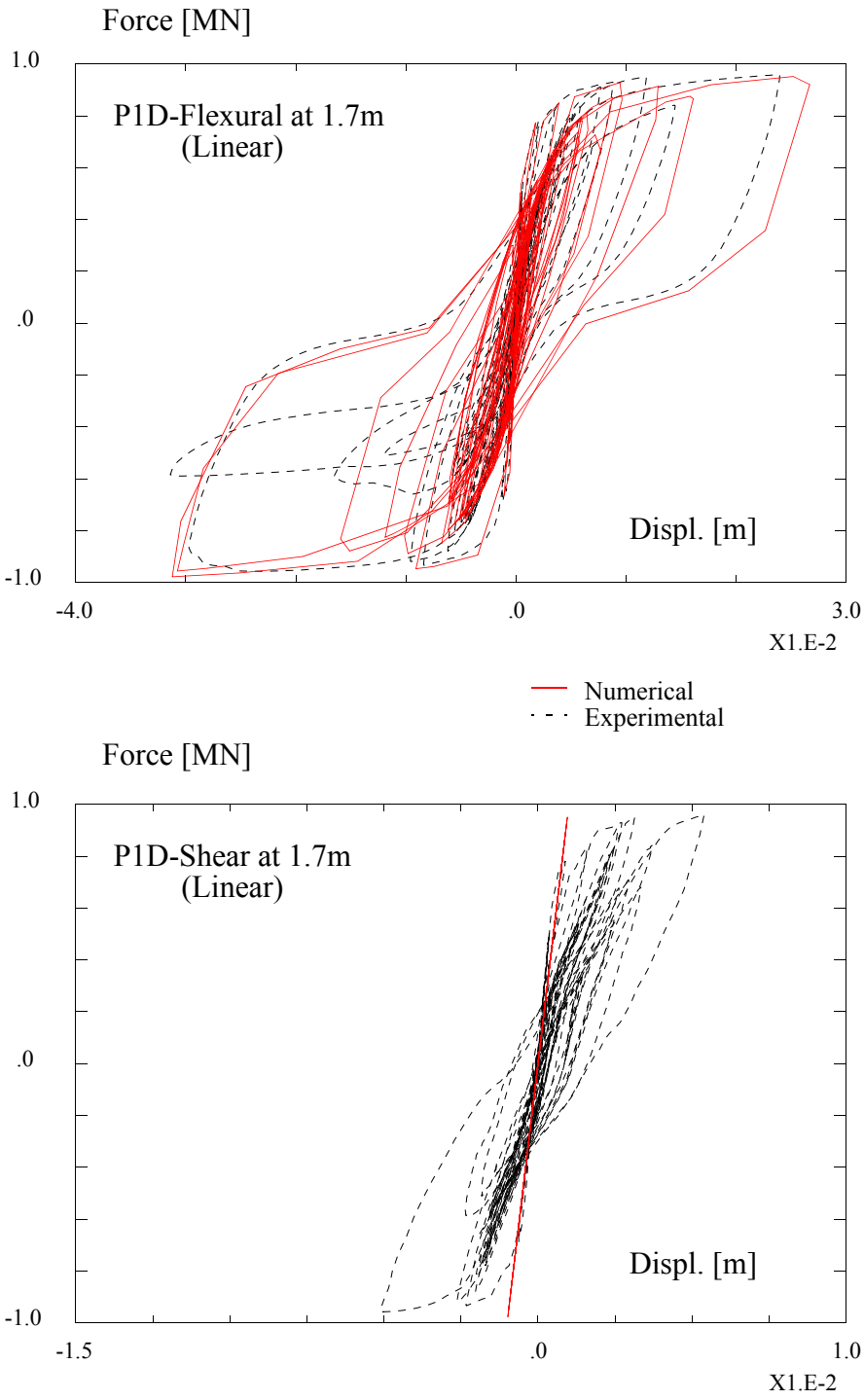

Figure 9.5 - Numerical versus experimental force-flexural and shear displacement response curves at 1.7m from the bottom, for pier P1D, using the linear shear model

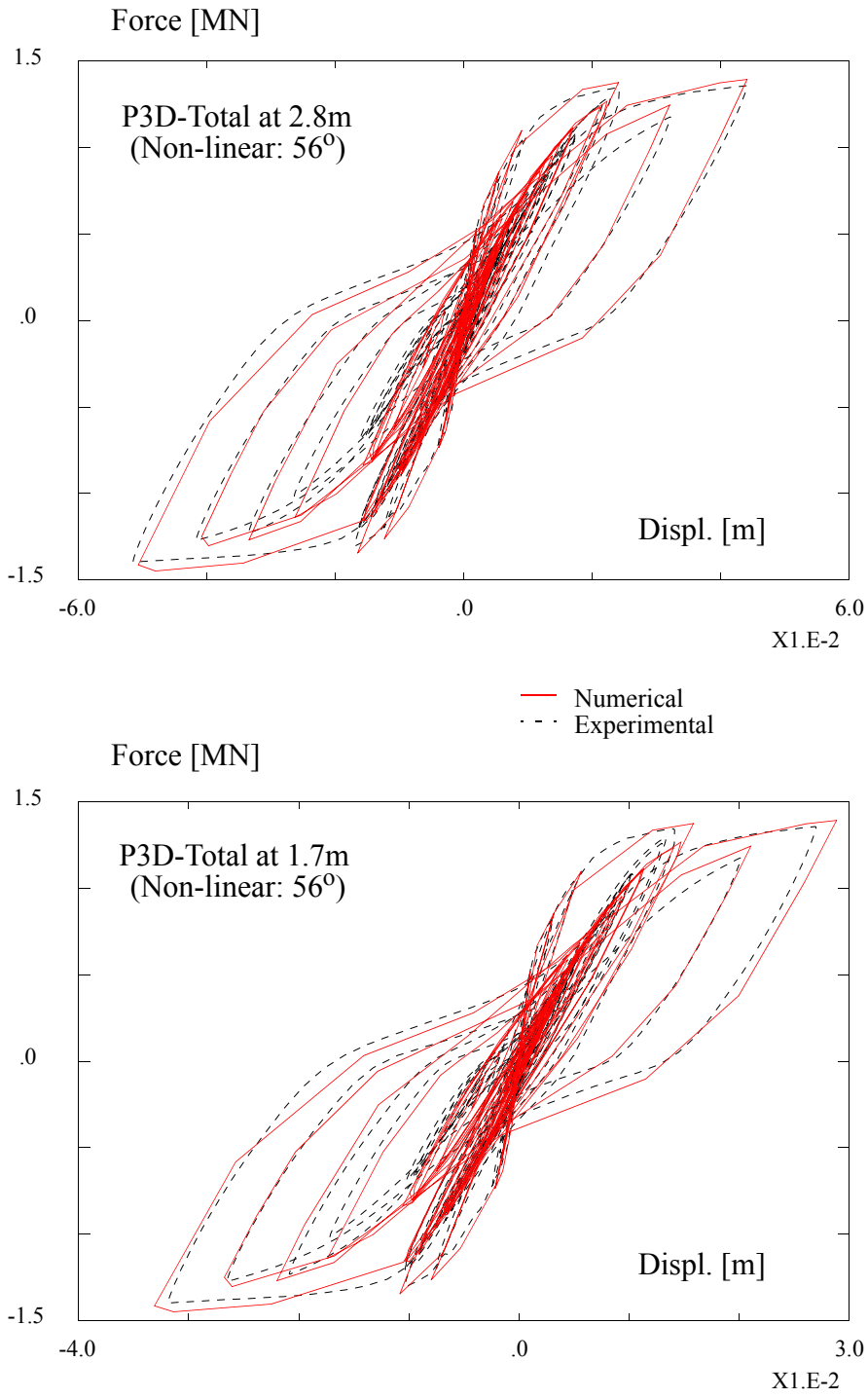

Figure 9.6 - Numerical versus experimental force-total displacement response curves for pier P3D at two different height levels and using the non-linear elastic shear model with θ=56°

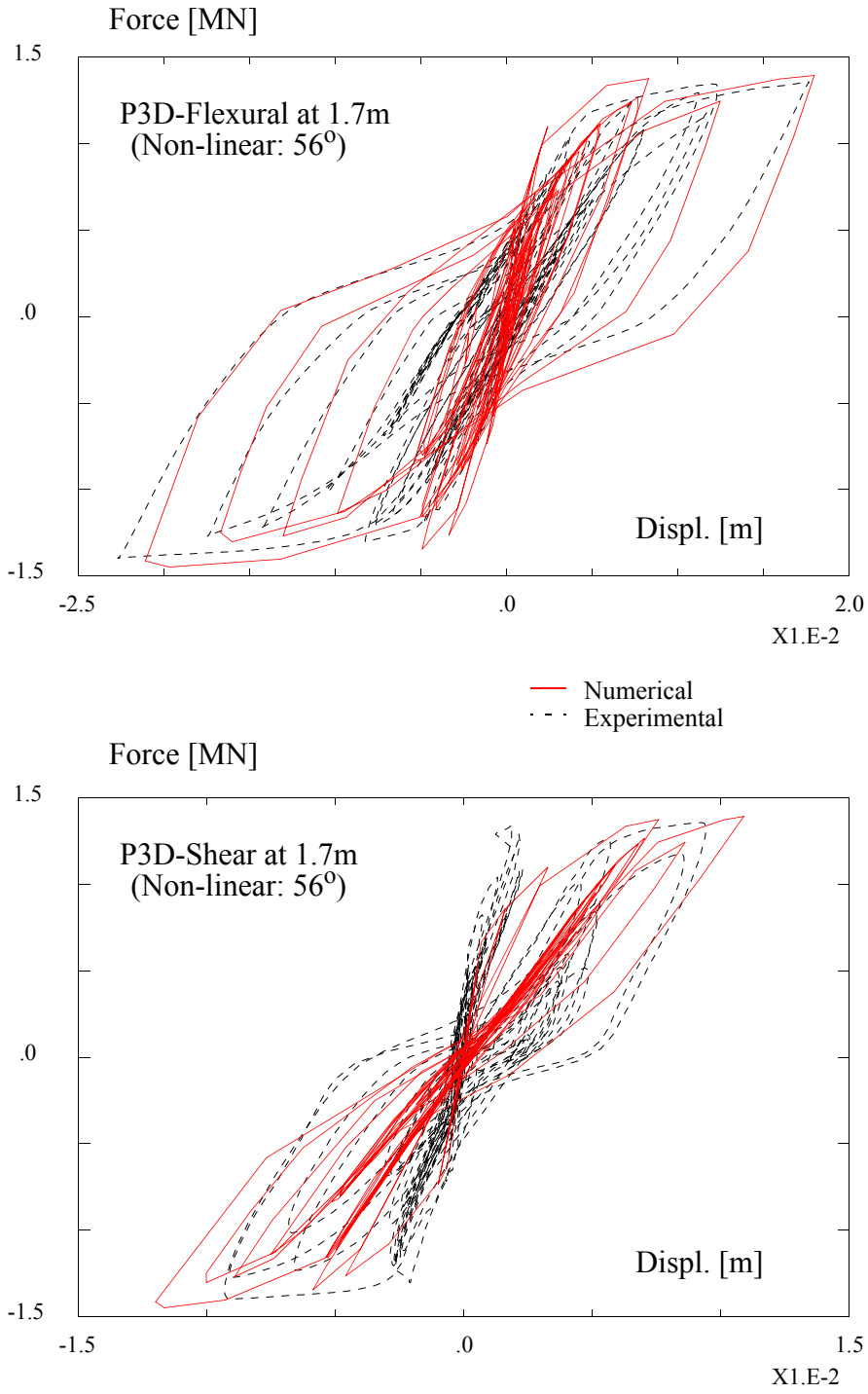

Figure 9.7 - Numerical versus experimental force-flexural and shear displacement response curves at 1.7m from the bottom, for pier P3D, using the non-linear shear model with θ=56°

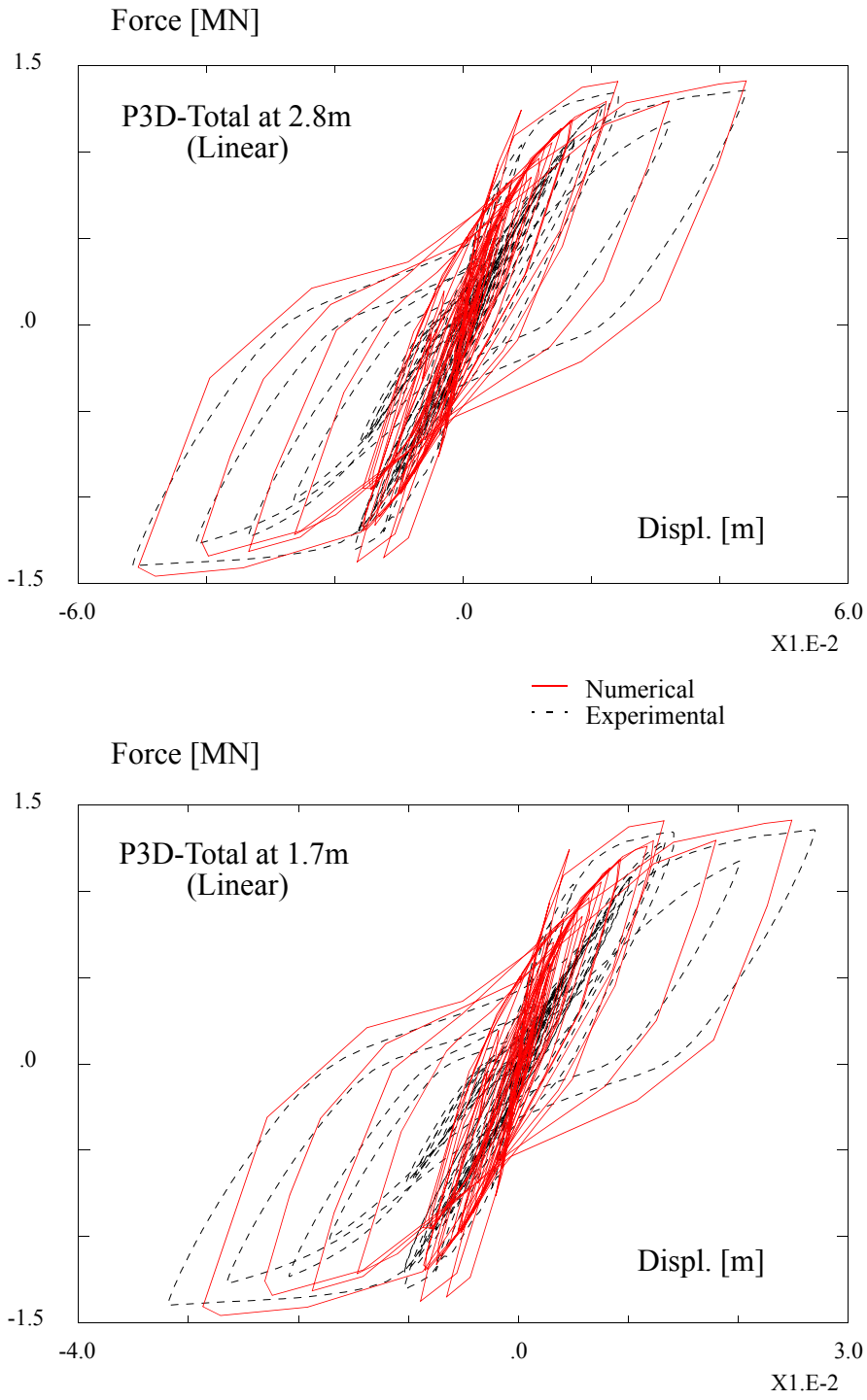

Figure 9.8 - Numerical versus experimental force-total displacement response curves for pier P3D at two different height levels and using the linear elastic shear model

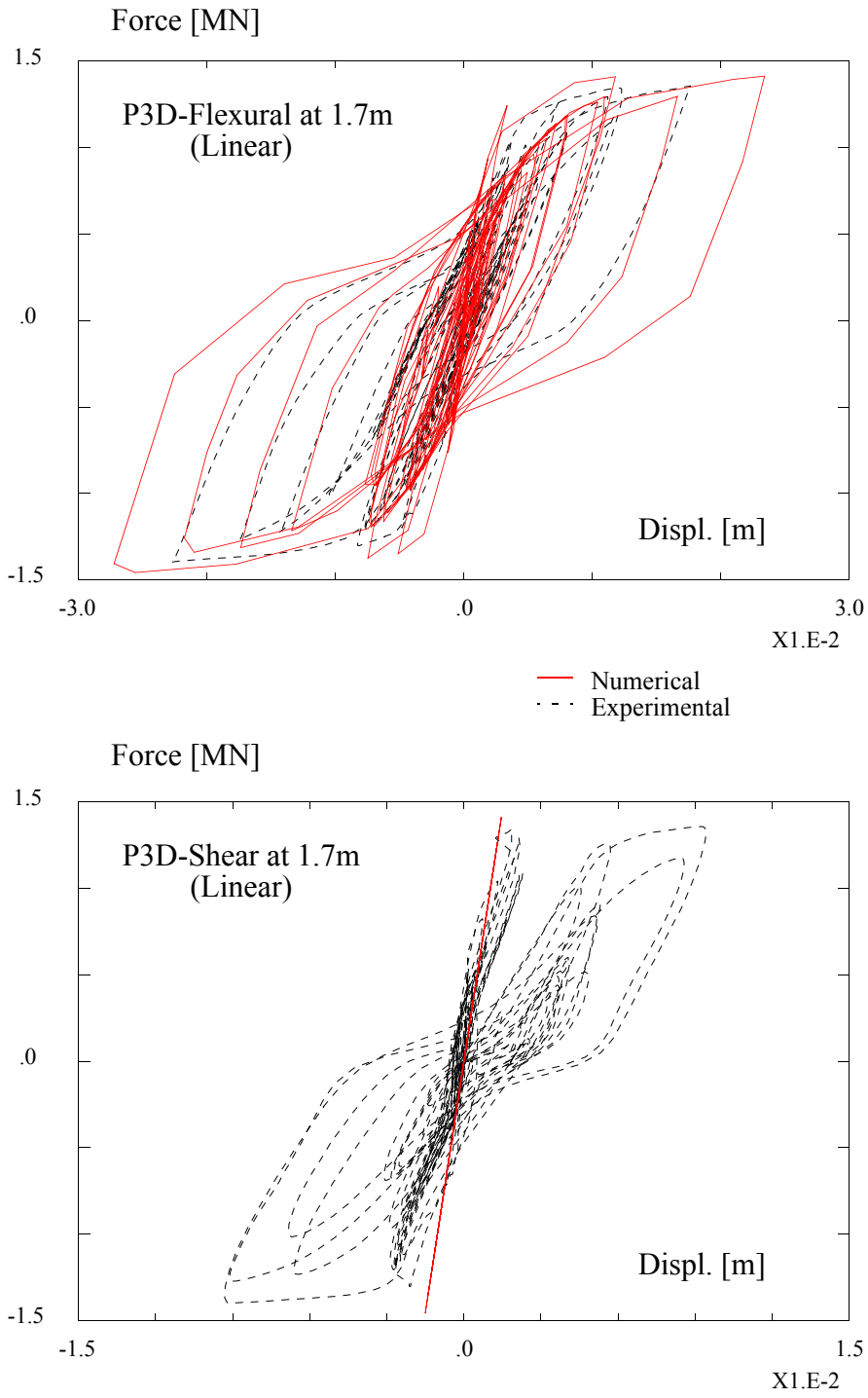

Figure 9.9 - Numerical versus experimental force-flexural and shear displacement response curves at 1.7m from the bottom, for pier P3D, using the linear elastic shear model

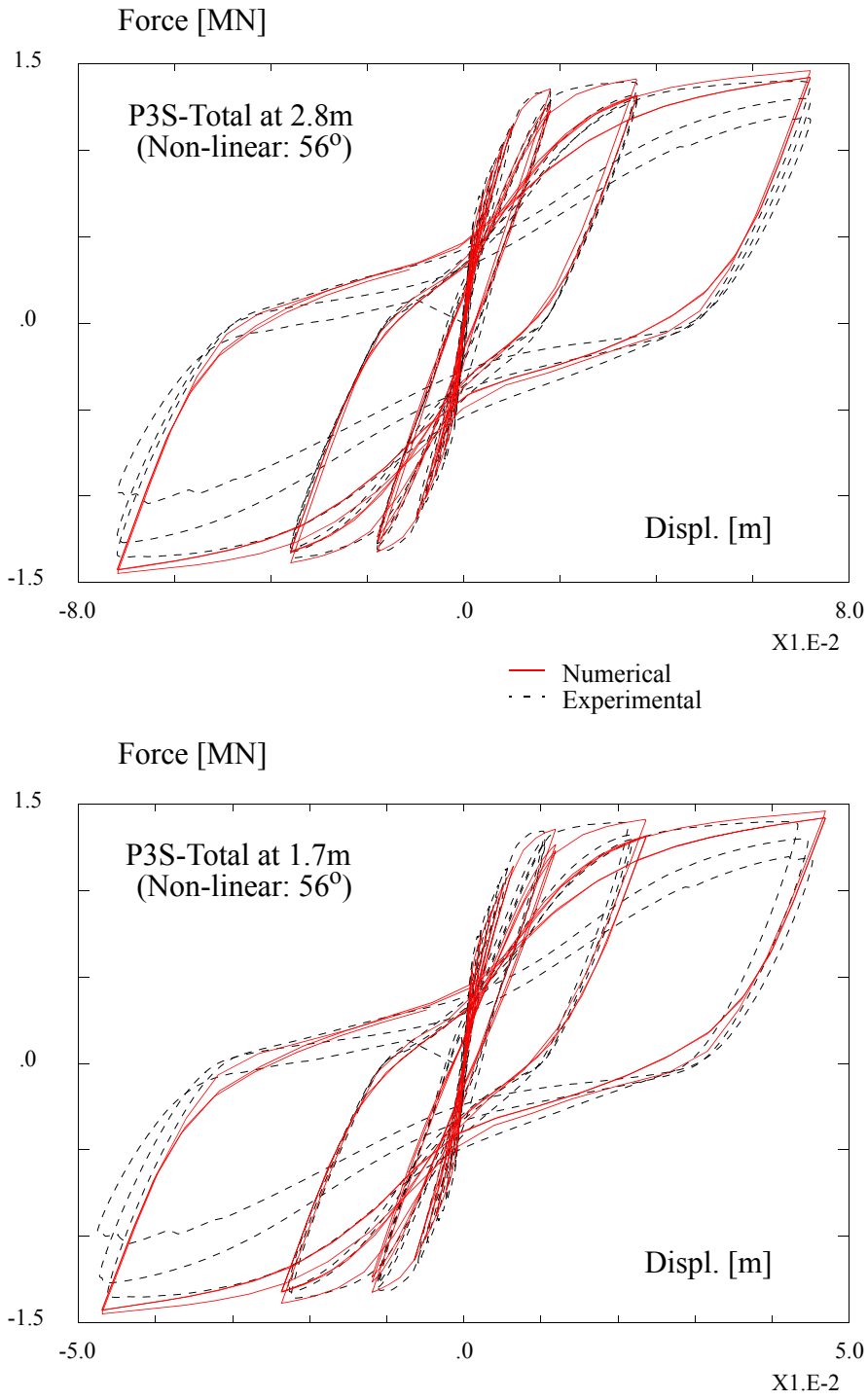

Figure 9.10 - Numerical versus experimental force-total displacement response curves for pier P3S at two different height levels and using the non-linear shear model with θ=56°

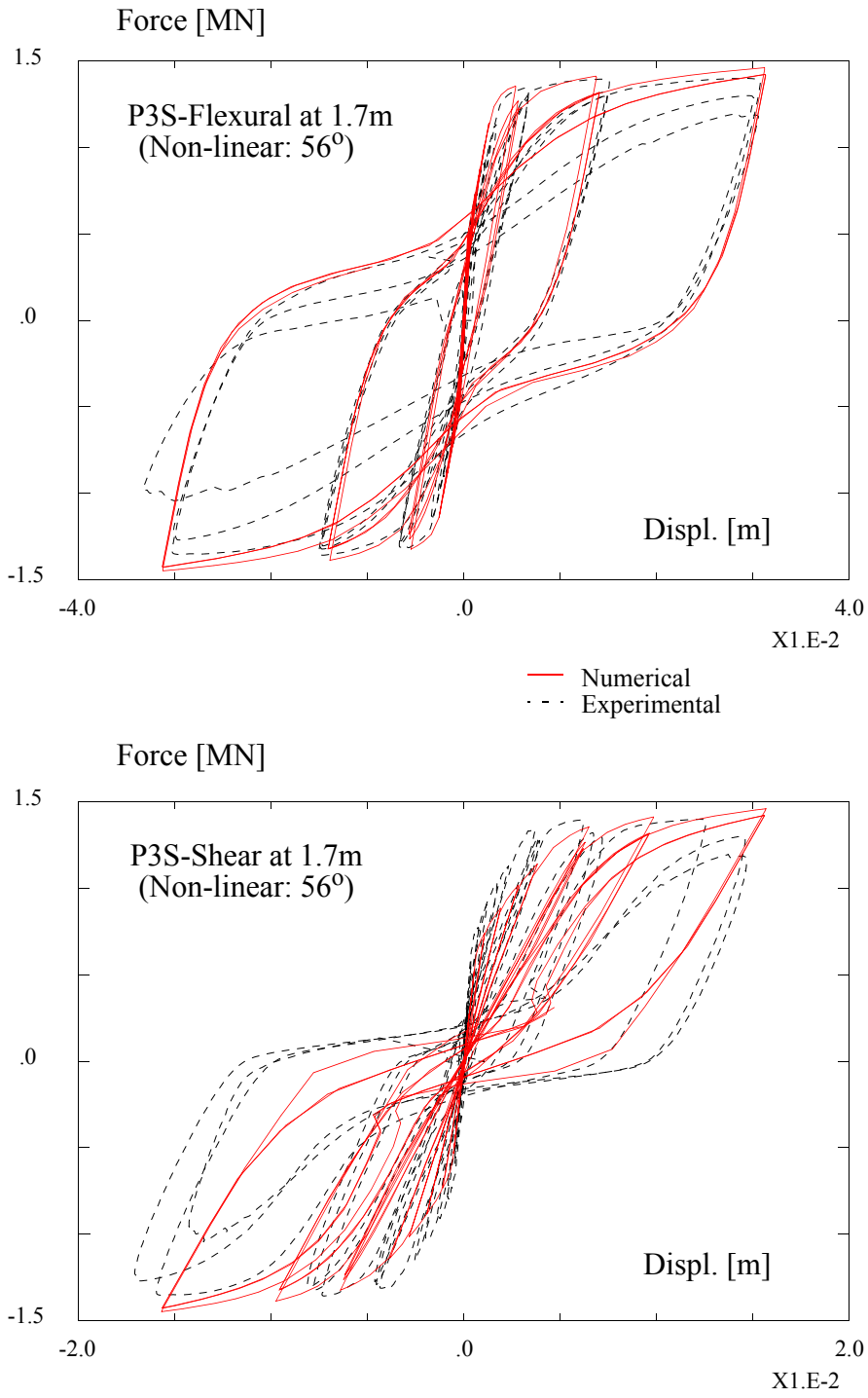

Figure 9.11 - Numerical versus experimental force-flexural and shear displacement response curves at 1.7m from the bottom, for pier P3S, using the non-linear shear model with $\theta=56^{o}$

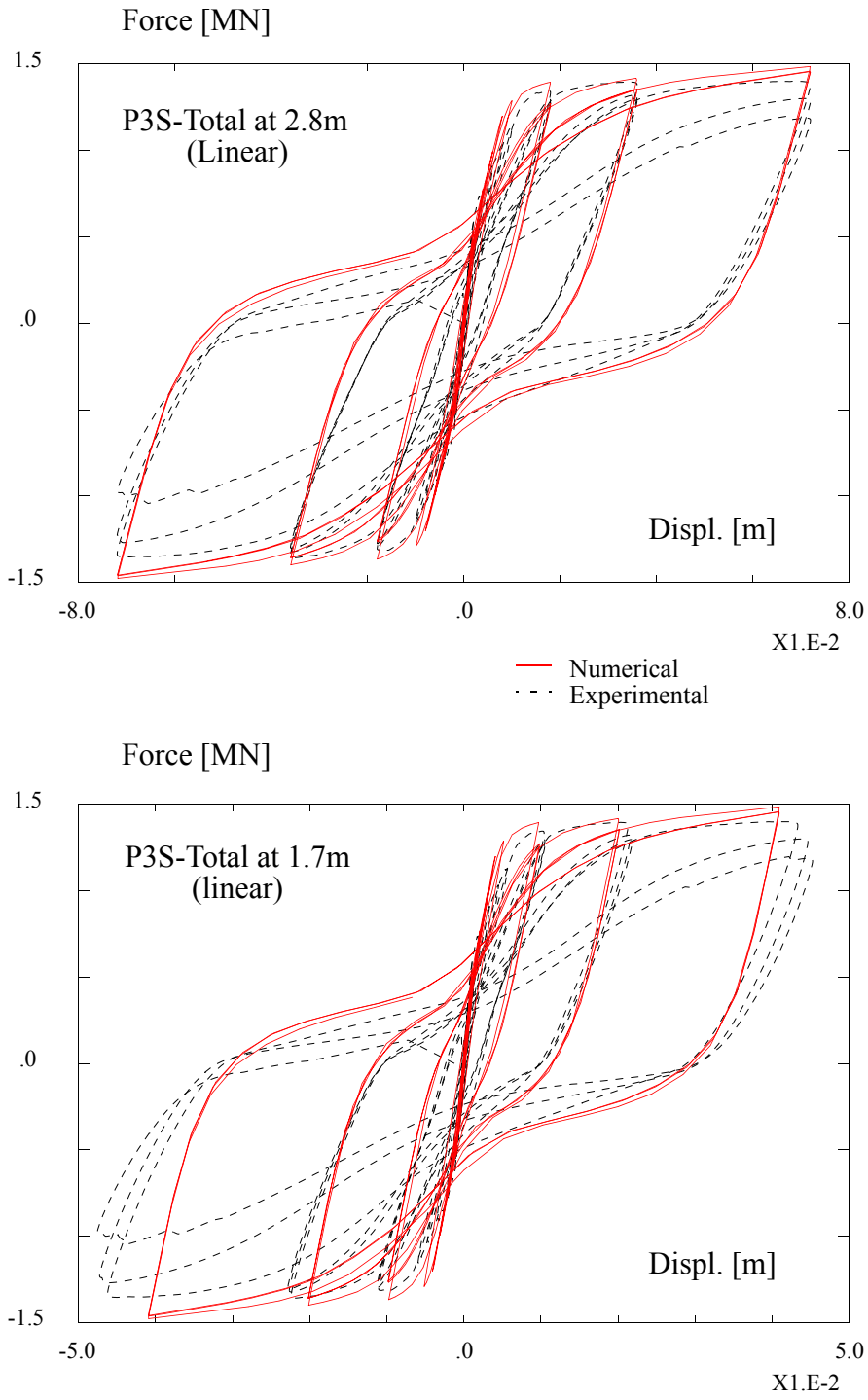

Figure 9.12 - Numerical versus experimental force-total displacement response curves for pier P3S at two different height levels and using the linear elastic shear model

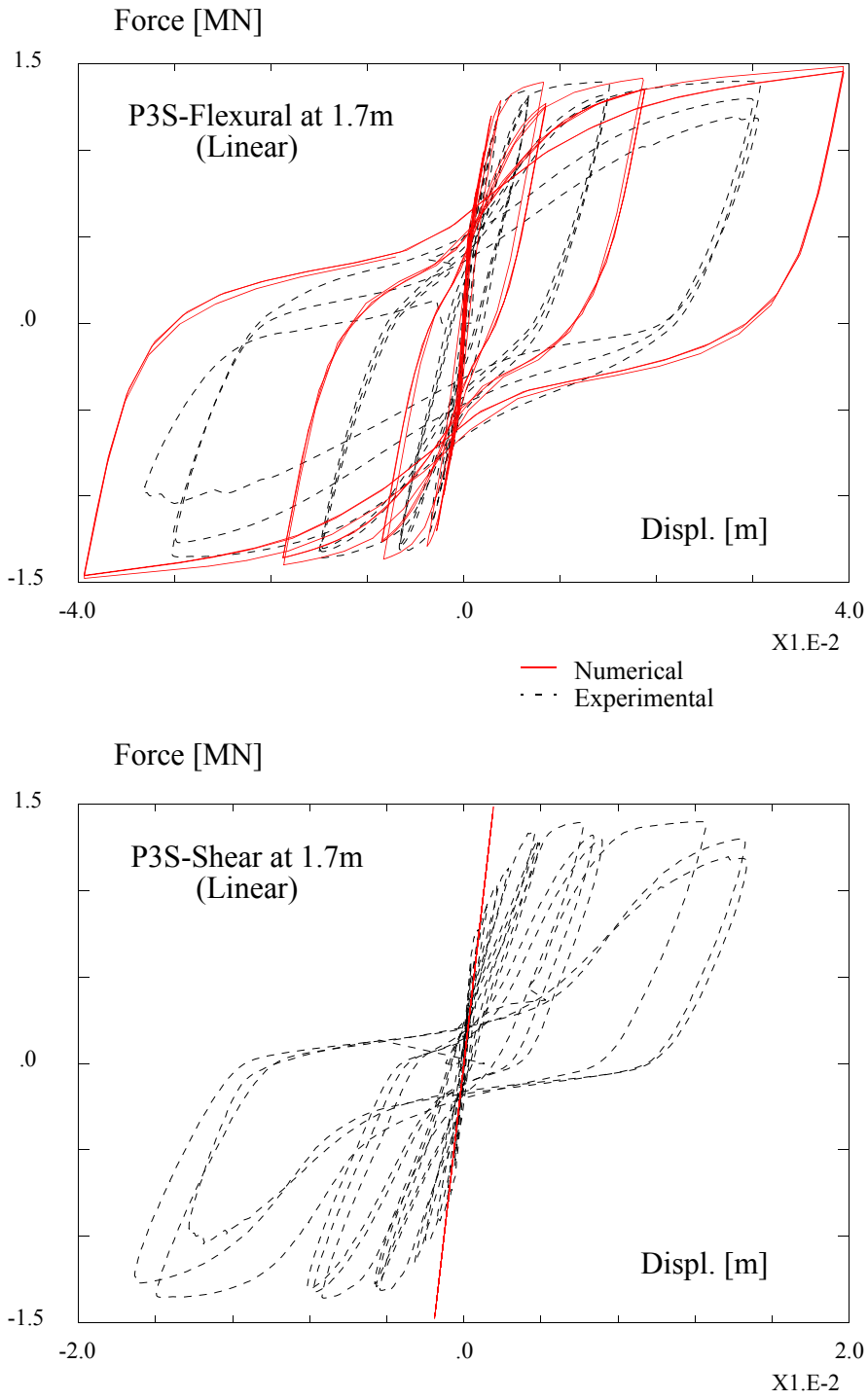

Figure 9.13 - Numerical versus experimental force-flexural and shear displacement response curves at 1.7m from the bottom, for pier P3S, using the linear elastic shear model

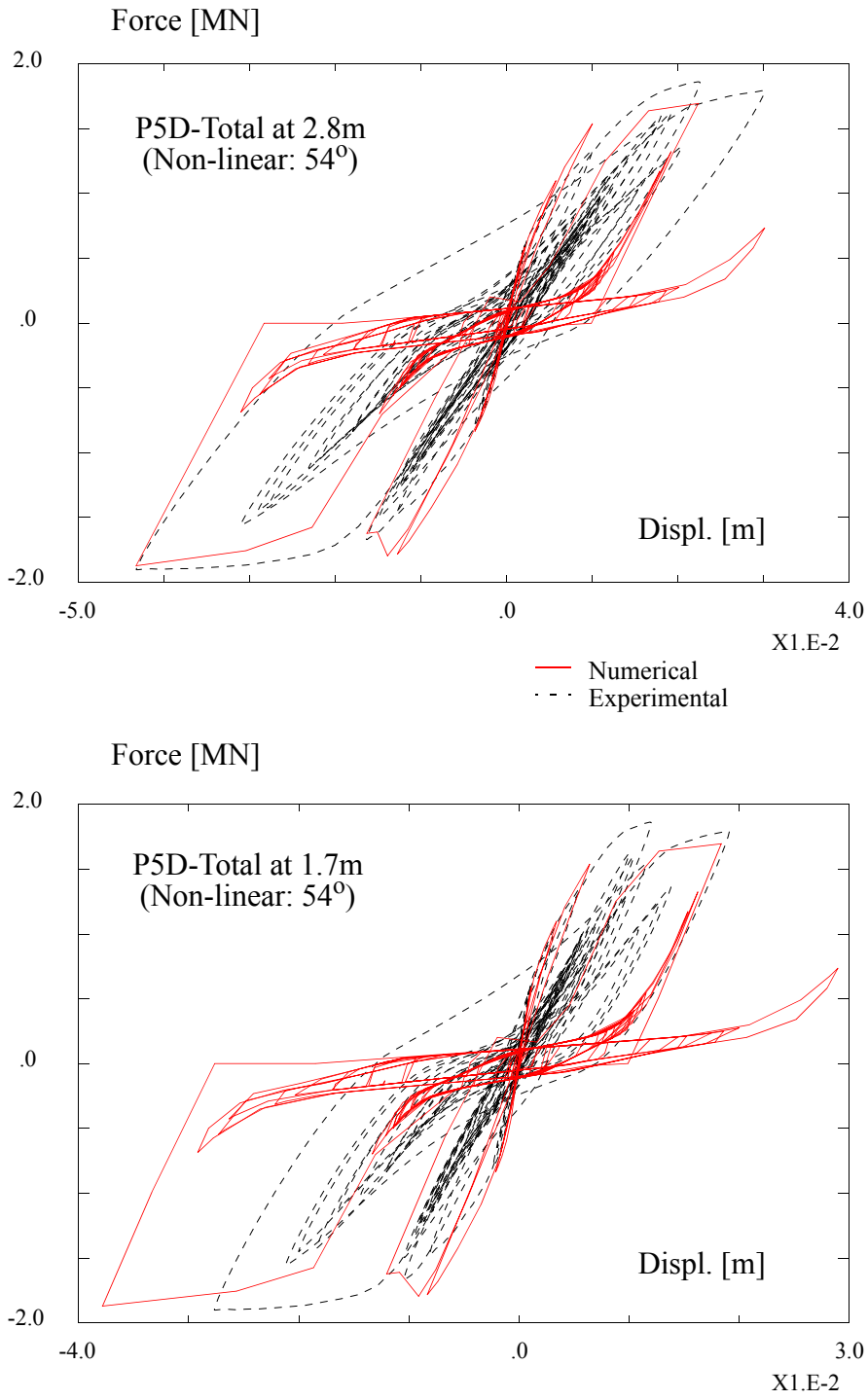

Figure 9.14 - Numerical versus experimental force-total displacement response curves for pier P5D at two different height levels and using the non-linear shear model with θ=54^o

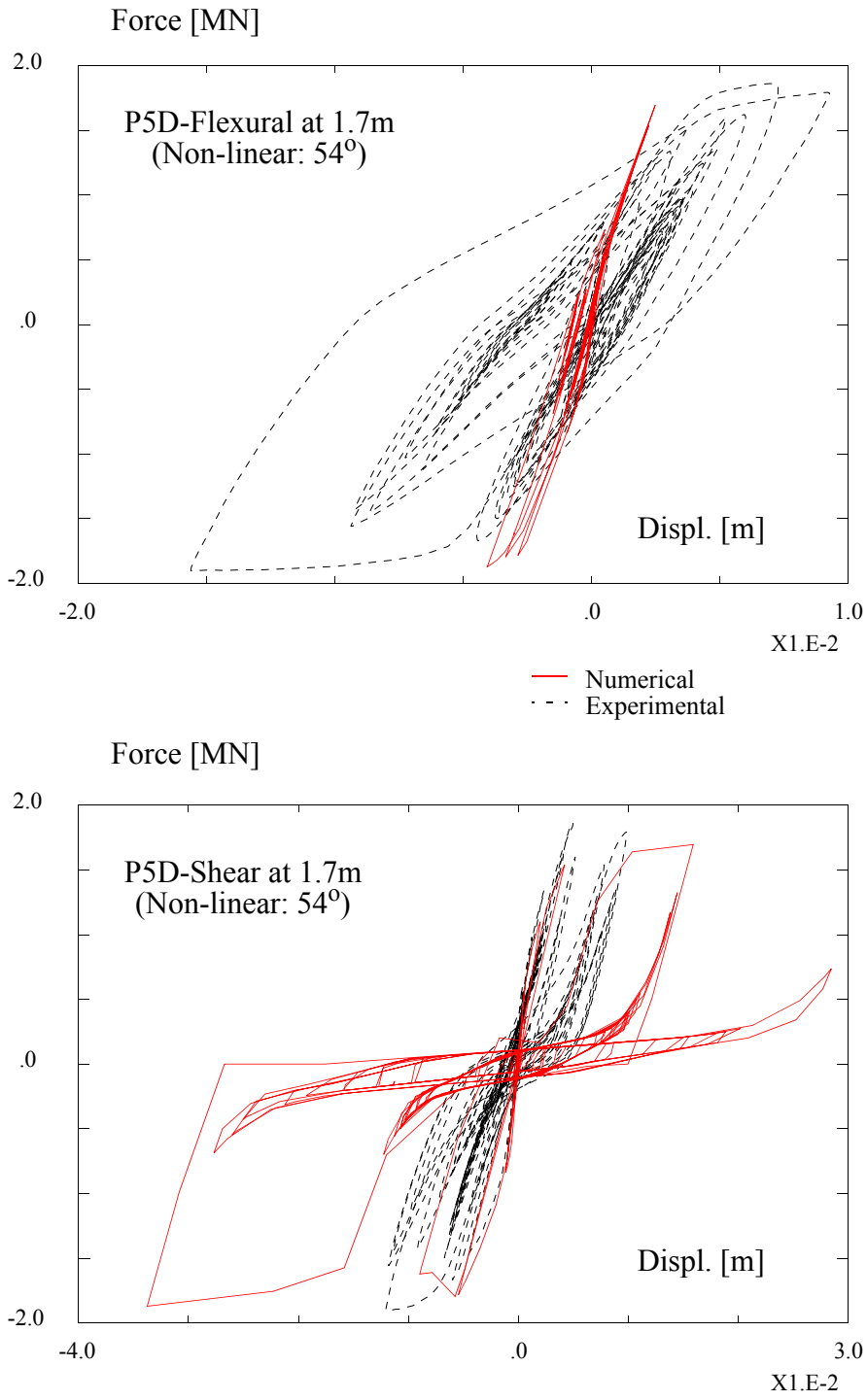

Figure 9.15 - Numerical versus experimental force-flexural and shear displacement response curves at 1.7m from the bottom, for pier P5D, using the non-linear shear model with $\theta=54^{o}$

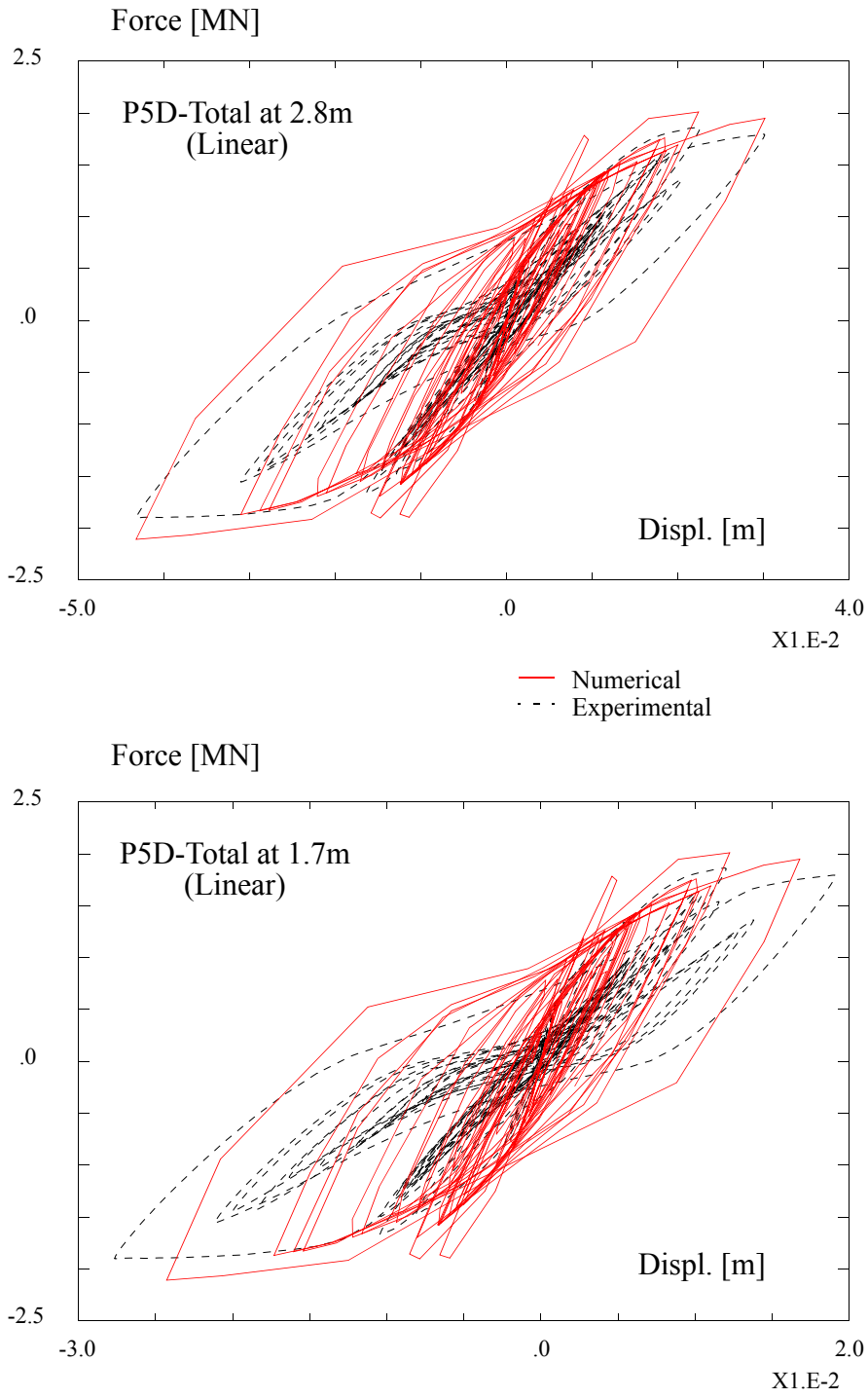

Figure 9.16 - Numerical versus experimental force-total displacement response curves for pier P5D at two different height levels and using the linear elastic shear model

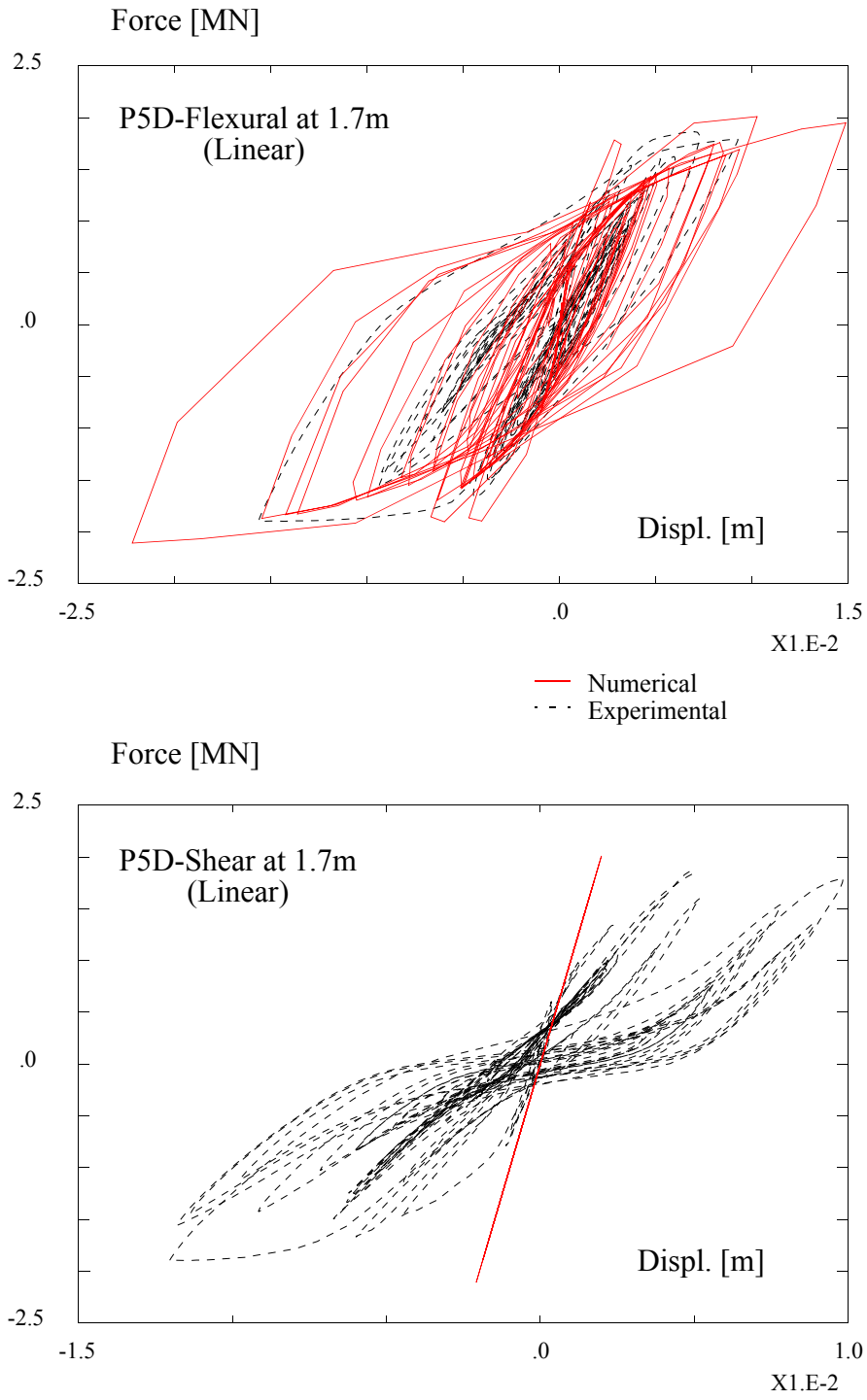

Figure 9.17 - Numerical versus experimental force-flexural and shear displacement response curves at 1.7m from the bottom, for pier P5D, using the linear elastic shear model

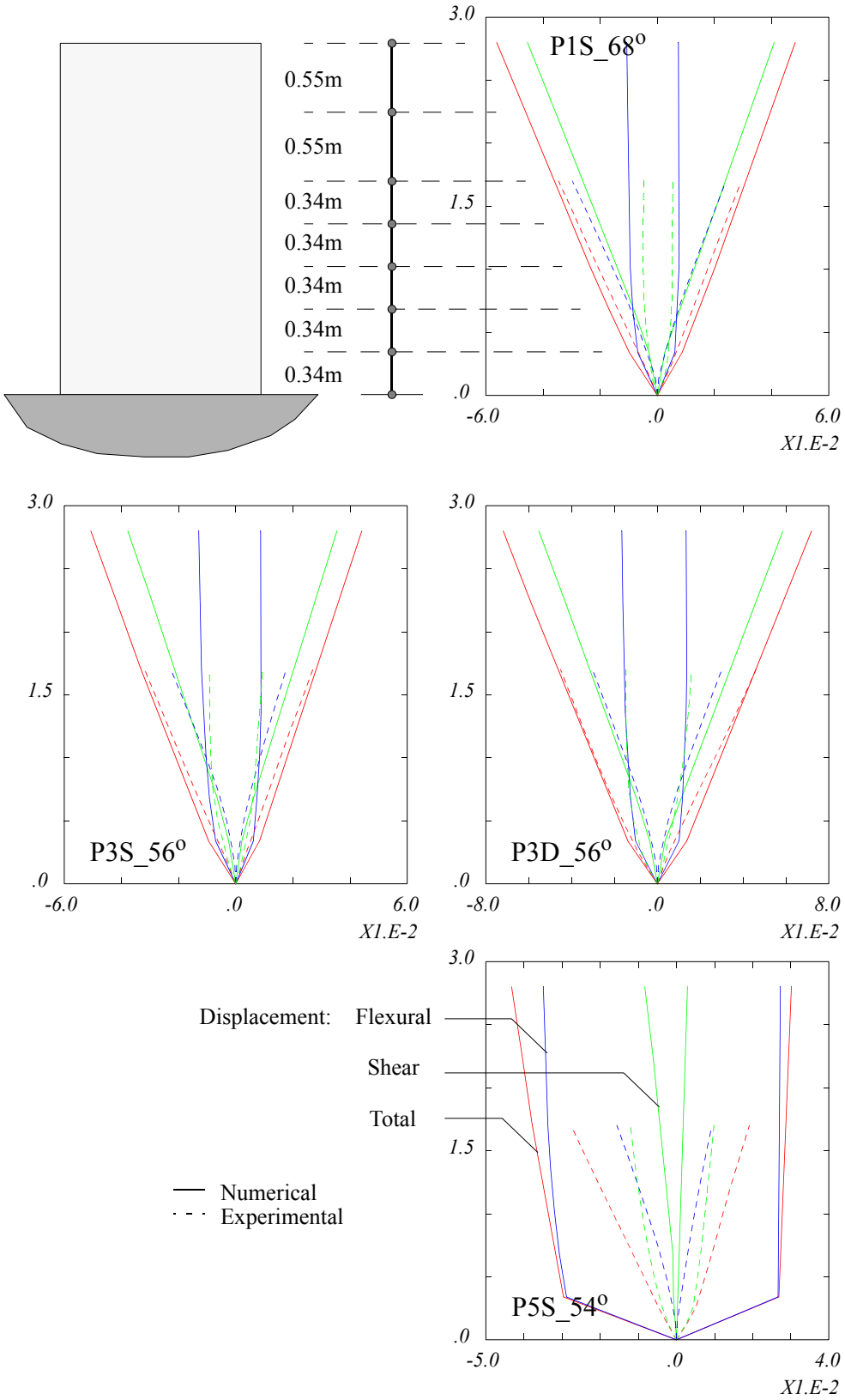

Figure 9.18 - Numerical versus experimental peak displacement profiles for the four piers and the non-linear shear model

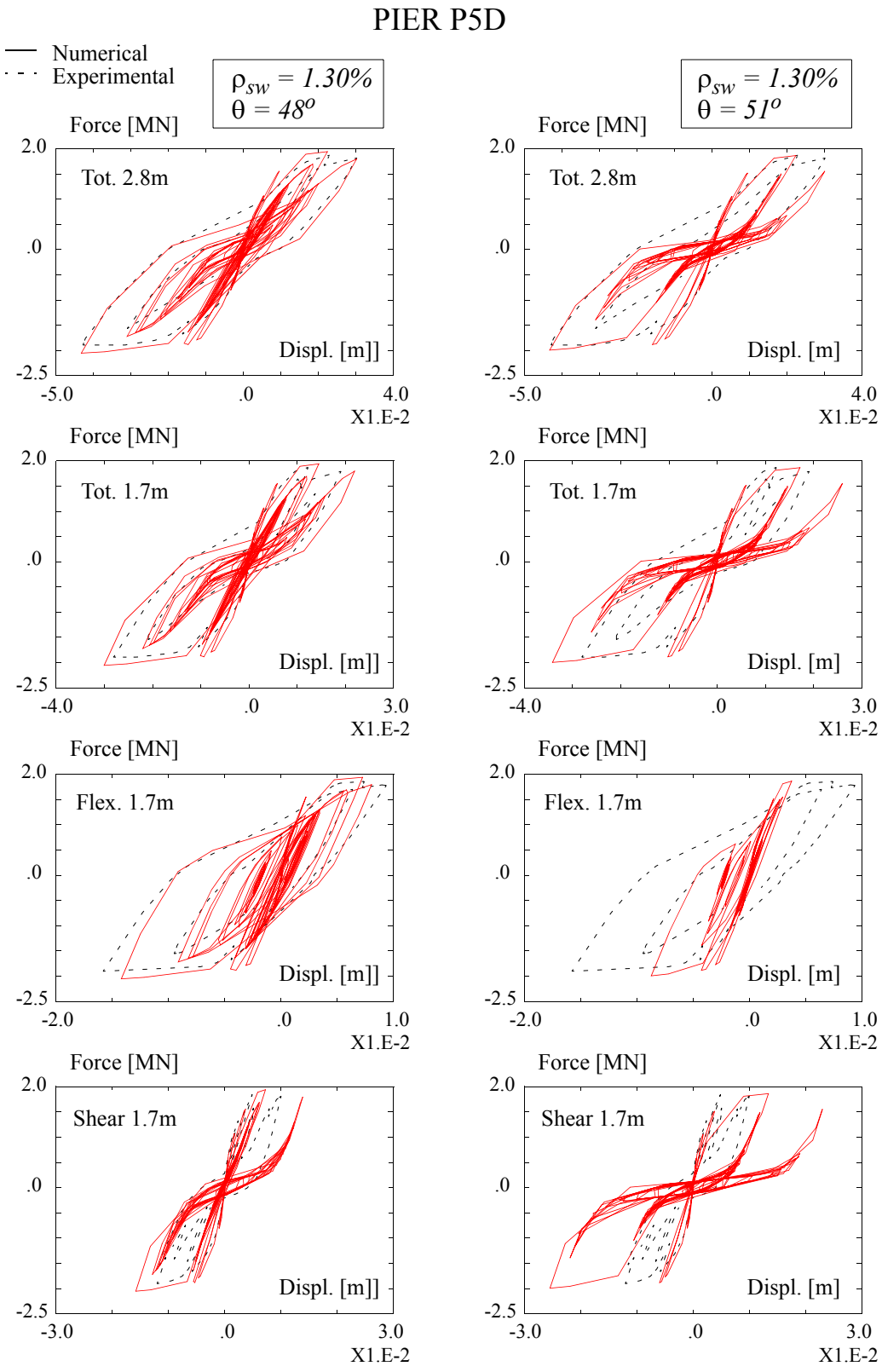

Figure 9.19 - Numerical versus experimental force-total, flexural and shear displacement response curves for pier P5D with different transverse critical cracking angles

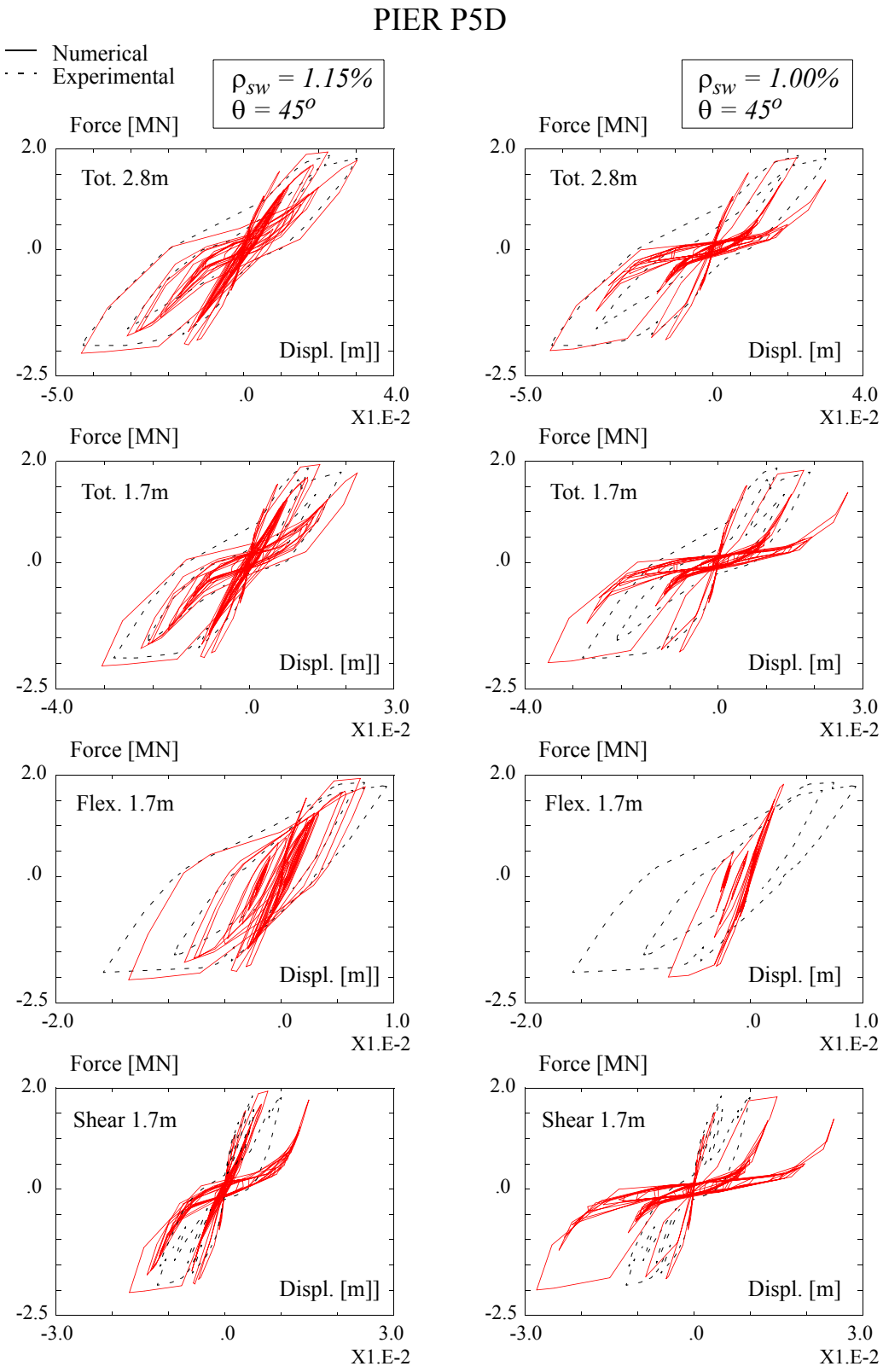

Figure 9.20 - Numerical versus experimental force-total, flexural and shear displacement response curves for pier P5D for different transverse steel ratios

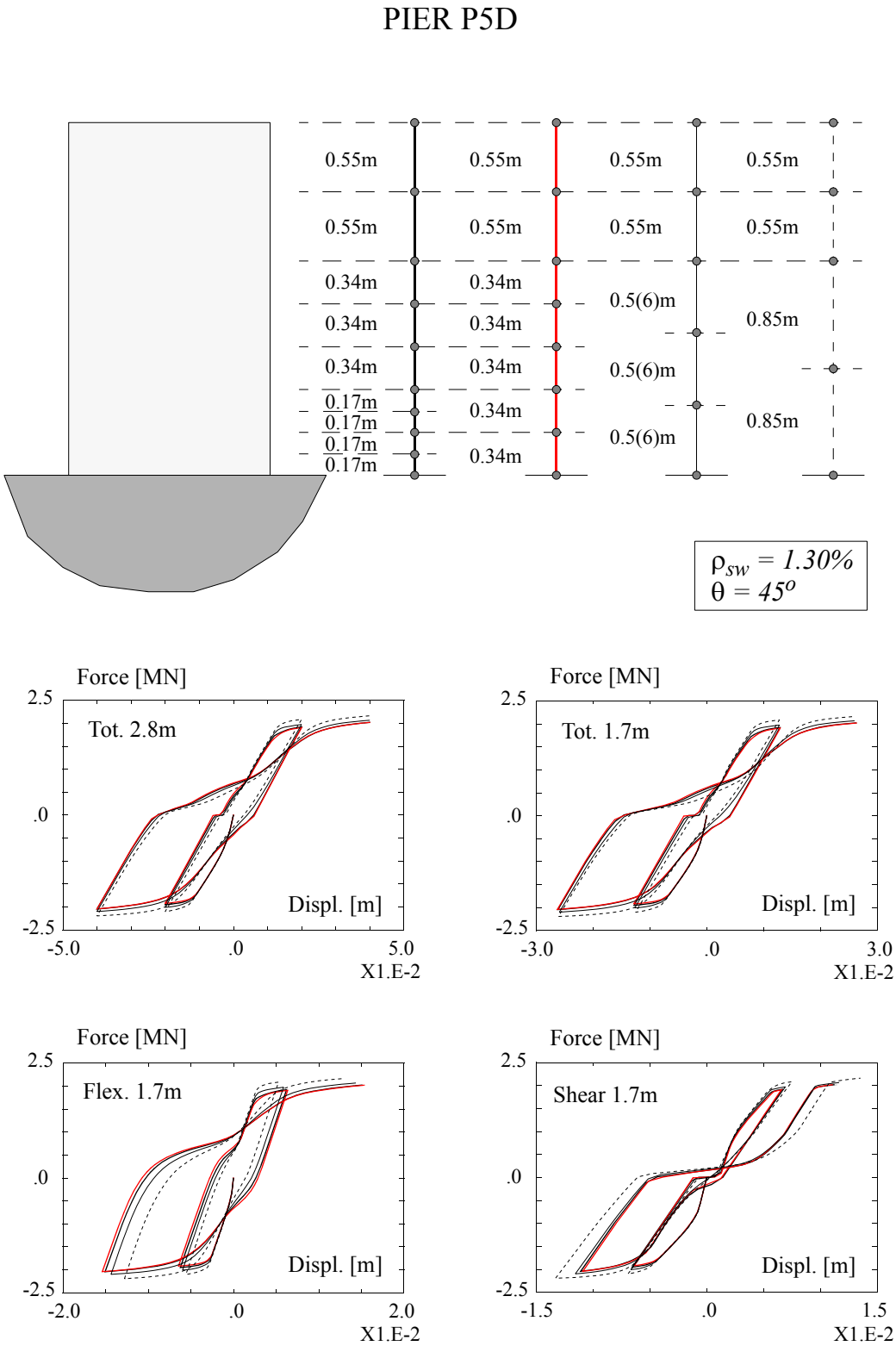

Figure 9.21 - Numerical force versus total, flexural and shear displacement response curves for pier P5D for different mesh discretization

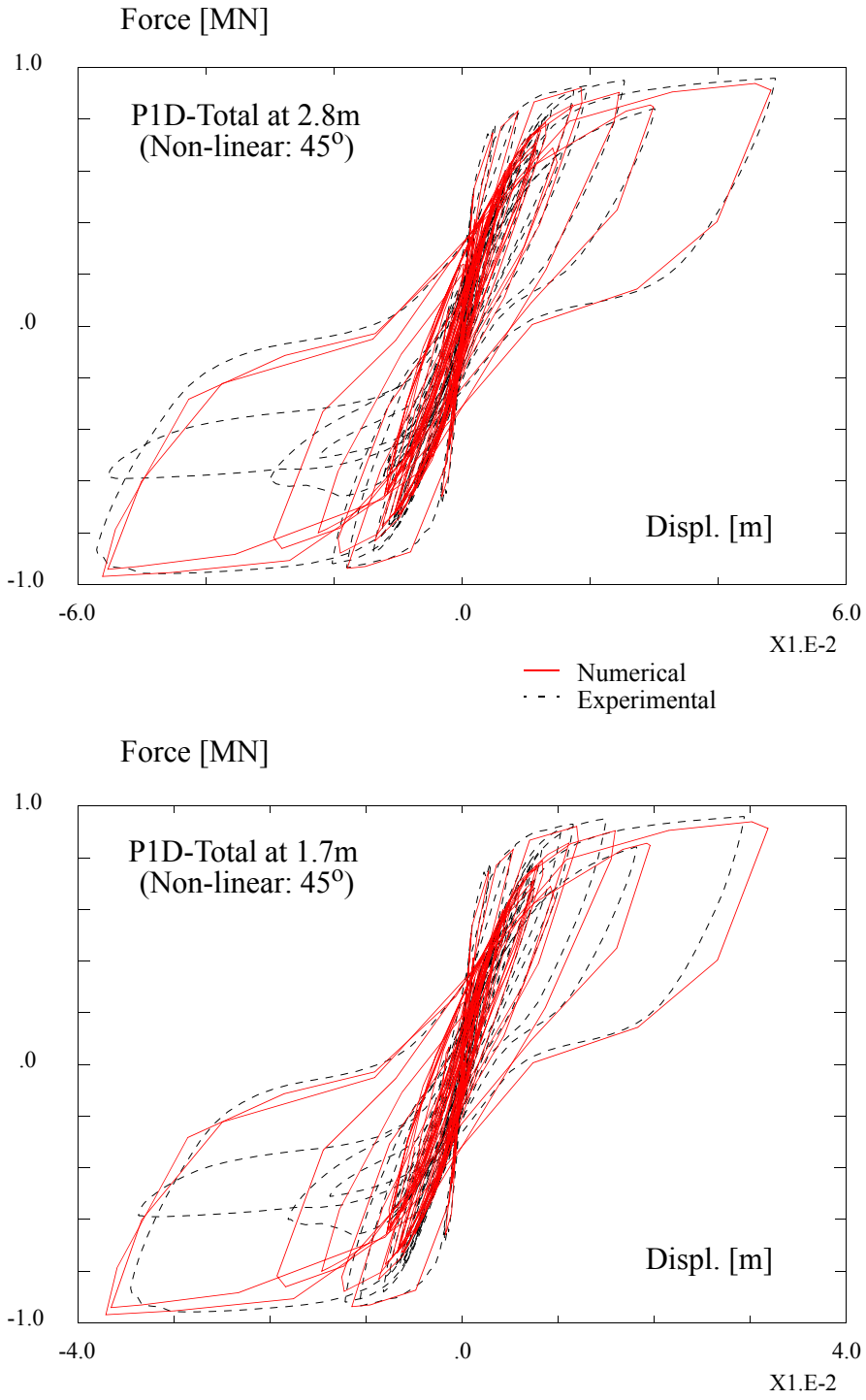

Figure 9.22 - Numerical versus experimental force-total displacement response curves for pier P1D at two different height levels and using the non-linear shear model with θ=45°

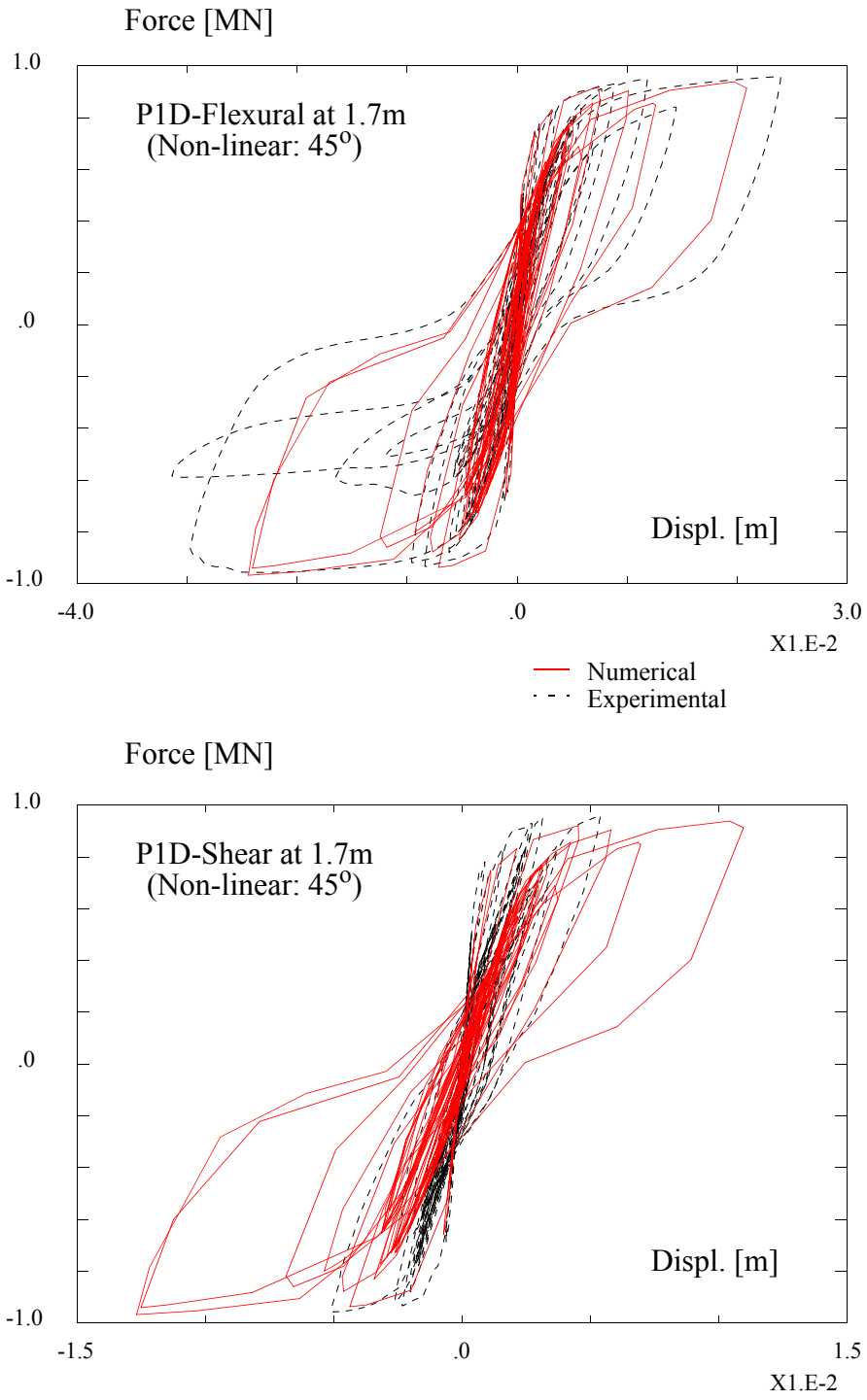

Figure 9.23 - Numerical versus experimental force-flexural and shear displacement response curves at 1.7m from the bottom, for pier P1D, using the non-linear shear model with θ=45º

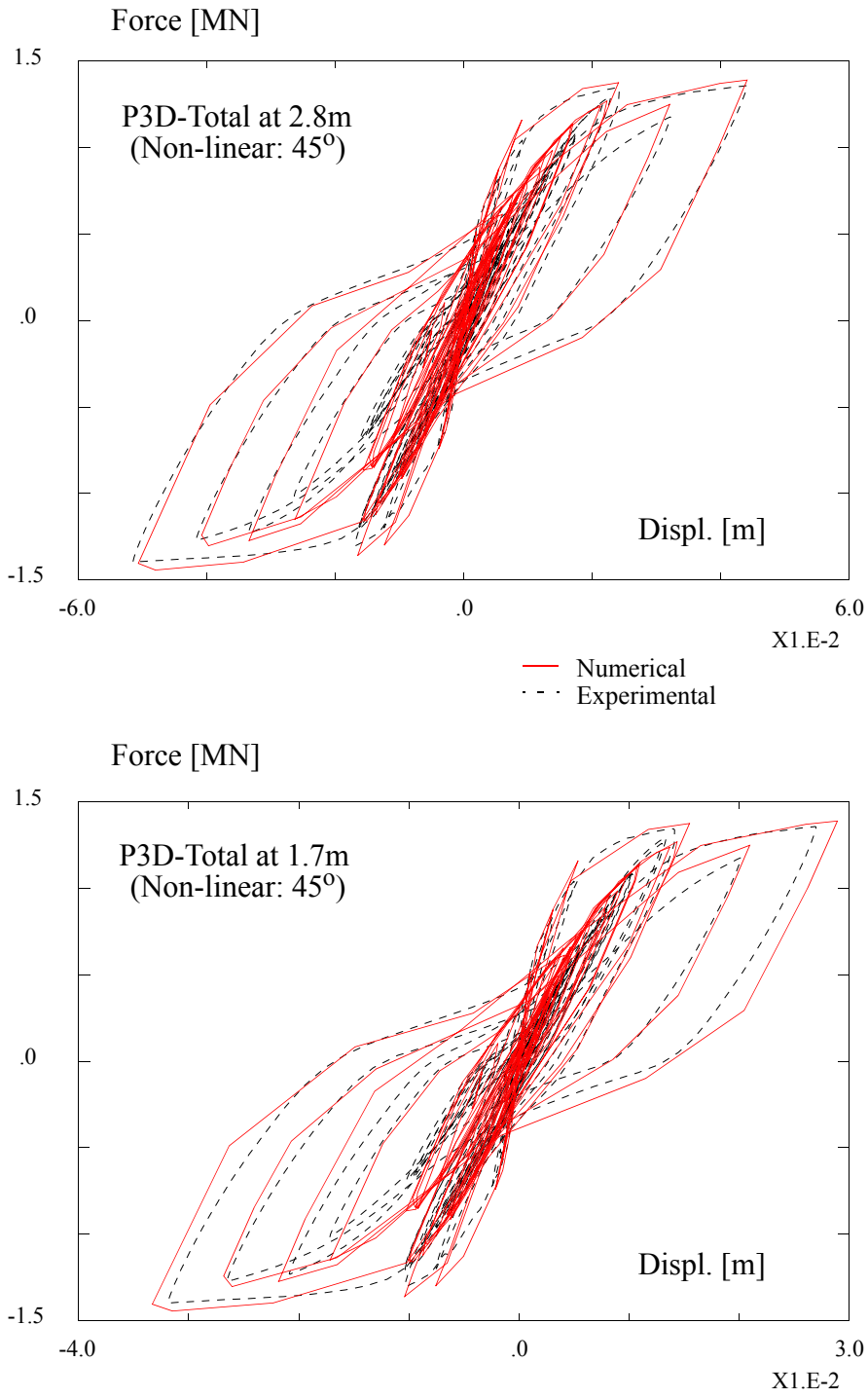

Figure 9.24 - Numerical versus experimental force-total displacement response curves for pier P3D at two different height levels and using the non-linear elastic shear model with θ=45°

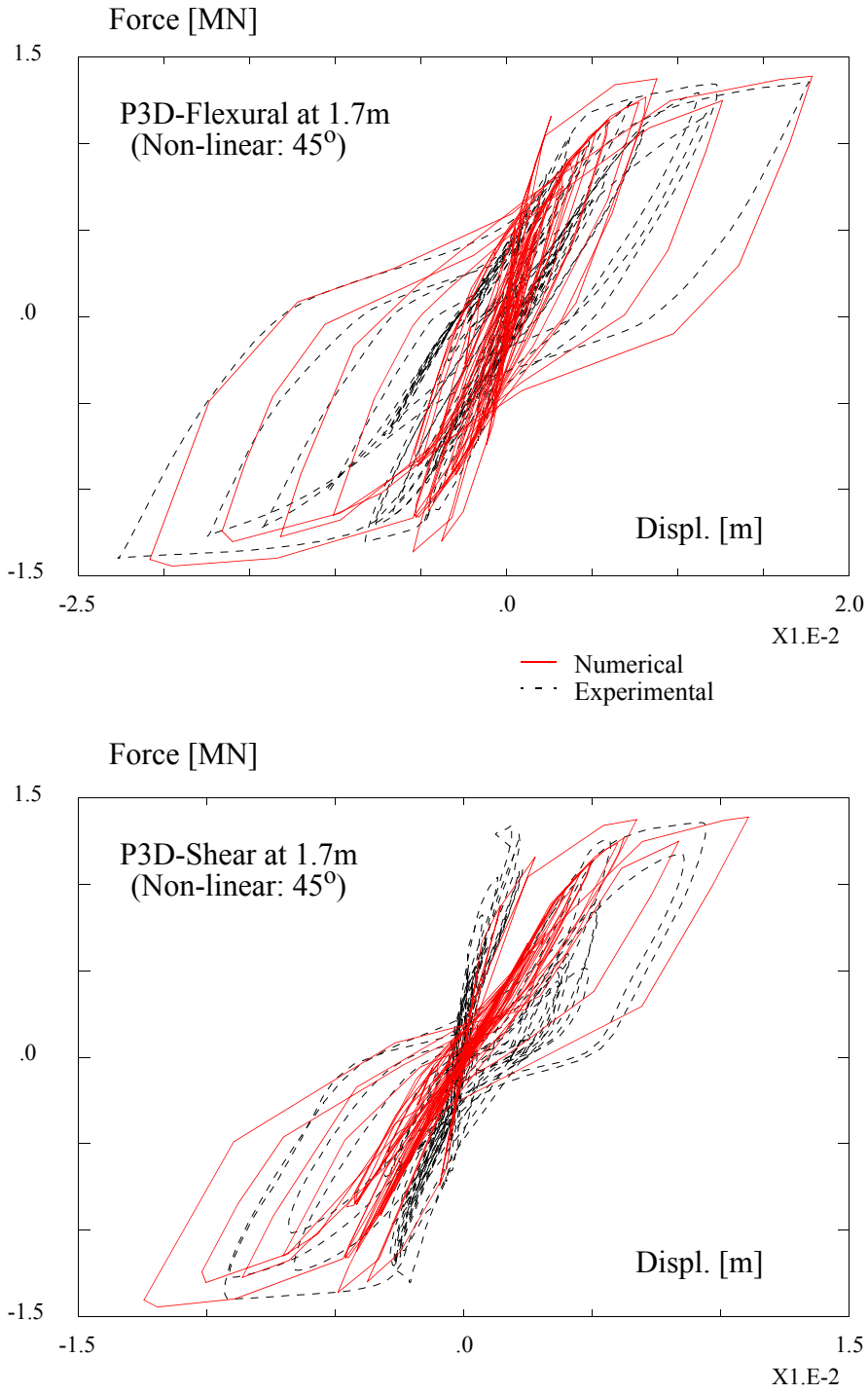

Figure 9.25 - Numerical versus experimental force-flexural and shear displacement response curves at 1.7m from the bottom, for pier P1D, using the non-linear shear model with θ=45º

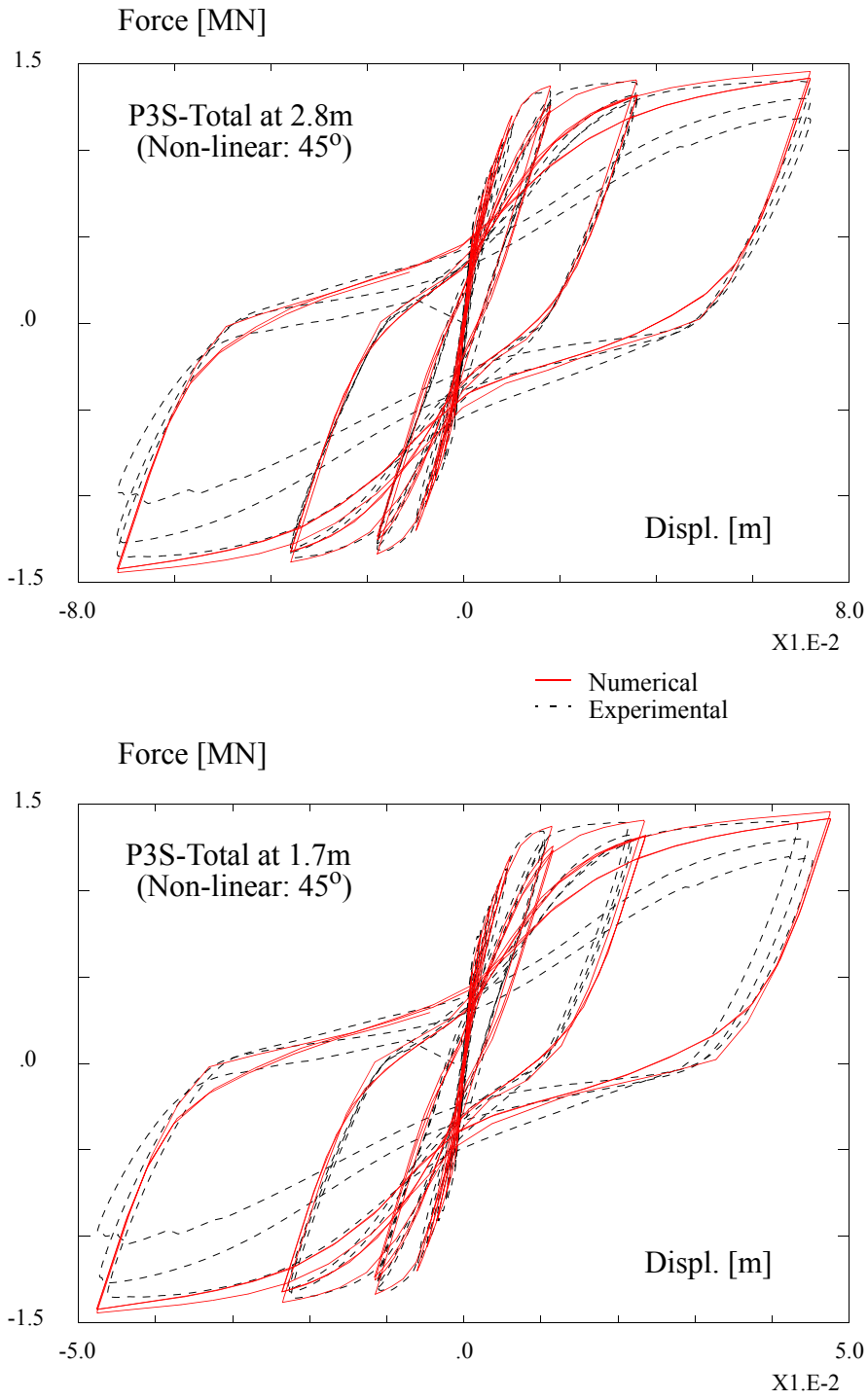

Figure 9.26 - Numerical versus experimental force-total displacement response curves for pier P3S at two different height levels and using the non-linear shear model with θ=45°

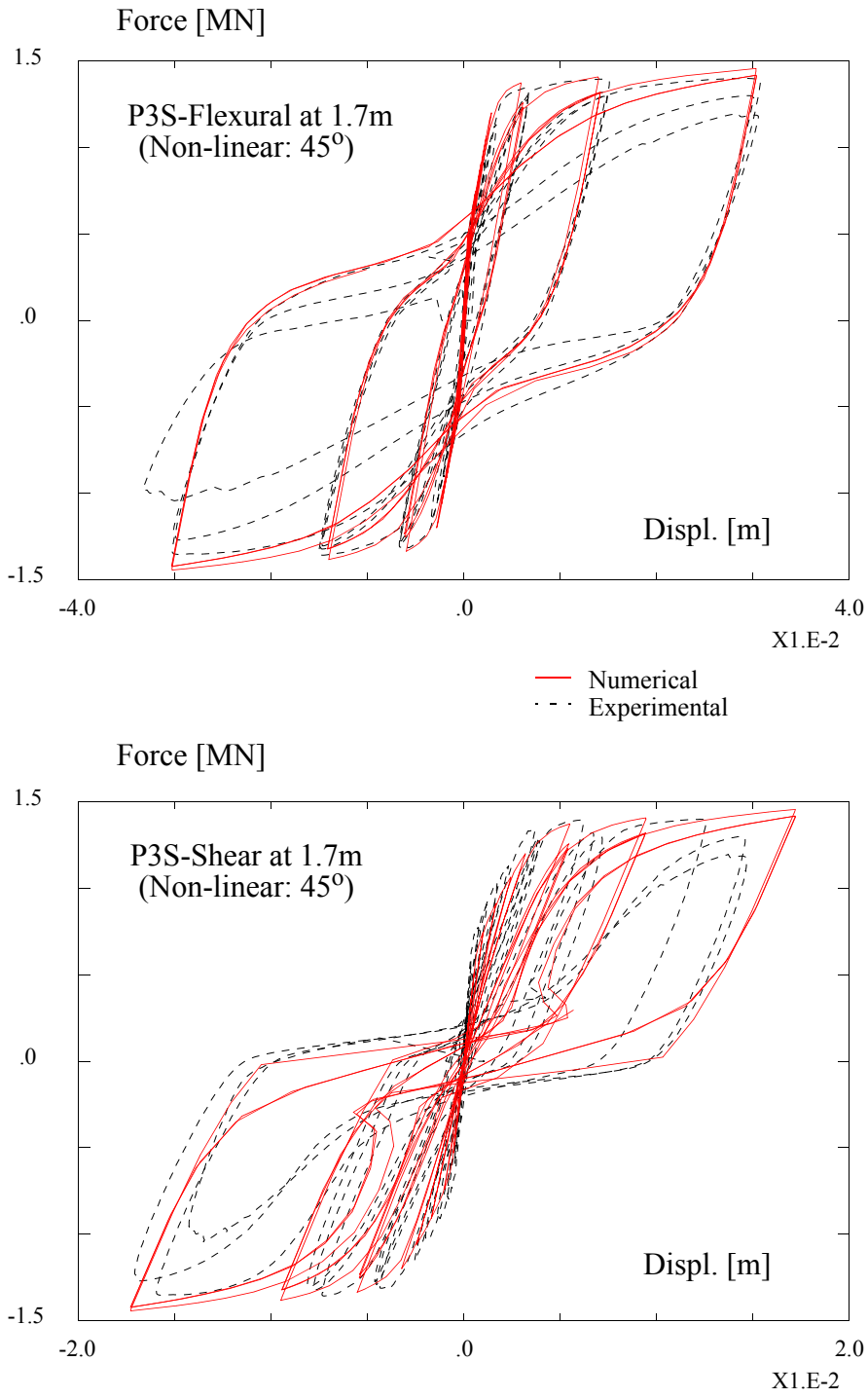

Figure 9.27 - Numerical versus experimental force-flexural and shear displacement response curves at 1.7m from the bottom, for pier P3S, using the non-linear shear model with θ=45°

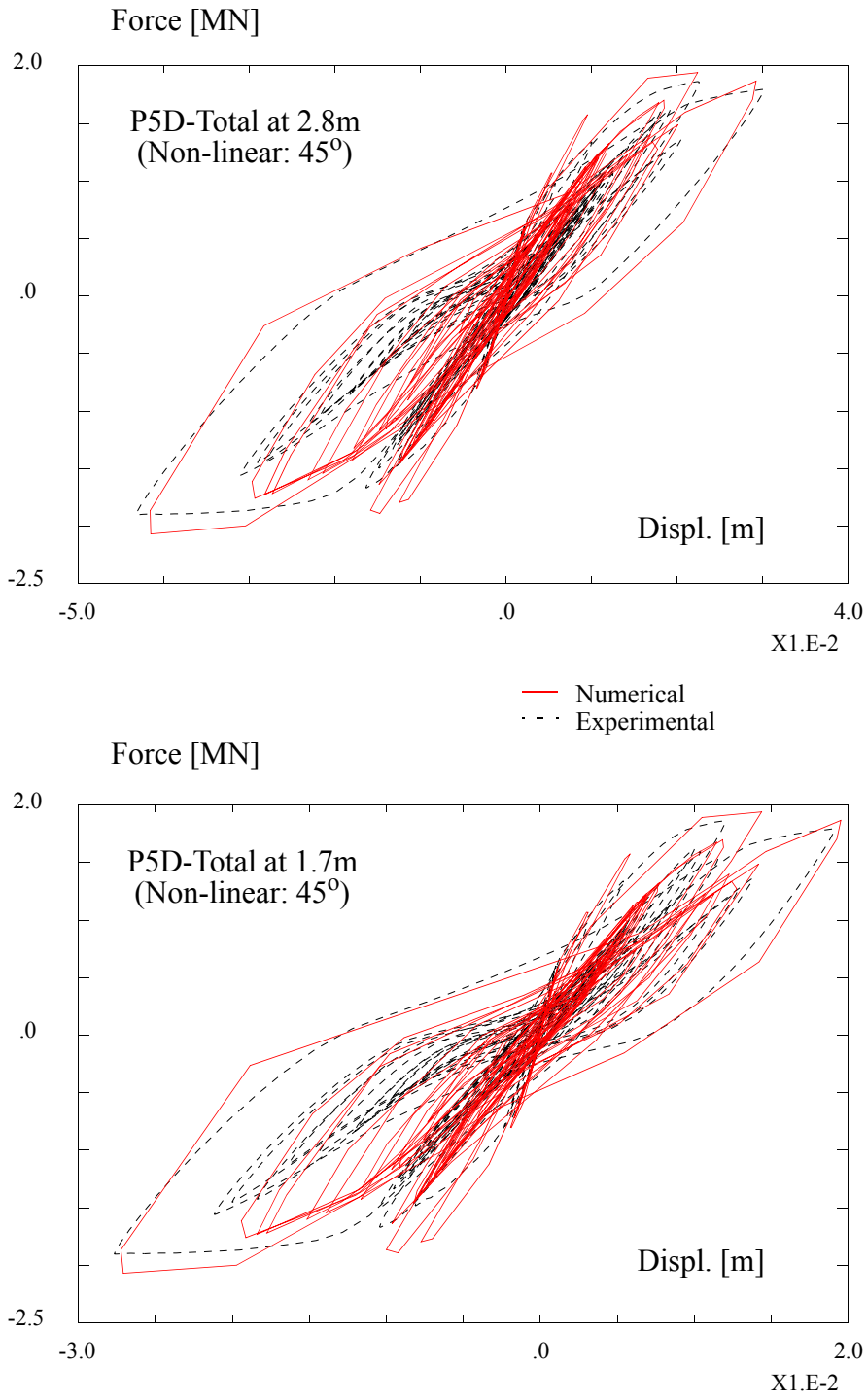

Figure 9.28 - Numerical versus experimental force-total displacement response curves for pier P5D at two different height levels and using the non-linear shear model with θ=45°

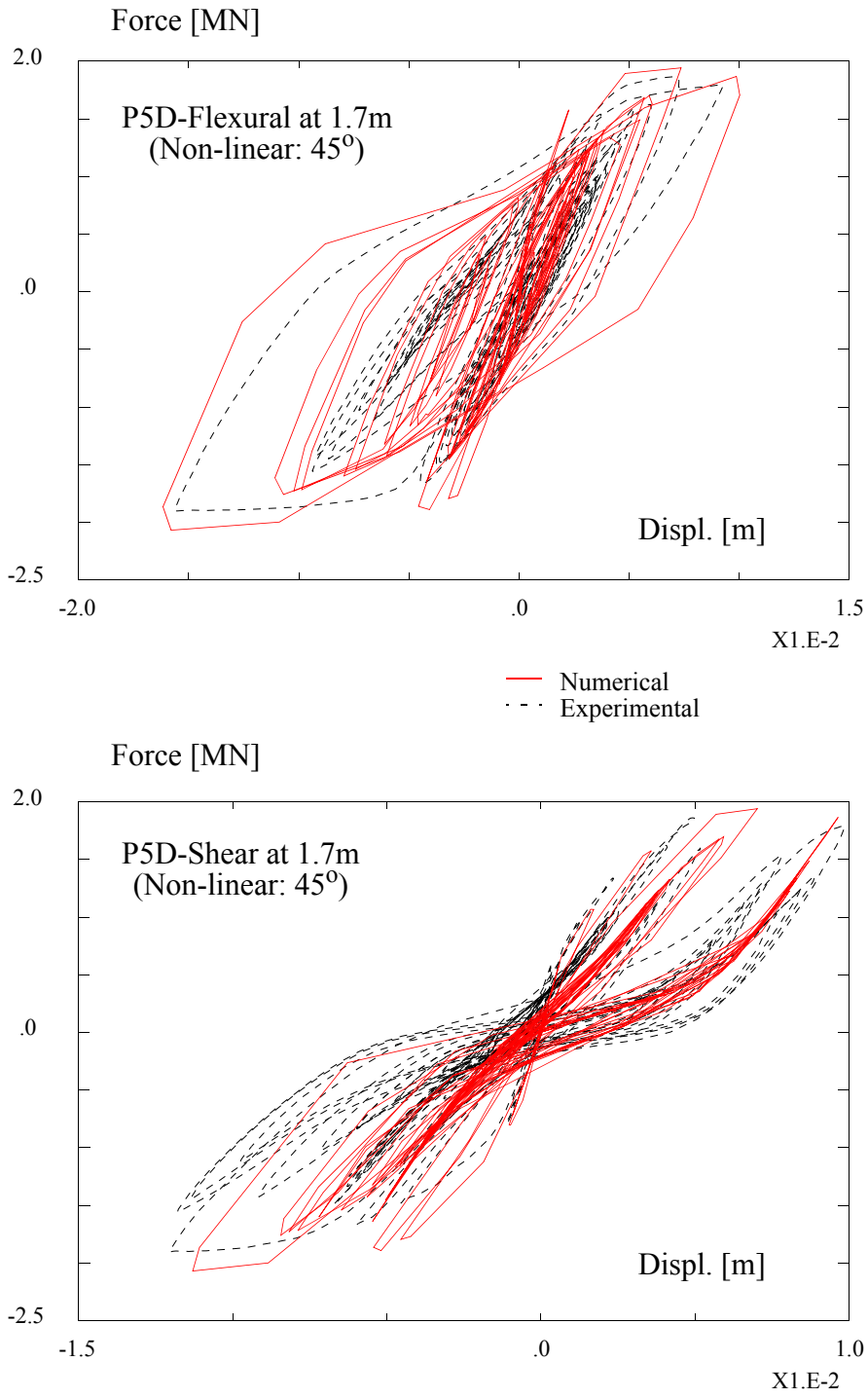

Figure 9.29 - Numerical versus experimental force-flexural and shear displacement response curves at 1.7m from the bottom, for pier P5D, using the non-linear shear model with θ=45°

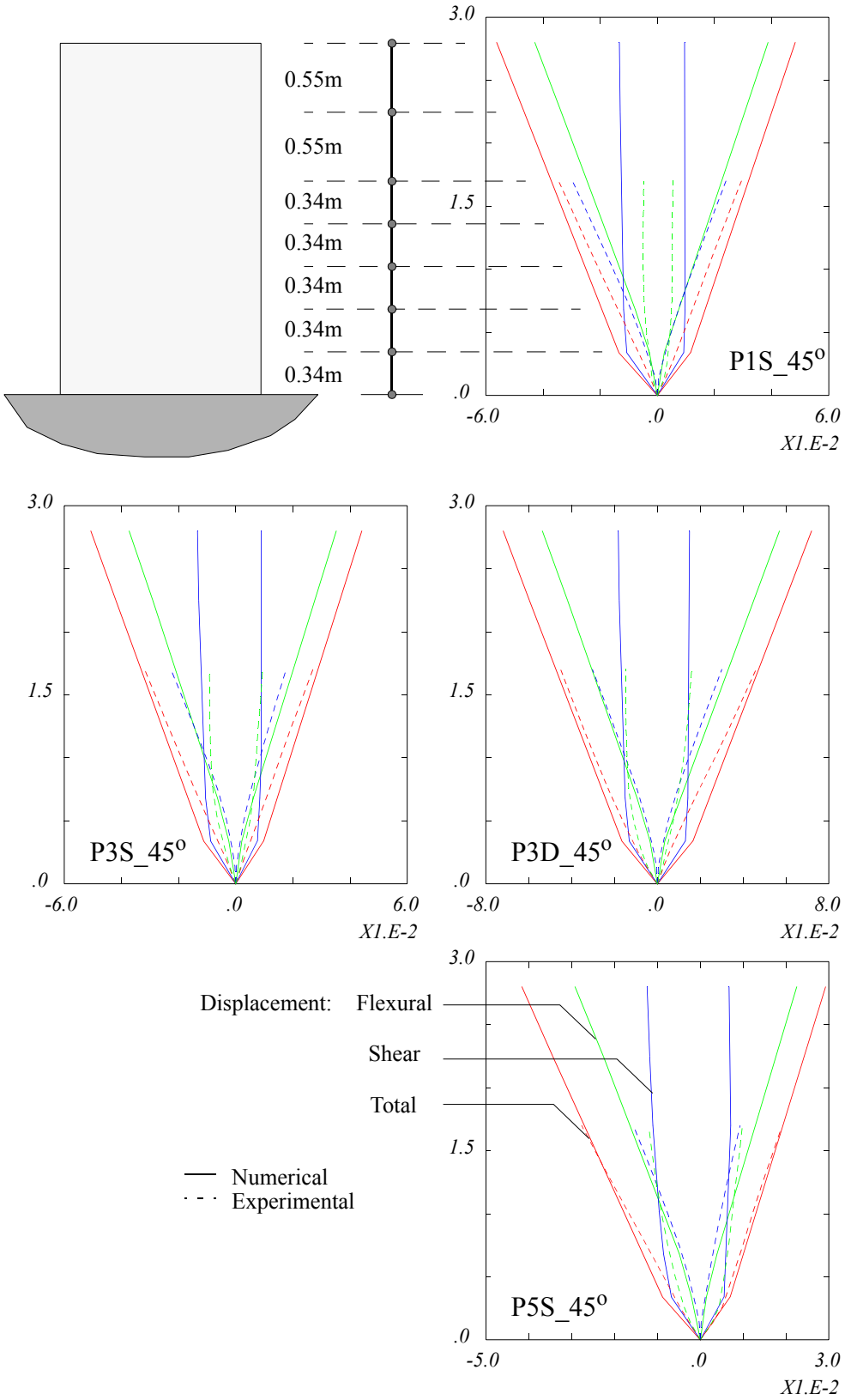

Figure 9.30 - Numerical versus experimental peak displacement profiles for the four piers and the non-linear shear model

European Commission

EUR 24153 EN – Joint Research Centre – Institute for the Protection and Security of the Citizen
Title: Non-linear Shear Model for R/C Piers
Author(s): J. Guedes, A.V. Pinto, P. Pegon
Luxembourg: Office for Official Publications of the European Communities
2010 – 114 pp. – 21 x 29.7 cm
EUR – Scientific and Technical Research series – ISSN 1018-5593
ISBN 978-92-79-14874-3
DOI 10.2788/56304

Abstract
The work presented has been developed within the Prenormative Research in support of EuroCode 8 (PREC8) programme of the European Commission. The EuroCode 8 (EC8) are the provisional European standards for the design of civil engineering structures in seismic prone areas. This programme included experimental test on a series of bridge structures that have been tested under Pseudo-Dynamic conditions.
Experimental tests were carried out to study the behaviour of bridge piers under cyclic loading. The results from these tests underlined the need to improve an existing fiber model to represent the non-linear behaviour of structures where the influence of the shear forces is not negligible. Thus, a strut-and-tie formulation coupled with the classic fibre model for flexural forces was developed. This formulation is based on the analogy of a R/C structure damaged with diagonal cracking with a truss made of concrete diagonals and steel ties.
The model is applied to a set of bridge piers tested at the ELSA laboratory and the results are compared with the experimental response.

How to obtain EU publications

Our priced publications are available from EU Bookshop (http://bookshop.europa.eu), where you can place an order with the sales agent of your choice.

The Publications Office has a worldwide network of sales agents. You can obtain their contact details by sending a fax to (352) 29 29-42758.

The mission of the JRC is to provide customer-driven scientific and technical support for the conception, development, implementation and monitoring of EU policies. As a service of the European Commission, the JRC functions as a reference centre of science and technology for the Union. Close to the policy-making process, it serves the common interest of the Member States, while being independent of special interests, whether private or national.

JRC
EUROPEAN COMMISSION

LB-NA-24153-EN-N

ISBN 978-92-79-14874-3